Proceedings
of the
Fourth International Symposium
on the
Interaction of Non-nuclear Munitions
with Structures
(volume 2)

Panama City Beach, Florida
April 17-21, 1989

REPORT DOCUMENTATION PAGE

Form Approved
OMB No. 0704-0188

1. AGENCY USE ONLY (*Leave blank*)	2. REPORT DATE	3. REPORT TYPE AND DATES COVERED
	April 1989	Final Report for April 17-21, 1989

4. TITLE AND SUBTITLE
Proceedings of the Fourth International Symposium on the Interaction of Non-nuclear Munitions with Structures (volume 2)

5. FUNDING NUMBERS
F08635-88-C-0067

6. AUTHOR(S)
Captain Diane B. Miller (Symposium Project Officer)

7. PERFORMING ORGANIZATION NAME(S) AND ADDRESS(ES)
Air Force Engineering and Services Center
Air Force Engineering and Services Laboratory
Tyndall AFB FL 32403-6001

8. PERFORMING ORGANIZATION REPORT NUMBER
ESL-TR-89-21 Vol 2

9. SPONSORING/MONITORING AGENCY NAME(S) AND ADDRESS(ES)
(Same as 7)

10. SPONSORING/MONITORING AGENCY REPORT NUMBER

11. SUPPLEMENTARY NOTES

12a. DISTRIBUTION/AVAILABILITY STATEMENT
Distribution unlimited.
Approved Public Release.

12b. DISTRIBUTION CODE

13. ABSTRACT (*Maximum 200 words*)

For the first 60 years of the 20th Century, criteria and methods based on the results of catastrophic events were used for the design of explosive facilities. The criteria and methods did not include a detailed or reliable quantitative basis for assessing the degree of protection afforded by the protective facility. In the late 1960's quantitative procedures were set forth in the first edition of the present manual, "Structures to Resist the Effects of Accidental Explosions." The manual was based on extensive research and development programs which permitted a more reliable approach to current and future design requirements. Since the original publication of this manual, more extensive testing and development programs have taken place. This additional research was directed primarily towards materials other than reinforced concrete which was the principal construction material referenced in the initial version of the manual. An upgrade to the manual, describing new design techniques has become essential. Design methods in the proposed upgrade provide required structural protection.

14. SUBJECT TERMS

15. NUMBER OF PAGES

16. PRICE CODE

17. SECURITY CLASSIFICATION OF REPORT	18. SECURITY CLASSIFICATION OF THIS PAGE	19. SECURITY CLASSIFICATION OF ABSTRACT	20. LIMITATION OF ABSTRACT
UNCLASSIFIED	UNCLASSIFIED	UNCLASSIFIED	SAR

GENERAL INSTRUCTIONS FOR COMPLETING SF 298

The Report Documentation Page (RDP) is used in announcing and cataloging reports. It is important that this information be consistent with the rest of the report, particularly the cover and title page. Instructions for filling in each block of the form follow. It is important to *stay within the lines* to meet *optical scanning requirements*.

Block 1. Agency Use Only *(Leave blank)*.

Block 2. Report Date. Full publication date including day, month, and year, if available (e.g. 1 Jan 88). Must cite at least the year.

Block 3. Type of Report and Dates Covered. State whether report is interim, final, etc. If applicable, enter inclusive report dates (e.g. 10 Jun 87 - 30 Jun 88).

Block 4. Title and Subtitle. A title is taken from the part of the report that provides the most meaningful and complete information. When a report is prepared in more than one volume, repeat the primary title, add volume number, and include subtitle for the specific volume. On classified documents enter the title classification in parentheses.

Block 5. Funding Numbers. To include contract and grant numbers; may include program element number(s), project number(s), task number(s), and work unit number(s). Use the following labels:

C -	Contract	PR -	Project
G -	Grant	TA -	Task
PE -	Program Element	WU -	Work Unit Accession No.

Block 6. Author(s). Name(s) of person(s) responsible for writing the report, performing the research, or credited with the content of the report. If editor or compiler, this should follow the name(s).

Block 7. Performing Organization Name(s) and Address(es). Self-explanatory.

Block 8. Performing Organization Report Number. Enter the unique alphanumeric report number(s) assigned by the organization performing the report.

Block 9. Sponsoring/Monitoring Agency Name(s) and Address(es). Self-explanatory.

Block 10. Sponsoring/Monitoring Agency Report Number. *(If known)*

Block 11. Supplementary Notes. Enter information not included elsewhere such as: Prepared in cooperation with...; Trans. of...; To be published in.... When a report is revised, include a statement whether the new report supersedes or supplements the older report.

Block 12a. Distribution/Availability Statement. Denotes public availability or limitations. Cite any availability to the public. Enter additional limitations or special markings in all capitals (e.g. NOFORN, REL, ITAR).

- **DOD** - See DoDD 5230.24, "Distribution Statements on Technical Documents."
- **DOE** - See authorities.
- **NASA** - See Handbook NHB 2200.2.
- **NTIS** - Leave blank.

Block 12b. Distribution Code.

- **DOD** - Leave blank.
- **DOE** - Enter DOE distribution categories from the Standard Distribution for Unclassified Scientific and Technical Reports.
- **NASA** - Leave blank.
- **NTIS** - Leave blank.

Block 13. Abstract. Include a brief *(Maximum 200 words)* factual summary of the most significant information contained in the report.

Block 14. Subject Terms. Keywords or phrases identifying major subjects in the report.

Block 15. Number of Pages. Enter the total number of pages.

Block 16. Price Code. Enter appropriate price code *(NTIS only)*.

Blocks 17. - 19. Security Classifications. Self-explanatory. Enter U.S. Security Classification in accordance with U.S. Security Regulations (i.e., UNCLASSIFIED). If form contains classified information, stamp classification on the top and bottom of the page.

Block 20. Limitation of Abstract. This block must be completed to assign a limitation to the abstract. Enter either UL (unlimited) or SAR (same as report). An entry in this block is necessary if the abstract is to be limited. If blank, the abstract is assumed to be unlimited.

*U.S.GPO:1990-0-273-271

Proceedings
of the
Fourth International Symposium
on the
Interaction of Non-nuclear Munitions
with Structures
(volume 2)

Panama City Beach, Florida
April 17-21, 1989

This document is Volume 2 of the Proceedings of the Fourth International Symposium on the Interaction of Non-Nuclear Munitions with Structures, held at the Edgewater Beach Resort, Panama City Beach, Florida from 17 through 21 April 1989. The symposium was sponsored by the Air Force Engineering and Services Center, Engineering and Services Laboratory, Tyndall AFB, Florida, and endorsed by the American Society of Civil Engineers' Structural Division.

The symposium was coordinated by Applied Research Associates, Inc. (ARA), Tyndall AFB, Florida, under USAF Contract F08635-88-C-0067, Subtask 2.03, and administered by the University of Florida Graduate Engineering Center, Eglin AFB, Florida, under subcontract to ARA. Mrs. Lily C. Clouston was the University of Florida's Symposium Administrator; Dr. Douglas H. Merkle was ARA's Symposium Coordinator and Proceedings Editor; and Captain Diane B. Miller was the Engineering and Services Laboratory's Symposium Project Officer.

All manuscripts in this document authored by United States authors have been approved for public release.

TABLE OF CONTENTS

AUTHOR INDEX

ABSTRACT

By

Chester E. Canada and Jerry Ward
DOD Explosive Safety Board

UPGRADE

of

"Structures to Resist the Effects of Accidental Explosions" (Army TM 5-1300/NAVFAC P-397/AFM 88-22)

For the first 60 years of the 20th Century, criteria and methods based on the results of catastrophic events were used for the design of explosive facilities. The criteria and methods did not include a detailed or reliable quantitative basis for assessing the degree of protection afforded by the protective facility. In the late 1960's quantitative procedures were set forth in the first edition of the present manual, "Structures to Resist the Effects of Accidental Explosions". The manual was based on extensive research and development programs which permitted a more reliable approach to current and future design requirements. Since the original publication of this manual, more extensive testing and development programs have taken place. This additional research was directed primarily towards materials other than reinforced concrete which was the principal construction material referenced in the initial version of the manual. An upgrade to the manual, describing new design techniques had become essential. Design methods in the proposed upgrade provide required structural protection.

This paper reviews differences and additions between the earlier version and the proposed upgrade. The planned schedule for technical review, Tri-Service coordination, and publication is presented.

"Structures to Resist the Effects of Accidental Explosions"

- PRESENTS METHODS TO ESTIMATE BLAST LOADS DUE TO ACCIDENTAL EXPLOSIONS

- PRESENTS DESIGN AND CONSTRUCTION METHODS FOR PROTECTIVE STRUCTURES HOUSING DOD EXPLOSIVE MATERIALS OPERATIONS

- DESIGN PRINCIPLES REQUIRED BY DOD 6055.9 STD

"Structures to Resist the Effects of Accidental Explosions"

(SHORT HISTORY)

- FIRST PUBLISHED IN 1969
- MODIFIED IN 1971
- NEED TO UPGRADE EVIDENT FROM EARLY 70'S
- PROPOSAL FOR UPGRADE IN 1978
- FUNDING ALLOCATED FOR UPGRADE IN 1980
- REVISION PROCESS (1980—PRESENT)
- OBTAIN TRI—SERVICE APPROVAL IN 1989
- PUBLISH APPROVED MANUAL IN 1990

"Structures to Resist the Effects of Accidental Explosions"
(AD NUMBERS OF CANDIDATE UPGRADE)

VOL #	AD #	NAME	DATE
1	A187052	INTRODUCTION	DEC 87
2	A176675	BLAST, FRAGMENT, AND SHOCK LOADS	DEC 86
3	A148895	PRINCIPLES OF DYNAMIC ANALYSIS	JUN 84
4	A178901	REINFORCED CONCRETE DESIGN	APR 87
5	A180470	STRUCTURAL STEEL DESIGN	MAY 87
6	A154275	SPECIAL CONSIDERATIONS IN EXPLOSIVE FACILITY DESIGN	APR 85

Structures to Resist the Effects of Accidental Explosions

OLD vs NEW

- SIX VOLUMES & ABOUT 1800 PAGES vs ONE VOLUME & ABOUT 250 PAGES
- NEW TOPICS: DESIGN WITH CMU AND STEEL MATERIALS
  BLAST RESISTANT WINDOWS
  SUPPRESSIVE SHIELDS
  PRE-ENGINEERED STRUCTURES
- ELECTRONIC (PC-BASED) VERSION TO BE AVAILABLE

NEW REVISION	OLD EDITION
VOL 1	CHAPTERS 1, 2, 3
VOL 2	CHAPTER 4
VOL 3	CHAPTER 6
VOL 4	CHAPTERS 5, 7, 8, 9
VOL 5	NEW MATERIAL
VOL 6	CHAPTER 10 & NEW MATERIAL

"Structures to Resist the Effects of Accidental Explosions"

- THREE TOPICS REQUIRE TECHNICAL REVIEW
  - INTERPRETATION OF SAFETY CRITERIA
  - LACING CRITERIA
  - BLAST RESISTANT WINDOW CRITERIA

- PLANS ARE TO
  - CONDUCT LIMITED PEER REVIEW OF THREE TOPICS
  - CONDUCT CURSORY EDITORIAL REVIEW OF MANUAL
  - RECOMMEND TRI-SERVICE APPROVAL IN 1989
  - PUBLICATION FORMAT TO ALLOW CHANGES

Enhancements of the Prediction of Ground Shock From Penetrating Weapons

James L. Drake, Elizabeth B. Smith and Scott E. Blouin

Applied Research Associates, Inc.
South Royalton, Vermont

ABSTRACT

This paper presents a procedure that predicts peak particle accelerations, velocities, displacements and stresses on axis beneath bombs exploding on or within the ground. It uses and reconciles the high explosive ground shock data base, results of numerical calculations, and theoretical considerations, including conservation laws, cavity expansion theory and similitude. The method reproduces most observed contained burst explosion data in media ranging from loose soil to hard rock.

BACKGROUND

This paper is an update to a paper entitled "Ground Shock from Penetrating Conventional Weapons" authored by James L. Drake and Charles D. Little, Jr. The original paper presented an empirical method to predict the ground shock environment in soil from conventional weapons as a function of burst position, soil indices and burster layer thickness. The analysis presented here describes certain enhancements to that prediction method especially the prediction of the near source ground shock environment.

SOIL PROPERTY EFFECTS

While no single material property index or combination of indices can be used to fully prescribe ground shock propagation, the seismic velocity c_i, the primary loading wavespeed c_o and the compactible air void volume ϵ_o are valuable indices for assessing ground shock magnitudes. The seismic velocity is associated with propagation of low amplitude waves through the in situ material and is not always indicative of the behavior of in situ materials at higher stress levels. The primary loading wave velocity is controlled by the in situ material response at stress levels of engineering interest and, as explained below, is generally slower than the seismic velocity and a better indicator of the dynamic in situ response. Unfortunately, the primary loading wave velocity is considerably more difficult to determine than is the seismic velocity. Ground shock attenuation rates with depth are controlled by the compaction of material during the passage of the stress wave. Dry weak rocks such as sandstones and tuff have crushable air voids and attenuate the shock more rapidly than hard rocks that contain few or no voids. Alluvial materials and soil have high crushable air voids and attenuate the shock more rapidly than all but the weakest, most dry porous rocks.

The seismic velocity and primary loading wave velocity provide a fundamental relation between space and time for scaling ground motions. Since the characteristic time for a given event is inversely proportional to the propagation velocity, explosions in strong competent materials (high seismic and loading wave velocities) will produce much shorter duration ground motion pulses than like bursts in soft rock and soils. The primary loading wave velocity provides a measure of the modulus of the medium. Thus, explosions in strong competent materials with high propagation velocities will produce higher accelerations and lower displacements than corresponding explosions in soft media having lower propagation velocities.

GROUND SHOCK ENVIRONMENT

Approximate analytical solutions for an expanding spherical shock wave in a nearly incompressible media, were used as the basis of the near source region analysis. Considering conservation of mass between the expanding cavity and the observation point, it was found that the flow field can be estimated by

$$v(t) = \dot{r}_c \left(\frac{r_c}{r}\right)^n \tag{1}$$

where v is the particle velocity, $r_c(t)$ is the expanding cavity radius and n is a constant of approximately 2. The magnitude of the particle velocity and the attenuation in the high pressure large flow region near the source are controlled by the cavity expansion rate and the geometric spreading of the shock front.

The kinetic energy in the source region can be estimated by

$$KE = 4\pi\rho_o \int_{r_c}^{r} r^2 \frac{v^2}{2}\, dr = 2\pi\rho_o \dot{r}_c^{\,2} r_c^{\,3} \left(1 - \frac{r_c}{r}\right) \tag{2}$$

assuming $n = 2$ and ρ_o is the initial density. Assuming that within the source region the kinetic energy in the flow field is approximately equal to 1/2 of the total weapon yield and also noting that for TNT 1kg = 4.6186E6 joules, then

$$v_p = 606.2 \left(\frac{W}{\rho_o r^3}\right)^{1/2} \tag{3}$$

where v_p is the peak particle velocity and W is the contained yield of the weapon in kg.

For incompressible flow $n = 2$. However, it has been shown that n can be generalized to account for volume changes in compactible materials by the expression

$$n = \frac{2 + \epsilon}{1 - \epsilon} \tag{4}$$

where ϵ is a constant <<1, that relates the volume change to the shear strain in the flow field. Attenuation rates observed in the data base show that $\epsilon = \epsilon_o$ where ϵ_o is the compactible air voids. For saturated material. n is less than 2 and depends on the strength of the material.

Empirical fits were made to peak ground motion and stress data obtained from contained HE detonations in soil and to results of finite difference calculations in various soil and rock geologies. The resulting expressions represent the best estimate of the contained explosion data base and are consistent with scaling relationships and near field analysis.

$$a_p = \frac{2\, v_p}{g\, t_r} \qquad r > .155\, W^{1/3} \tag{5}$$

$$v_p = \begin{cases} \dfrac{606.2}{\sqrt{\rho_o}} \left(\dfrac{r}{W^{1/3}} \right)^{-3/2} & r < .155\, W^{1/3} \quad (6) \\[2ex] \dfrac{9906}{\sqrt{\rho_o}} \left(\dfrac{r}{r_c} \right)^{-n} & r > .155\, W^{1/3} \quad (7) \end{cases}$$

$$\frac{d_p}{W^{1/3}} = \frac{3.31}{c_i} \left(\frac{r}{W^{1/3}}\right)^{-2} \qquad r > .155\, W^{1/3} \tag{8}$$

$$\sigma_p = \rho_o\, c_L\, v_p \tag{9}$$

where

$$r_c = .155\, W^{1/3} \tag{10}$$

$$c_L = c_o + S\, v_p \tag{11}$$

$$t_r = \left(\frac{c_i}{c_L} - 1 \right) \frac{r}{c_i} \qquad c_i > c_L \tag{12}$$

Terms in the above equations are defined as

a_p = peak radial acceleration (g)
d_p = peak displacement (m)
σ_p = peak stress (P_a) (1 Kbar = 10^8 P_a)
r = radial distance from the explosion (m)
g = gravitational acceleration (m/s^2)
n = peak velocity attenuation exponent
S = equation of state factor (≈1.5 for geologic media)
t_r = rise time (s)

The peak velocity and stress attenuations from the above equations and the soil parameters from Table 1 are compared to the data in Figure 1 for both dry and saturated media. The previous fits to the data are also included in the plots. The new methodology extends the prediction into much higher stress regimes.

The peak particle velocity in the source region are included in the above equations. The magnitude and attenuation rate are controlled by the cavity expansion rate and the geometric spreading of the shock front. This region extends to a range of .155 $m/kg^{1/3}$ which corresponds to the approximate size of the expanded cavity in most rocks. Within this region, the material displacements are large with respect to the initial position, so that material is pushed into a relatively thin shell with an approximately constant kinetic energy density. The resulting peak particle velocity is only weakly dependent on the material properties.

The loading wave velocity is a function of the loading intensity. It generally starts from the primary loading wavespeed and monotonically increases with increasing stress. For most geologic materials, the propagation speed can be approximated by relating it to the initial loading wavespeed and the peak particle velocity through the use of the factor S which is a function of the overall compressibility of the material.

The material model for all rocks and soils has been simplified to relate the loading wavespeed to the peak particle velocity with the parameter $S \approx 1.5$. This has been done to allow the user to employ this methodology with relatively little knowledge of the actual material model of the geology of interest. If the actual uniaxial stress strain response is known, it can easily be substituted to relate the loading wavespeed to the peak particle velocity.

The magnitude of the stress and ground motion will be greatly enhanced as the weapon penetrates more deeply into the soil. The concept of a coupling factor was introduced in the previous paper and is summarized here. This factor accounts for the effect of weapon penetration on the ground shock parameters and is defined as the ratio of the ground shock magnitude from a partially buried weapon to the ground shock from a fully contained burst in the same media. The coupling factor, f, can be determined from Figure 2 and the acceleration, velocity, stress and

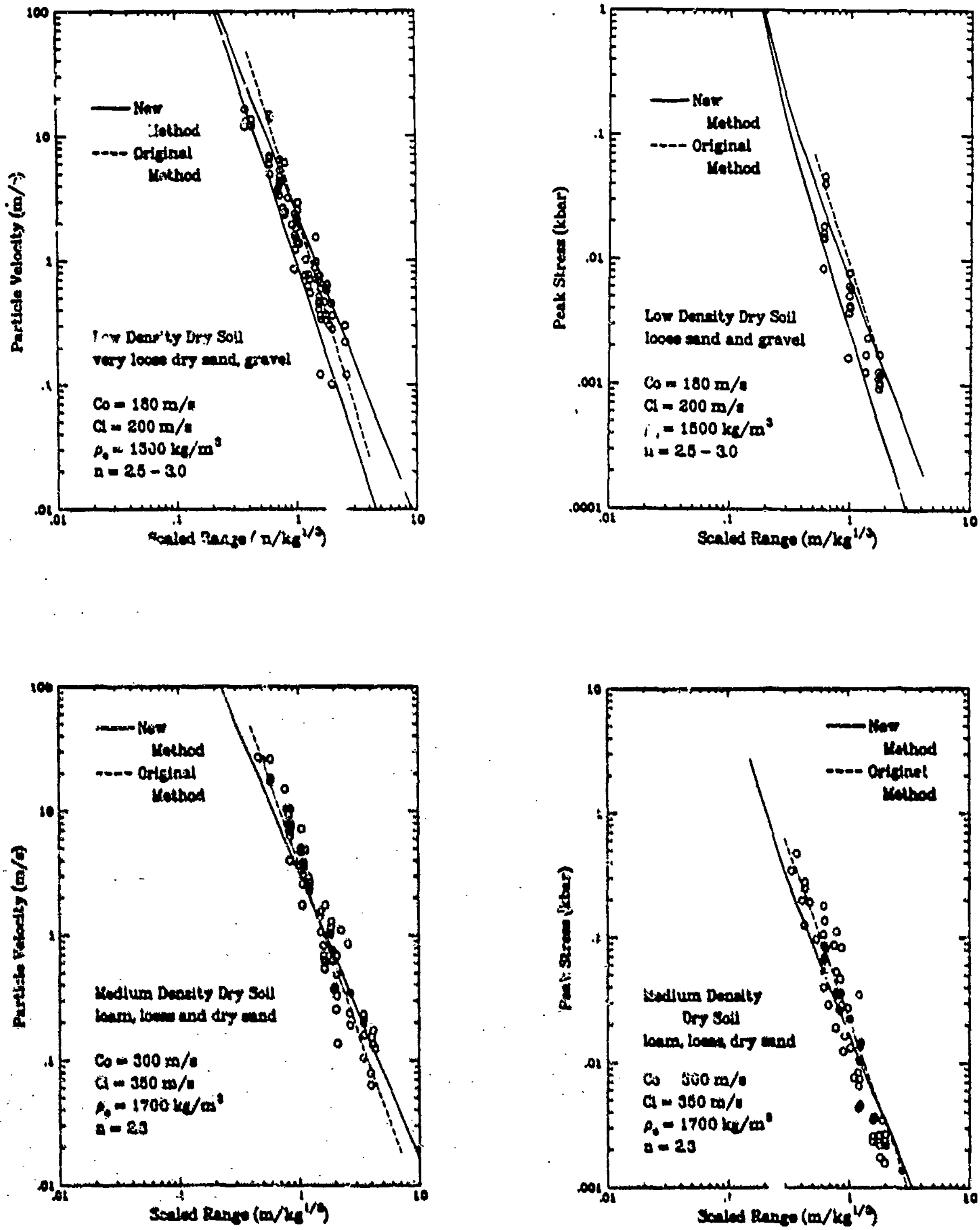

Figure 1a. Comparison of peak velocity and stress attenuation prediction to explosive data.

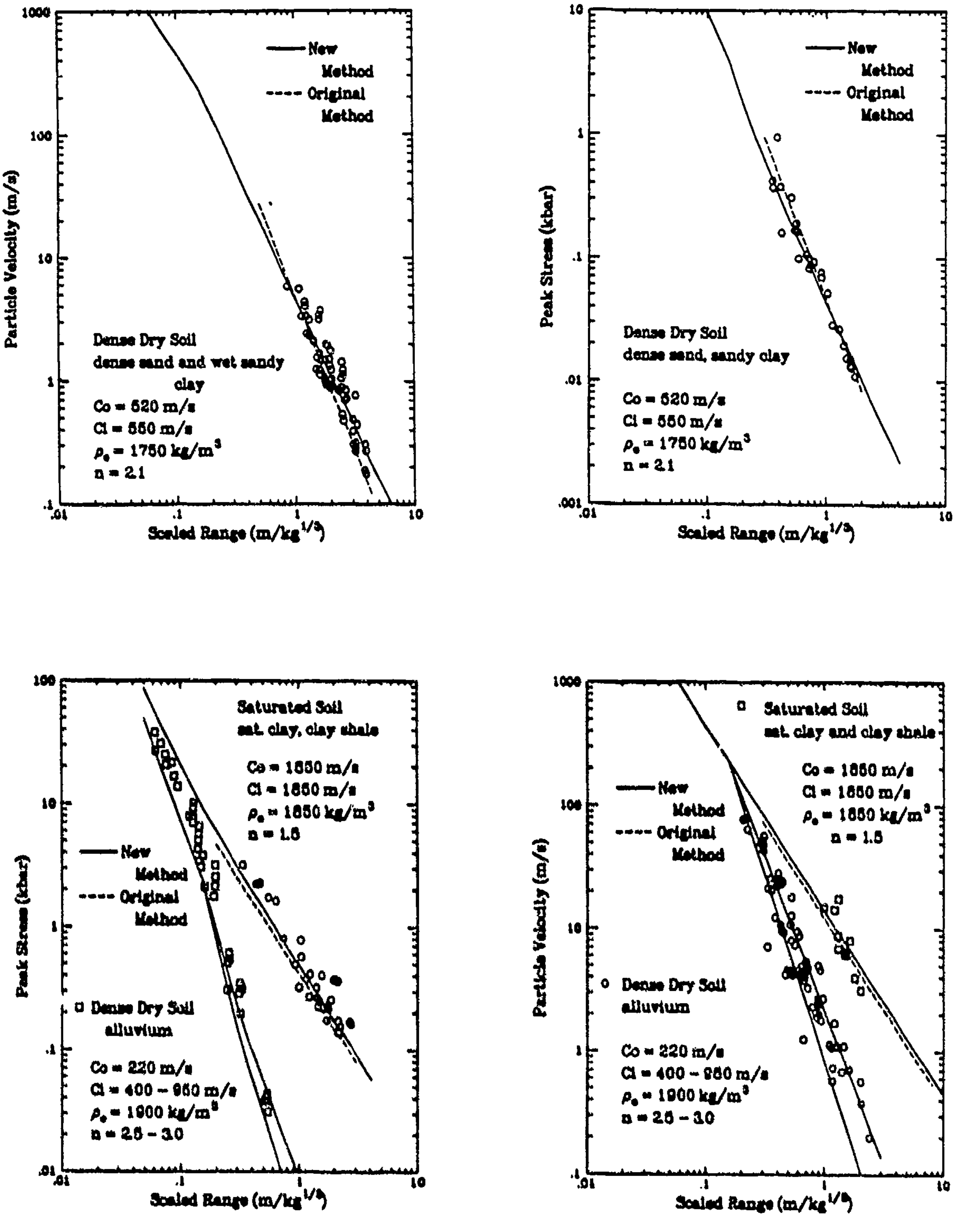

Figure 1b. Comparison of peak velocity and stress attenuation prediction to explosive data.

displacemont obtained from the above equations should be multiplied by this factor for shallow buried bursts.

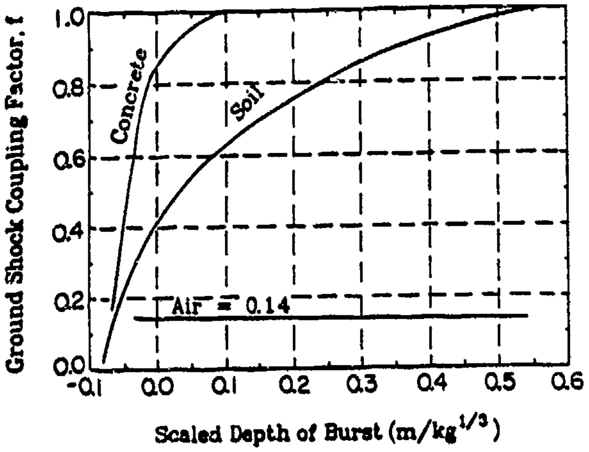

Figure 2. Ground shock coupling factor as a function of scaled depth of burst.

Stress and motion time histories can be characterized by exponential time histories that decay rapidly in amplitude and broaden as they propagate outward from the explosion (Figure 3). The characteristic time for these time histories can be measured in arrival time from the source, $t_a = r/c_i$, the time of peak, $t_p = r/c_L$, and the time of positive phase duration t_+ where

$$t_+ = 2.72 \frac{d_p}{v_p} - 0.36\ t_r \qquad (13)$$

Assuming a linear rise to peak velocity, the velocity waveform can be approximated by

$$v(t) = v_p\left(\frac{t - t_a}{t_r}\right) \qquad t_a \leq t \leq t_p \qquad (14)$$

$$v(t) = v_p\left(\frac{t_d - t}{t_d - t_p}\right)e^{-\left(\frac{t - t_p}{t_d - t_p}\right)} \qquad t \leq t_p \qquad (15)$$

where t_d is the absolute time at the end of the positive phase duration. Since the time domain waveform features are inversely proportional to the propagation velocity, explosions in competent material (high c_i) will produce shorter pulses with higher accelerations and lower displacements than corresponding explosions in less competent material (low c_i). Consistent scaling relationships also require higher accelerations to be associated with higher stresses and lower displacements. Conversely, low accelerations will be associated with lower stresses and higher displacements.

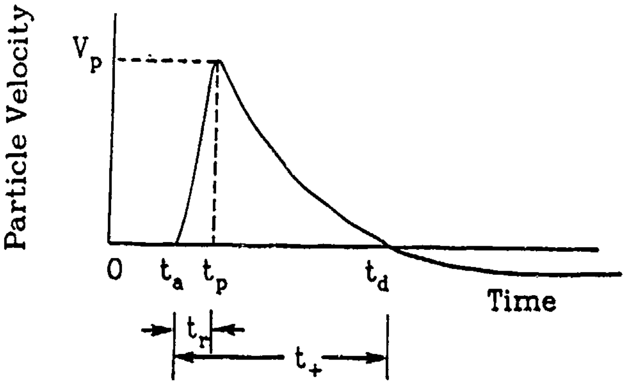

Figure 3. Particle velocity time history.

CONCLUSIONS

Empirical expressions were derived from a fit to a large body of ground shock data from buried bursts in soil. These expressions were derived using a more sophisticated material model than originally used by Drake and Little. The resulting equations more accurately predict the near source environments. These modifications of Drake and Little's work do not negate the previous study. The extend it over a broader range of peak stresses and over a broader range of geologies.

The method presented here is not necessarily recommended over the previous method but is more valid at regions closer to the source and is based on a more rigorous theoretical approach which closely approximates actual test data in virtually all types of geologic materials. The two methods are in close agreement at farther ranges.

SOIL CATEGORY	TYPES AND EXAMPLES	TYPICAL IN SITU DENSITY ρ_o (kg/m^3)	TYPICAL SEISMIC WAVESPEED c_i (m/s)	TYPICAL INITIAL LOADING c_o (m/s)	VELOCITY ATTENUATION EXPONENT n
Dense Dry Soil	alluvium	1900	500 1000 (cemented)	220	2.5 to 3.0
	dense sand	1750	550	520	2.1
Medium Density Dry Soil	sand, loam, alluvium	1700	350	300	2.3
Low Density Dry Soil	loose sand, loam	1500	200	180	2.5 to 3.0
Saturated Soil	all types	1850	1850	1850	1.5
High Strength Rock	quartzite, diabase, basalt, granite	2650	5500	4500	2.0
Medium Strength Rock	shales, porous sandstones and limestones, chlorite	2500	3400	2750	2.0
Low Strength Rock	porous tuff, clay, shales, schist	2000	2050	1550	2.3
Very Low Strength Rock	very porous and friable weathered rock	1400	1400	1050	2.5

Table 1. Generic soil and rock properties.

SINGLE DEGREE OF FREEDOM ANALYSIS OF BURIED ARCHES

R.A. Frank

Applied Research Associates, Inc.
Southeast Division
6404 Falls of Neuse Road, Suite 200
Raleigh, North Carolina 27615

ABSTRACT:

This paper presents the results of current research aimed at developing an improved single-degree-of-freedom (SDOF) analysis model for buried arches. Several refinements in the SDOF analysis procedures for buried arches are derived, including (1) development of a general soil-arch interaction model for defining the structure-media-interaction (SMI) loads on the arch, (2) development of equivalent SDOF response parameters for arches of arbitrary half-central angle, and (3) development of a resistance function that accounts for the moment-thrust load path the arch follows during deformation. The work assumes a cylindrical arch cross-section of arbitrary arch angle subjected to a vertically propagating planar ground shock. The elastic and plastic deformed shapes are derived for a characteristic load distribution and used to define the equivalent parameters for the SDOF model. This characteristic load is replaced in the response calculation by a simplified soil-arch interaction model which more accurately reflects the variation of the interface loads on the arch as it is engulfed. While the present model assumes a planar ground shock from a nuclear burst, the methodology is adaptable to conventional munitions.

INTRODUCTION:

The buried arch is a popular geometry for protective structure design: its curved geometry is capable of resisting high pressures through a combination of bending and thrust while providing a large interior span that can be used to store and protect military equipment such as aircraft. However, because of its geometry, analysis of the ground shock loads acting on the arch and its dynamic response is extremely complex and not well understood. As a result, current methods for analysis and design of buried arches are generally crude, over simplistic, and inadequate for predicting the dynamic loads and large deformation response of these structures.

One approach to modeling the complex response of buried arches is the finite element method wherein the complete arch geometry and structure-media-interaction can be modeled explicitly. The fast computational speeds and large memory capacity of modern computers allow one to model the arch in great detail without too great a penalty in turn-around time. However, finite element models are still time consuming to prepare and the results are often difficult to interpret. In addition, finite element models are cumbersome to use in preliminary design calculations, survivability/vulnerability assessments, and cost-trade studies. Hence, there is still a need for more simplified analysis procedures that can accurately predict the loads and response of buried structures. Furthermore, the high cpu speeds of modern computers alleviate the need to make many of the simplifying assumptions in SDOF models so that the accuracy of these models can be improved and potentially approach that of more sophisticated finite element models.

The research reported herein is addressing this need through the development of refined SDOF analysis procedures for buried arches. This work attempts to include as much of the appropriate physics as is possible while retaining the simplicity of the SDOF modeling approach. While the work is currently ongoing, the model derivation is complete and is presented in this paper. Comparisons with test data will be presented in a future paper.

SDOF MODEL FORMULATION:

A schematic of the loading and response of a buried arch as it is engulfed by a ground shock wave is shown in Figure 1. As the shock wave impinges on the arch, the ground shock stresses are reflected due to the impedance mismatch between the soil and the structure. Initially, only a small portion of the arch perimeter is loaded by the ground shock. As the ground shock propagates deeper, the perimeter of the arch that is loaded increases, until at engulfment the entire arch perimeter is loaded. Response of the arch is primarily in the first symmetric bending mode and analysis of recent test data and results of finite element calculations [1] show that the peak flexural response occurs during this engulfment phase. These studies have also shown that the response of the arch is not sensitive to the details of the loading and that the primary loading on the arch is due to the normal pressures on the arch. Interface shear stresses developed on the arch interface are generally small and can be neglected [1].

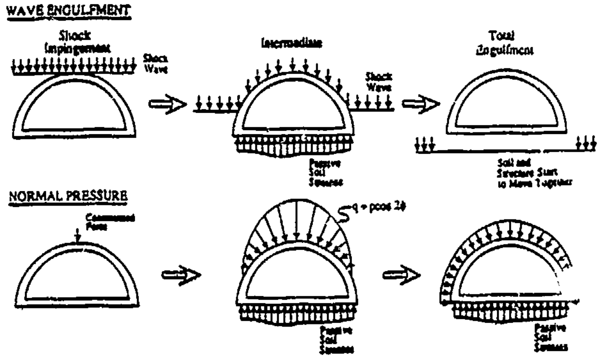

Figure 1: Planar Ground Shock on a Buried Arch

Crawford, et al. [2], have observed that the ground shock loads on buried cylinders and arches can be described using a characteristic $q + p\cos 2\phi$ stress distribution. This load distribution, shown in Figure 1, consists of a uniform component given by q and a nonuniform component given given by $p\cos 2\phi$. However, the magnitude and distribution of the interface stresses on the arch vary as the arch is engulfed so that the characteristic load distribution is not constant in time, rather, the relative magnitude of the two components varies. However, as will be demonstrated in the derivation of the deformed shapes, the q term does not influence the deformed shape or capacity (except through the moment-thrust interaction diagram) so that the temporal variation of the relative magnitude of the two components is not important to the derivation of the SDOF model parameters. It is important in determining the moment capacity and, consequently, the arch dynamic response.

Based on these observations, an equivalent SDOF model of the arch can be developed as illustrated in Figure 2. The interface loading on the arch is represented by a characteristic $q + p\cos 2\phi$ load distribution. The response is assumed to be in the first symmetric bending mode and the assumed mode shape is taken as the deformed shape of the arch under this load distribution applied statically. The equation of motion for the equivalent SDOF system is given by

$$M_e \ddot{w}_o + R_e = F_e(t) \tag{1}$$

where M_e, R_e, and F_e are the equivalent mass, resistance, and applied force for the SDOF system and $\ddot{w}_o$ is the vertical acceleration of the crown. The derivation of these parameters and the loading function are discussed in the following paragraphs.

Loading Function.

While the characteristic $q + p\cos 2\phi$ load distribution is used to derive the deformed shape and equivalent SDOF parameters, a more accurate description of the loading is desired in solving for the response of the arch. The approach followed uses a simplified SMI model based on linear wave theory to define the interface stresses on the arch. This approach has been used with good success in SDOF models for buried slabs subjected to ground shock from conventional and nuclear munitions [3]. The interface stresses on the arch are determined using a combination of simple wave propagation and rigid body mechanisms to pose the boundary conditions between the soil and the structure. The rate of external work done by the interface stresses is then calculated at each time increment and used to determine the response of the SDOF system and the equivalent q and $p\cos 2\phi$ interface stress components.

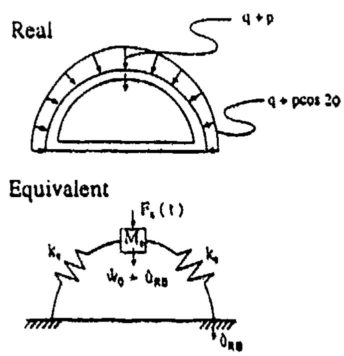

Figure 2. Arch SDOF Model.

Assuming a full-slip interface condition (zero interface strength), the interface load consists of normal stresses only which are given by (see Figure 3)

$$\sigma_n = \sigma_{ff_n} + \rho C_L \left(V_{ff_n} - \dot{u}_{RB} \cos \phi - \dot{w}\right) \tag{2}$$

where σ_{ff_n} = freefield ground shock stress normal to the arch interface, ρC_L = soil impedance, V_{ff_n} = freefield velocity normal to the arch interface, $\dot{u}_{RB}$ = vertical rigid body velocity of the arch, ϕ = angle to point of interest on the arch, and $\dot{w}$ = radial velocity of the arch at the point of interest. A planar, vertically propagating ground shock is assumed and the freefield ground shock velocity and stress are assumed constant behind the shock front. The component of the freefield velocity normal to the interface is given by

$$V_{ff_n} = V_{ff} \cos \phi \tag{3}$$

The freefield stresses normal to the arch interface are determined by transforming the freefield vertical and horizontal stresses to the plane normal to the arch interface. Representing the horizontal stress by $\sigma_{ff_h} = K_o\, \sigma_{ff_v}$ and assuming the vertical and horizontal freefield stresses represent principal stresses, the freefield stress normal to the arch interface is given by

$$\sigma_{ff_n} = q_{ff} + p_{ff} \cos 2\phi \tag{4}$$

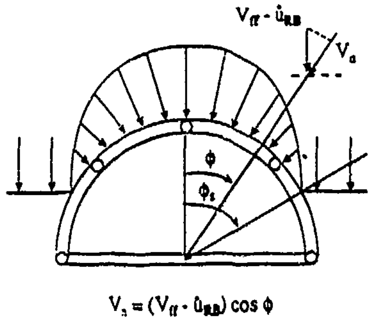

Figure 3. Planar Wave Loading Model

where

$$q_{ff} = \left(\frac{1+K_0}{2}\right)\sigma_{ff}, \quad \text{and} \quad p_{ff} = \left(\frac{1-K_0}{2}\right)\sigma_{ff}, \tag{5}$$

The rate of external work done by the interface stresses in deforming the arch is given by

$$\dot{W}_{ext} = \int_{\phi_R}^{\phi_S} \sigma_n \dot{w} r d\phi \tag{6}$$

$$= q_{ff}\int_{\phi_R}^{\phi_S} \dot{w} r d\phi + p_{ff}\int_{\phi_R}^{\phi_S} \dot{w}\cos 2\phi\, r d\phi$$

$$+ pC_L \left\{ (V_{ff} - \dot{u}_{RB}) \int_{\phi_R}^{\phi_S} \dot{w}\cos\phi\, r d\phi - \int_{\phi_R}^{\phi_S} \dot{w}^2 r d\phi \right\}$$

where the limits of integration are ϕ_R = arch angle to complete unloading ($\sigma_n \le 0$) and ϕ_S = arch angle to the current position of the shock front.

This external work rate is then used to define the equivalent load, F_e, where

$$F_e = \frac{\dot{W}_{ext}}{\dot{w}_0} \tag{7}$$

Likewise, the equivalent nonuniform loading component is given by

$$p_e = \frac{\dot{W}_{ext}}{\int \dot{w}\cos 2\phi\, r d\phi} \tag{8}$$

and the equivalent uniform component (evaluated at the crown) is given by

$$q_e = \sigma_n(0) - p_e \tag{9}$$

Deformed Shape
Elastic Response

The mode shape for the arch in the elastic response range is taken as the deformed shape for the arch under the characteristic $q + p\cos 2\phi$ load distribution. The solution for the deformed shape follows the general approach outlined by Timoshenko and Gere in Reference [4] and has been derived for fixed and pinned (2-hinged) support conditions. Referring to Figure 4, the elastic force resultants at any arbitrary angle from the crown are given by

$$V = \frac{pr}{9}\left(\{Av\}\sin\phi - 6\sin 2\phi\right) \tag{10}$$

$$N = \frac{pr}{9}\left(\{Av\}\cos\phi + 3\cos 2\phi\right) - qr \tag{11}$$

$$M = \frac{pr^2}{9}\left(\{A_M\} + 3\cos 2\phi - \{Av\}\cos\phi\right) \tag{12}$$

where the bracketed terms $\{A_M\}$ and $\{A_V\}$ depend on the support conditions and are of the general form

$$\{A\} = \left(\frac{A_0 + A_1\phi_0 + A_2\phi_0^2}{D_0 + D_1\phi_0 + D_2\phi_0^2}\right). \tag{13}$$

The constants for Equations 9 - 12 are:

$$Av_0 = \begin{cases} \text{fixed: } -3\ (\cos 3\phi_0 - \cos\phi_0) \\ \text{pinned: } -7\ \sin 3\phi_0 + 9\sin\phi_0 \end{cases}$$

$$Av_1 = \begin{cases} \text{fixed: } -2\ \sin 3\phi_0 - 6\sin\phi_0 \\ \text{pinned: } 6\ (\cos 3\phi_0 + \cos\phi_0) \end{cases}$$

$$Av_2 = \begin{cases} \text{fixed: } 0.0 \\ \text{pinned: } 0.0 \end{cases}$$

$$A_{M_0} = \begin{cases} \text{fixed: } 0.25\ (\cos 4\phi_0 + 8\cos 2\phi_0 - 9) \\ \text{pinned: } \sin 4\phi_0 + \sin 2\phi_0 \end{cases}$$

$$A_{M_1} = \begin{cases} \text{fixed: } 3\sin 2\phi_0 \\ \text{pinned: } -6\cos 2\phi_0 \end{cases}$$

$$A_{M_2} = \begin{cases} \text{fixed: } 0.0 \\ \text{pinned: } 0.0 \end{cases}$$

$$D_0\begin{cases}\text{fixed: } 2 - 2\cos 2\phi_0\\ \text{pinned: } -3\sin 2\phi_0\end{cases}$$

$$D_1\begin{cases}\text{fixed: } -\sin 2\phi_0\\ \text{pinned: } 2\left(2+\cos 2\phi_0\right)\end{cases}$$

$$D_2\begin{cases}\text{fixed: } -2.0\\ \text{pinned: } 0.0\end{cases}$$

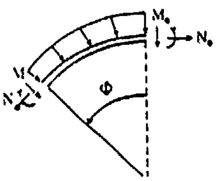

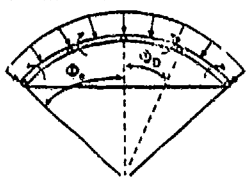

Figure 4. Arch Parameter Definitions and Static Collapse Mode

Finally, the radial displacements are given by

$$w = \frac{pr^4}{9EI}\left(\{A_w\}\cos\phi + \cos 2\phi - 0.5\{A_V\}\phi\sin\phi + \{A_M\}\right) \tag{14}$$

where

$$A_{w_0} = \begin{cases}\text{fixed: } 5(0.5\sin 4\phi_0 - \sin\phi_0)\\ \text{pinned: } -5\cos 4\phi_0 + 8\cos 2\phi_0 - 3\end{cases}$$

$$A_{w_1} = \begin{cases}\text{fixed: } 0.5\left(-5\cos 4\phi_0 + 4\cos 2\phi_0 + 1\right)\\ \text{pinned: } 0.5\left(-11\sin 4\phi_0 - 2\sin 2\phi_0\right)\end{cases}$$

$$A_{w_2} = \begin{cases}\text{fixed: } -\sin 4\phi_0 + 4\sin 2\phi_0\\ \text{pinned: } 3\left(\cos 4\phi_0 - 2\cos 2\phi_0 + 1\right)\end{cases}$$

This deformed shape is used as the mode shape for the equivalent SDOF and can be used to derive the transformation factors, K_M and K_L, resulting in

$$K_L = \frac{q\int_0^{\phi_0} w\,d\phi + p\int_0^{\phi_0} w\cos 2\phi\,d\phi}{w_0\left(q\phi_0 + 0.5p\sin 2\phi_0\right)} \tag{15}$$

and

$$K_M = \frac{1}{\phi_0 w_0^2}\int_0^{\phi_0} w^2\,d\phi \tag{16}$$

where w_0 = deflection at the crown ($\phi = 0$).

Note that for both the pinned and fixed arch the the work done by the uniform load component is zero. This results in an inconsistency in the case of a semi-circular arch, where $\phi_0 = 90°$ and $\sin 2\phi_0 = 0$. In this case, the load component performing work is normalized to the load component not doing work and the load transformation factor does not have a physical meaning. Due to this inconsistency the more general statement of the equation of motion has been retained.

Plastic Response

The limit capacity, deformed shape, and plastic response parameters for the arch are derived using the limit plasticity assuming the five-hinge static collapse mode as shown Figure 4. From kinematic considerations, the relationships between the vertical velocity at the crown and the rotation of the arch segments 1 and 2 are given by

$$\dot{w}_0 = r\left(\sin\phi_D\left(\frac{1-\cos\phi_0}{1-\cos\phi_D}\right) - \sin\phi_0\right)\dot{\theta}_2 \tag{17}$$

$$\dot{\theta}_1 = \left(\frac{\cos\phi_D - \cos\phi_0}{1-\cos\phi_0}\right)\dot{\theta}_2 \tag{18}$$

where $\dot{\theta}_1$ and $\dot{\theta}_2$ are the rotation rates of segments 1 and 2, respectively; and ϕ_D is the angle to the haunch hinge.

The capacity, p^*, of the arch is derived by equating the internal and external work rates (Note: the work done by the q component is zero as in the elastic case) giving

$$p^* = \frac{3M_p}{2r^2\left(1-\cos\phi_0\right)}\left(\frac{A_0 + A_1\cos\phi_D}{C_0 + C_1\cos\phi_0 + C_2\cos^2\phi_0}\right) \tag{19}$$

where

$$A_0 = \begin{cases}\text{fixed: } 2\left(1-\cos\phi_0\right)\\ \text{pinned: } 1 - 2\cos\phi_0\end{cases} \qquad C_0 = -\cos\phi_0$$

$$A_1 = \begin{cases}\text{fixed: } 0.0\\ \text{pinned: } 1.0\end{cases} \qquad C_1 = 1+\cos\phi_0 \qquad C_2 = -1$$

and M_p = plastic moment capacity of arch cross-section. Minimization with respect to ϕ_D gives

$$\text{pinned: } \cos\phi_D = \left(\sqrt{2}-1\right) + \left(2-\sqrt{2}\right)\cos\phi_0$$

$$\text{fixed: } \cos\phi_D = \frac{1}{2}\left(1+\cos\phi_0\right) \qquad (20)$$

This solution is a upper bound in that the internal work done by the membrane stresses is neglected. The effect of the existence of membrane forces is, however, accounted for in determining the plastic moment capacity, M_p, as discussed in the following section.

Resistance Function

The resistance of the arch is modeled using an elastic-perfectly plastic resistance function as shown in Figure 5, where the stiffness and maximum resistance are determined using the solutions presented earlier. The major refinement here is that the maximum resistance is allowed to vary depending on the moment-thrust combination existing in the arch at any point in time. Observations from test data [5,6] have shown that the response of the arch is generally in the compression region of the moment-thrust diagram and that the eccentricity (ratio of moment to thrust) decreases as the arch is engulfed by the ground shock. This response is illustrated in Figure 5 and is modeled by allowing the moment capacity of the arch to vary based on the weighted average of the elastic moment and thrust at the arch critical cross-sections (crown, ϕ_D and ϕ_0), as calculated using the equivalent q_e and p_e components. Since as the arch is engulfed the magnitude of the uniform component, q_e, increases relative to the nonuniform component, p_e, this will naturally increase the magnitude of the thrust relative to the moment, replicating test data observations. This can potentially result in the arch yielding at a moment magnitude less than the peak moment due to the decreasing moment capacity above the balance point.

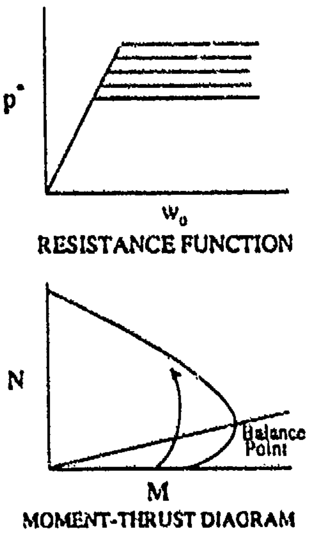

Figure 5. Resistance Function.

ADAPTATION TO CONVENTIONAL MUNITIONS

The proposed SDOF methodology can be adapted to conventional munitions for the case of an overhead burst and two-dimensional response (for example, a longitudinally segmented arch). This is accomplished by replacing the planar ground shock with a spherically propagating shock wave as illustrated in Figure 6. Assuming that the radial stress and velocity in the freefield are constant behind the shock front, the normal freefield ground shock stress and velocity are given by

$$\sigma_{ffn} = q_{ff} + p_{ff}\cos 2\left(\phi+\beta\right)$$
$$V_{ffn} = V_{ff}\cos\left(\phi+\beta\right) \qquad (21)$$

so that the external work rate is given by

$$\dot{W}_{ext} = q_{ff}\int_{\phi_R}^{\phi_S}\dot{w}\,r\,d\phi + p_{ff}\int_{\phi_R}^{\phi_S}\dot{w}\cos 2\left(\phi+\beta\right)r\,d\phi \qquad (22)$$

$$+\,\rho C_L\left\{V_{ff}\int_{\phi_R}^{\phi_S}\dot{w}\cos\left(\phi+\beta\right)r\,d\phi - \dot{u}_{RB}\int_{\phi_R}^{\phi_S}\dot{w}\cos\phi\,r\,d\phi - \int_{\phi_R}^{\phi_S}\dot{w}^2 r\,d\phi\right\}$$

Since the angles ϕ and β are related (as determined by the standoff distance), β can be solved for in terms of ϕ giving

$$\beta = \cos^{-1}\left(\frac{1}{\sqrt{\left(\frac{r}{x}\right)^2\sin^2\phi+1}}\right) = \sin^{-1}\left(\frac{\sin\phi}{\sqrt{\left(\frac{r}{x}\right)^2\sin^2\phi+1}}\right) \qquad (23)$$

and

$$\cos\left(\phi+\beta\right) = \left(\frac{\cos\phi}{\sqrt{\left(\frac{r}{x}\right)^2\sin^2\phi+1}}\right) + \left(\frac{r\sin^2\phi}{x\sqrt{\left(\frac{r}{x}\right)^2\sin^2\phi+1}}\right) \qquad (24)$$

Similarly,

$$\cos 2\left(\phi+\beta\right) = \left(\frac{2\cos 2\phi}{\sqrt{\left(\frac{r}{x}\right)^2\sin^2\phi+1}}\right) + \left(\frac{2r\sin\phi\sin 2\phi}{x\sqrt{\left(\frac{r}{x}\right)^2\sin^2\phi+1}}\right) \qquad (25)$$

Substitution of Eqns 24 and Eq.25 into Eqn 22 for the external work rate results in a radical integral considerably more complex than those for the nuclear case. Nonetheless, closed form solutions for these integrals exist so that a computer efficient model can be developed.

The loading for a conventional weapon is more localized than that for a nuclear weapon so that the deformed shape and collapse mechanism may also require modification. This can be modeled by assuming a concentrated load at the crown for the characteristic load distribution. The deformed shape and plastic limit capacity can then be derived for this characteristic loading.

STATUS AND FUTURE EFFORT

The research is currently in the final stages of the model development and programming. In addition to the refinements reported herein, models have been derived for including the effects of rise time in the loading function and for calculating the rigid body response of the arch. The elastic response is currently being expanded to include a three hinge arch (crown, supports). After programming and checkout of the model, comparisons of the model against test data from the AFWL Kachina test series [7] and the DNA/WES Dynamic Arch Test [8]. Comparisons against finite element calculations [1] and other arch SDOF models [5,9] will also be conducted.

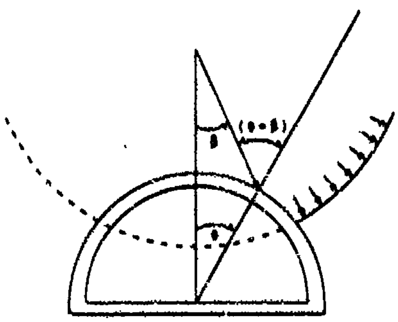

Figure 6. Adaptation to Conventional Weapon

REFERENCES

1. Bingham, B., Galloway, J. C., and Frank. R.A., "Failure Level Analysis of Buried Arches" Contract DNA001-85-C-0411, Defense Nuclear Agency, Washington, D.C., 31 May 1988.

2. Crawford, R.E., Higgins, C. J., and Bultmaness, E. H., "The Air Force Manual for Design and Analysis of Hardened Structures" AFWL-TR-72-104, Kirtland AFB, N.M.

3. Timoshenko, S.P., and J.M. Gere, Theory of Elastic Stability, 2nd Edition, Engineering Society Monographs, McGraw-Hill Book Company, 1961.

4. Drake, J.L., R.A. Frank, and M. Rochefort, "A Simplified Method for the Prediction of the Ground Shock Loads on Buried Structures."

5. Flathau, W. J., L. M. Bryant, and P. F. Mlakar, "Single-Degree-of-Freedom Analysis of Buried Arches Loaded by Conventional Ground Shock", JAYCOR, presented at The International Symposium concerning Conventional Weapon Effects held in Mannheim, West Germany, 10-13 March 1987.

6. Krauthammer, T., Flathan, W. J., Smith, J. L., and Betz, J. F., "Lessons from Explosive Tests on RC Buried Arches," Journal of Structural Engineering, Vol. 115, No. 4, April, 1989.

7. Smith, J. L., J. F. Betz, and G. T. Baird, "KACHINA Test Series: Dynamic Arch Test Three (DAT-3) Analysis Report", AFWL-TR-85-63, Air Force Weapons Laboratory, Kirtland Air Force Base, New Mexico, March, 1986.

8. Dallriva, F. D., "Data Report for FY86 Dynamic Shallow-Buried Arch Test", USAE Waterways Experiment Station, Structural Mechanics Division, Structures Laboratory, Vicksburg, Mississippi, October, 1986.

9. Auld, H. E., W. C. Dass, and D. H. Merkle, "Development of Improved SDOF Analysis Procedures for Buried Arch Structures", Applied Research Associates, Inc. for the Air Force Weapons Laboratory, Kirtland Air Force Base, New Mexico, September, 1983.

ACKNOWLEDGMENT

The research reported on is being performed as partial fulfillment of the requirements for the degree of Doctor of Philosophy (Civil Engineering) at North Carolina State University under the supervision of Dr. Ajaya K. Gupta. The author would also like to acknowledge the support of the Air Force Engineering Services Center, Air Force Weapons Laboratory, and the Defense Nuclear Agency in providing test data and the results of finite element calculations which were used to study the arch loading and response phenomenology.

EXPEDIENT HARDENING METHODS FOR STRUCTURES SUBJECTED TO THE EFFECTS OF NON-NUCLEAR MUNITIONS

Robert H. Sues, Charles E. Murphy, William C. Dass, Lawrence A. Twisdale

Applied Research Associates, Inc.
Raleigh, North Carolina 27615

ABSTRACT

A study has been conducted to investigate expedient methods for hardening existing structures and exposed assets against the effects of conventional weapons. The expedient hardening methods covered in this paper are soil berms, sandbagging, sand grids, concrete modular revetments, bin revetments, and sacrificial panels. For each of the methods the paper gives a short description of the method including threat protection afforded, a summary of available test results, limitations of the method and special considerations required for deployment.

1. INTRODUCTION

In peacetime or wartime situations, needs can arise to upgrade the hardness of an existing facility in an expedient fashion. This may be due to a change in function of the facility (e.g., relocation of important assets to the facility), an increase in the perceived importance of the facility, or an increase in the expected threat. A study has been conducted to investigate both traditional and newly developed methods of expedient hardening and to develop guidance for designers. The expedient hardening methods covered in this paper are: soil berms, sandbagging, sand grids, concrete modular revetments (aircraft, Bitburg, SIFCON), bin revetments, and sacrificial panels. For each of the methods investigated, the paper presents a short description of the method including threat protection afforded, a summary of available test results, limitations of the method and special considerations required for deployment. The complete results of this study can be found in the expedient hardening addendum to the Air Force Manual for the Design of Protective Structures for Conventional Weapons Effects (ARA, 1988). The addendum includes methods not covered herein, design guidance, and a selection roadmap to aid in making optimal selections.

2. SOIL BERMS

General. Berms are employed as free standing structures or constructed against walls. A bermed wall configuration is shown in Figure 1.

Threat Protection. Berms provide protection against near miss general purpose bombs, high explosive rounds, and ballistic penetration (USOCD, 1941). As free standing walls, berms can be used to deny a direct line of sight to a protected asset or a vulnerable area such as a door opening.

Recent tests on berms include the CHEBS series conducted at Kirtland AFB (Hyndman, 1987) and the NATO tests conducted at Tyndall AFB (Hyde, 1989). The CHEBS tests included free standing, full scale reinforced concrete revetments that were both bermed and unbermed. The environment was provided by a nose tangent MARK 83 general purpose bomb, statically detonated at a standoff of 50 feet. The NATO test examined the effectiveness of a bermed semi-hardened reinforced concrete wall subjected to the NATO GP bomb threat. In both tests, no damage was reported to the bermed structures, while the unbermed structures suffered significant front face cratering and backface spall. Significant airblast protection was also demonstrated in these tests. The CHEBS tests showed a reduction of about 93% in peak wall pressures (at the berm-wall interface); the NATO test showed similar reductions in peak wall pressures. Because of the reduced wall pressures, the risk of spall and breach are greatly reduced (even though total impulse delivered remains relatively unchanged). It must be cautioned, however, that if the weapon penetrates the berm prior to detonation, the coupling between the explosion and the surrounding soil can result in wall pressures greater than for an unbermed wall. Also, in a free standing configuration, a berm provides little airblast protection. This is because the blast wave reforms behind it after passing over the top. This was demonstrated by studies made during the CHEBS tests. The tests demonstrate that berms provide excellent second or multiple attack protection.

Limitations/Special Considerations. The main disadvantage of free standing berms and to a lesser extent bermed walls is their large space requirements. Berming may not be a practical hardening option for structures sited in very rocky terrains or where grading equipment is not available. At air base facilities, berms sited near taxiways and runways may exacerbate problems related to blowing dust and foreign debris. Erosion control measures are particularly important under these circumstances. Typical facings used to control erosion include sod, sandbags, and asphalt cutback. Generally, structures that were originally designed to withstand loadings associated with weapon effects have ample capacity to support additional dead loads associated with berming. This is not the case for conventional structures and analysis is required to determine the need for additional support.

3. SANDBAGGING

General. Sandbagging is a traditional method of providing effective protection to walls, overhead structures, and revetments (DOA, 1985; Hoot, et al., 1974). Sandbags can also be used to construct free standing walls and wall structures for protection of otherwise exposed assets. Figure 2 shows a sand bag upgrade of an existing structure.

Threat Protection. Several test series conducted by the U.S. Army Waterways Experiment Station (WES) have demonstrated that sandbags placed against walls and over roofs are successful in protecting against near miss and direct hit high explosive rounds, and direct ballistic impacts (Hoot, et al., 1974; Bucci and Mlakar, 1976; Hamlin, 1986). Placed against walls, sandbags provide protection similar to that obtained from berming with soil.

In one series of tests (Hoot, et al., 1974), a timber framed roof structure protected by 4 layers of sandbags (16 inches of cover) was not breached by contact detonations of an 82 mm mortar, 107 mm rocket, or a 122 mm rocket. Similar tests of 6 inch thick precast reinforced concrete roof panels also demonstrated the effectiveness of sandbagging. An 82 mm mortar round detonated directly against the slab caused major spalling on the interior surface. A 107 mm rocket round caused massive spalling and breached the slab. With two layers of sandbags covering the roof, the test using the 107 mm rocket was repeated with only minor cracking occurring on the interior face. A 15 inch layer of sandbags stacked against a 6 inch precast wall provided good protection against a 155 mm HE artillery round detonated at a standoff of 5.0 ft. A similar unprotected wall was decimated by the round. Sandbag berms, wall and roof coverings provide multiple attack protection to near miss high explosive threats similar to soil berms or soil covers.

Limitations/Special Considerations. The main limitation of sand bags is aesthetics and for this reason, sandbagging is generally not considered an acceptable approach for more permanent upgrades. Sandbags have had a history of susceptibility to rot, however, newer bag materials made of an acrylic fabric are available and are reported to remain serviceable for over 2 years with no signs of deterioration under all climatic conditions (DOA, 1985). Improved performance against ballistic penetration is obtained by mixing the fill material with dry portland cement (1 part cement to 10 parts soil) or dipping the filled bags in a cement-water slurry (DOA, 1985).

4. SAND GRIDS

General. Sandgrids were originally developed as a soil confining system for use in roadway construction over loose soils. Sandgrids are constructed by filling a prefabricated plastic form shaped like cells of a honeycomb with a granular material such as sand or gravel (Figures 3, 4). The sand grids are available in a standard configuration or a newer, notched configuration. The notched configuration allows for development of a lapped joint between layers that prevents leakage of the fill material. The principal advantages over the more traditional methods of hardening with soil are ease of construction and reduced space requirements. Currently available sandgrids are 38 inches wide in place.

Threat Protection. Testing has demonstrated that sandgrids can provide efficient and effective protection against near miss general purpose bombs, high explosive artillery rounds, shoulder launched rockets, and machine gun fire (White, 1983; Wood, 1985; Hamlin, 1986; Hayes, 1987, 1988; Hyde, 1989).

Recent tests conducted on the NATO test facility demonstrated that sandgrids are very effective in protecting semi-hardened walls from near miss general purpose bomb fragments and airblast (Hayes, 1988; Hyde, 1989). In this test a 65 cm wall protected by a sandgrid shield (Figure 4) suffered no damage from a GP bomb detonation. The same wall, unprotected, suffered severe spall when subjected to the same weapon at the same standoff.

Wood (1985) reports the results of tests on free standing sandgrid revetments against 105 mm flechette artillery rounds, 155 mm HE airbursts, and 155 mm surface bursts. Six 105 mm flechette rounds were detonated 120 ft from the target. None of the flechettes completely penetrated the revetment. Six standard D544 fragmentary HE rounds were detonated at a stand off of 40 ft and an elevation of 20 ft. The revetment remained stable and erect and showed slight deterioration. There was no evidence of fragments passing through the sandgrid. Six 155 mm rounds each were statically detonated, nose tangent, at ranges of 5, 10, and 15 ft from the test revetments. At the 5 ft range, the six rounds totally collapsed the revetment. Good fragmentation protection, however, was provided for the first two rounds. At the 10 ft range, after six rounds, the sandgrid revetment remained intact and erect but the top three layers were significantly damaged. No fragments penetrated through the revetment. The six rounds fired at the 15 ft range caused only superficial damage. Sandgrid revetments have also demonstrated effectiveness in defeating penetration by small arms fire up to 50 caliber rounds (White, 1983).

Gravel filled sandgrid revetments have been tested against U.S. LAW and Soviet RPG-7 antitank weapons (Hayes, 1988). Crushed limestone (3-4 in. diameter) was used for the revetments tested against the LAW, and rounded river gravel (1.5-2 in. diameter) was used for the revetment tested against the RPG-7. Two consecutive hits by LAW rounds, in approximately the same location, cratered the front face of the revetment but the revetment was not perforated. The revetment hit by the RPG-7 was perforated by the rocket motor, but the residual velocity of the motor was not sufficient to cause damage to a protected wall or lightly armored assets placed behind the revetment.

Sandgrids filled with sand and gravel have also been tested against a wire guided warhead (TOW) placed against the side of the revetment and statically detonated (Hayes, 1988). The sand filled revetment was breached by the weapon and the steel witness plate behind the revetment was perforated. The gravel filled revetment was breached and fragments from the weapon perforated the revetment; however, the witness plate was not damaged.

Sangrid revetments provide limited second attack protection from near miss GP bombs based upon evidence from the NATO test facility. The sandgrid form was severely damaged, however, much of the soil remained in the shape of a small berm. In other applications against less severe threats such as near miss HE artillery rounds, the sandgrid revetment provides excellent second attack protection. As overhead protection, sandgrids provide limited second attack protection against direct hit mortar and HE artillery attack but can be repaired with loose soil or sand bags.

Limitations/Special Considerations. The maximum free standing height for use as a protective structure against conventional weapons is about 8 ft.

5. CONCRETE MODULAR REVETMENTS

General. The discussion in this section focuses on several modular designs constructed of conventionally reinforced concrete (R/C) and SIFCON (Slurry Infiltrated Fiber reinforced Concrete) that have been tested. Figure 5 shows one common type of modular unit. The revetments are often bermed by soil to improve overall performance (see Section 2 and Figure 1).

Threat Protection. These revetments provide protection against fragments and airblast from near miss general purpose bombs and other lesser threats such as HE artillery rounds, rockets, and mortars. Also, they are often used to deny line-of-sight to doors and other vulnerable openings.

Recent tests on R/C revetments include the CHEBS series conducted at Kirtland AFB (Hyndman and Bulman, 1987; Carson and Morrison, 1986) and the NATO tests conducted at Tyndall AFB (Hyde, 1989). The CHEBS tests included revetments that were both bermed and unbermed (see Section 2). In the CHEBS 9 and 10 tests four standard revetment designs were tested in a variety of configurations: (1) the Bitburg Revetment with a wall thickness of 0.30 m, (2) the 3-meter Aircraft Revetment with a wall thickness of 0.245 m, (3) the 4-meter Aircraft Revetment with a wall thickness of 0.245 m, and (4) the 4-meter Aircraft Revetment with a wall tapering from 0.245 m at the base to 0.085 m at the top. A second series of tests (CHEBS 16) was conducted using similar designs constructed using SIFCON (Carson and Morrison, 1986). The NATO test examined the effectiveness of unbermed Bitburg revetments subjected to the NATO GP bomb threat. R/C revetments have also been tested against a variety of other conventional weapons including HE rockets, mortars, and machine gun fire (Hoot, et al., 1974).

The results of the CHEBS and NATO tests demonstrated that unbermed R/C revetments can provide good first strike protection but limited second attack protection due to their susceptibility to fragment damage and movement (i.e., rigid body shifting). As bermed structures, R/C revetments provide excellent second attack protection.

For the revetments constructed of SIFCON, the general damage characteristics resulting from fragment impact differed significantly from the damage characteristics of the R/C revetments. The damage on the front face of the SIFCON revetments tended to be localized immediately around the impact area and not cratered as was the case with the R/C revetments. Little or no rear spall occurred with the SIFCON revetments. When the revetments were perforated by fragments, the penetrations were clean, nearly cylindrical and easily repaired.

R/C revetment panels 6 inches thick and supported by precast blocks (Hoot, et al., 1974) were demonstrated to be effective against 81 mm mortars and 120 mm rockets detonated at a standoff of 5.0 ft. Against 155 mm HE artillery rounds the 6 inch panel was considered to be effective only for standoffs greater than 30 ft. Against 122 mm rockets, the revetment was considered satisfactory for standoffs of 10.0 ft; and with the addition of a 15 inch sandbag facing, the revetment defeated the fragment effect at a 5 ft standoff.

Limitations/Special Considerations. R/C revetments are limited by the resources necessary to fabricate and deploy them. Their use as an expedient measure requires that they be prefabricated and available for deployment. Modular, prefabricated revetments require a relatively smooth base surface for deployment. Bermed, R/C revetments have fairly large space requirements and other limitations associated with soil berms or bermed walls (see Section 2). The geometry of the Aircraft Revetment does not allow for the formation of ninety degree turns in the layout of an array of revetments. The base of the Bitburg revetment has corners mitered at 45 degrees which allow for ninety degree turns, but these corners are vulnerable to fragment penetration because the wall thicknesses of the two revetments just meet and do not lap. These corners should be protected with sandbags.

6. BIN REVETMENTS

General. Bin revetments refer to any of a variety of methods used to create vertical walls of sand, soil, gravel, or rock rubble. These systems combine the protective qualities of soil structures with an efficient use of space. The thickness of the soil wall is the primary means of providing protection. The structural system is designed to confine the soil and can be constructed of reinforced concrete, steel, wood or wire caging. Typical configurations are two parallel walls with fill between them or prefabricated containers filled with soil and arranged into a revetment (Figure 6). In addition, bin revetments can take the form of planters for aesthetic permanent upgrades.

Threat Protection. These revetments provide essentially the same protection as bermed walls or revetments. They can be employed against fragment and airblast threats from near miss general purpose bombs, other lesser conventional munitions, and ballistic threats. They can also be used to deny line-of-sight to doors and other vulnerable openings.

Soil bin revetments with a soil thickness of 12 inches were tested by WES for protection against near miss mortar and rocket detonation in support of the U.S. Army during the Vietnam conflict (Carre, 1969, 1972). Soil bin structures constructed of plywood, 18 gage corrugated metal, and M8A1 landing mats were tested. The M8A1 soil bin defeated all fragments from 81 to 120 mm mortars and 107 mm rocket detonations at a stand off of 5 ft. The plywood and corrugated metal bin revetments were also effective at a range of 5 ft but suffered greater damage.

As a part of the CHEBS 9 and 10 tests (Hyndman and Bultman, 1987), a soil bin revetment was constructed using two parallel rows of 3 m Aircraft revetments (see Section 5). The soil thickness was approximately 5 ft. The soil bin was positioned 50 ft from a 1000 lb GP bomb. The face of the front Aircraft revetment was severely damaged by the fragment impacts but no damage to the rear revetments forming the soil bin was reported.

C & C Chamber revetments were tested as a part of the NATO facility tests (Hyde, 1989). This soil bin structure makes use of off-the-shelf precast concrete manhole liners (rectangular tubes 3.0 x 4.5 ft in section, 2.46 ft long, with a wall thickness of 3 inches). The tubes allow for a soil thickness of 2.5 ft. Several reinforcing methods were tested including wire mesh, synthetic and steel fibers and various combinations. Revetment walls were constructed by bolting the tubes together with steel straps and filling the units with sand. Walls one, two, and three layers high were tested. The tests demonstrated that this configuration can provide fragment protection against general purpose bombs. If reinforced with steel mesh, multiple attack protection can be expected.

Limitation/Special Consideration. Soil bin revetments generally require significant construction resources. If built of expedient materials, they tend to be temporary measures. Constructed of reinforced concrete or masonry, they are usually part of permanent upgrades or new facility construction.

7. SACRIFICIAL PANELS

General. Sacrificial panels are panels attached to the exterior of a main structural wall so that an air space is left between the main wall and the panel. The panels are not expected to survive a weapons blast but still provide significant protection to the main wall (Figure 7). Sacrificial panels constructed of a variety of materials such as reinforced concrete, steel plate, plywood, or a layered combination of materials have been tested. Sacrificial panels are used for both expedient upgrading of existing facilities and as inexpensive hardening methods for new construction.

Threat Protection. Sacrificial panels have demonstrated effectiveness in protecting against fragments and airblast from near miss general purpose bombs and HE rounds. Recent tests include a series of 19 scaled tests on a variety of panel types (reinforced concrete, steel, plywood, and composite) conducted by the AFESC and the WES (McVay, 1988), the full scale NATO tests conducted at Tyndall AFB (McVay, 1988; Hyde, 1989) and a series of tests on concrete panels conducted by WES (Colthorp, 1987).

In all of these cases the damage to the walls protected by the sacrificial panels was greatly reduced from the damage observed for the unprotected walls. For example, for a wall protected by a 6 inch precast panel with a nominal 1 inch air space at the full scale NATO test, only minimal scabbing and cratering occurred on the front face of the main wall and no spall occurred on the backface. The same wall tested bare suffered severe spall damage that would have been lethal to equipment and personnel inside. The mechanism behind the protection afforded is due to the greatly reduced number and momentum of the fragments that impact the main wall and greatly reduced peak pressures on the main wall. This results in a much lower potential for spall and breach even though load duration from airblast may be greatly increased.

Limitations/Special Considerations. The main limitation of sacrificial panels is their single-hit-only capability. If multiple hit capability is required a system must be in place to provide for expedient replacement of the panels.

8. CONCLUSIONS

A wide range of methods may be used to provide expedient structural hardening against the effects of conventional weapons. These methods vary in the degree of protection afforded, multiple strike capability, ease of construction, and ease of deployment. Optimal selection of a hardening method requires careful consideration of each of these factors as they relate to the particular needs of a given situation and the resources available. From the test data reviewed the most effective protection is provided by earth structures. Earth structures can significantly reduce the effects of fragments and airblast and can provide excellent multiple strike protection. Confining the earth through the use of bags, sand grids, or bins eliminates many of the limitations associated with traditional berms. Sacrificial panels and unbermed concrete revetments also provide effective protection but do not provide the multiple hit capability of earth structures.

9. ACKNOWLEDGEMENT

This work was supported by a contract from the Air Force Engineering and Services Center, Tyndall AFB, Florida.

10. REFERENCES

Applied Research Associates, Design of Protective Structures for Conventional Weapons, ARA 5460, Draft Final, 1988.

Bucci, D.R., Mlakar, P.F., Design of Earth-Covered Structures To Defeat Contact Burst Rounds, WES TR-N-76-7, 1976.

Carre, G.L., Application of Field Available Materials to Fortifications, WES TR-NH-74-4, May 1974.

Carson, J., Morrison, D., The Response of SIFCON Revetments to a Mark 83 General-Purpose Bomb, AFWL-TR-86-42, 1986.

Carson, J. et al., The Ballistic Performance of Slurry Infiltrated Fiber Concrete, AFWL-TR-86-103, 1987.

Colthorp, D.R., Ball, J.W., McVay, M.K., "Effectiveness of Sacrificial Panels in Reducing Blast and Fragment Loads," Third INMS Symposium, 1987.

Department of the Army, Survivability, FM 5-103, 1985.

Hayes, P.G., Expedient Field Fortifications Using Sand-Grid Construction, WES TR-SL-88-39, 1988.

Hamlin, A.T., Fortification Overhead Protection Using Sandgrid Construction, WES, Misc. Paper SL-86-4, 1986.

Hoot, B.B., et al., Evaluation of Field Fortifications, WES TR N-74-5, 1974.

Hyde, D., The NATO Semi-Hardened Facility Full-Scale Test Program, WES TR-89-06, Draft Final 1989.

Hyndman, D., Bultman, E., Bitburg and Aircraft Revetment Tests - Conventional High-Explosives Blast and Shock (CHEBS) Tests 9 and 10, AFWL-TR-86-46, 1987.

Marchand, K.A., and Ross, C.A., The Response of Sandbag Barriers to Blast and Fragment Loadings, U.S.Army CERL 1987.

McVay, M.K., Systems for Sheilding Aboveground Structures from Bomb Fragments and/or Airblast, WES, Draft 1988.

National Defense Research Committee, Effects of Impact and Explosion, Volume 1, Ofc Sci Res Dev, Wash., D.C., 1946.

Schneider, B. and Mondragon, R., Design and Construction Techniques for SIFCON, AFWL-TR-88-XX, 1988.

United States Office of Civil Defense, Report of Bomb Tests on Materials and Structures, 1941.

White, R. W., Field Artillery Emplacements Development and Weapons Effects Evaluation, WES, TR-SL-83-1, 1983.

Wood, W.S., The Effects of Blast and Flechette/Fragment Penetration on Field Fortifications, WES, Misc. Paper SL-85-2, 1985.

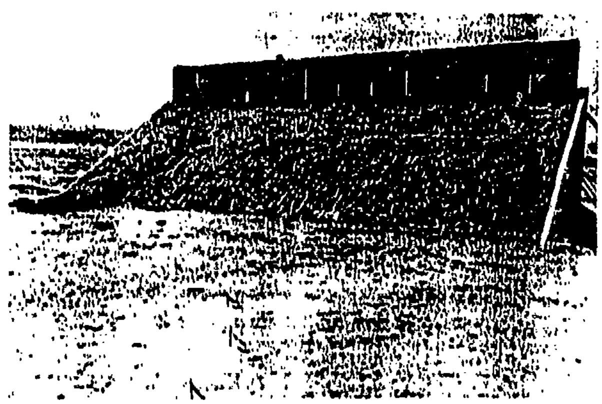

Figure 1. Bermed Wall

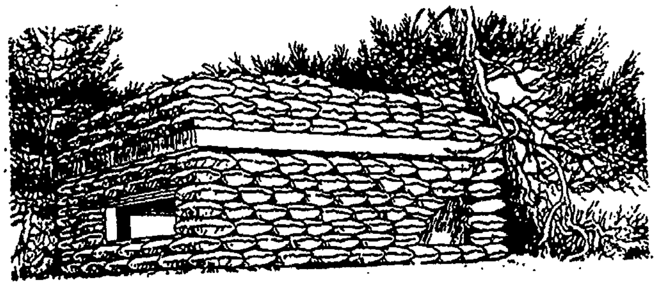

Figure 2. Sandbag Upgrade

Figure 3. Sand Grid Section

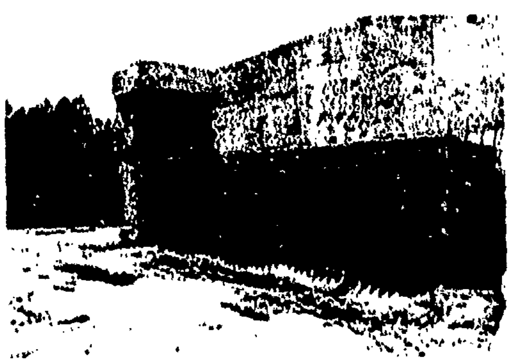

Figure 4. Sand Grid Revetment

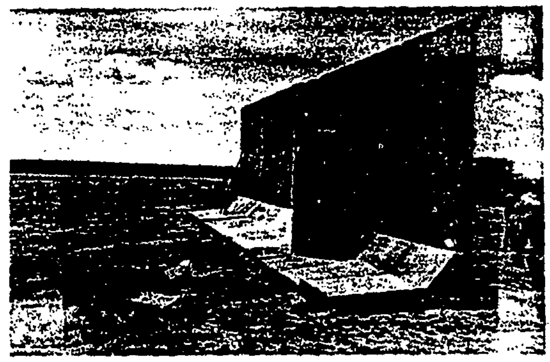

Figure 5. Four-meter Aircraft Revetment

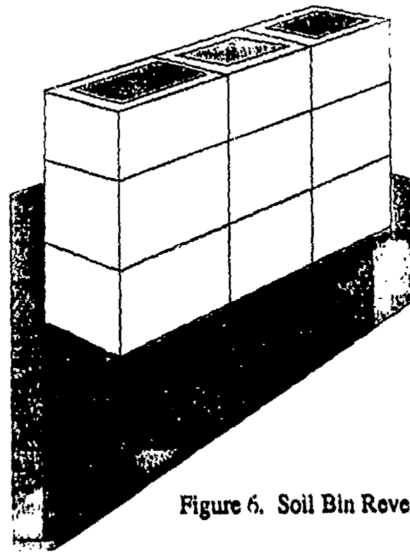

Figure 6. Soil Bin Revetment

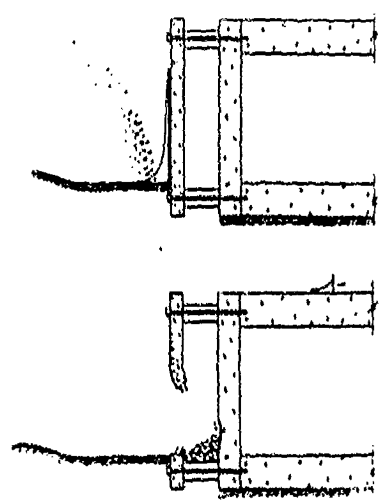

Figure 7. Sacrificial Panel

BLAST RESISTANCE OF A POLYCARBONATE WINDOW

David L. Tilson and James M. Watt, Jr.

US Army Engineer Waterways Experiment Station (WES)
Vicksburg, Mississippi

ABSTRACT

High explosive threats directed against U.S. facilities throughout the world have identified a need to blast harden these facilities. Lose of windows during blast loading poses a serious threat to personnel and facility security. Research has shown that a blast resistant window is feasible and that a single-degree-of-freedom (SDOF) analysis can predict the window response.

The WES generic blast resistant window was designed to withstand a peak reflective pressure of 80 psi. This window survived the test with no damage. The SDOF predictions for the 26-inch by 26-inch windows were in good agreement with test data, with the analysis being conservative. This good agreement resulted from the use of a resistance function developed from a static test.

INTRODUCTION

High explosive threats directed against U.S. facilities throughout the world have identified a need to blast harden these facilities. One of the most vulnerable elements in these structures is the window systems. Lose of windows during blast loading poses a serious threat to personnel and facility security. Research has been funded for the purpose of designing a generic window system to withstand high blast pressures. From this research, it was shown that a window system can be designed to resist high blast pressures and that the dynamic response can be predicted with a single-degree-of-freedom (SDOF) analysis.

WES BLAST WINDOW

The WES generic blast resistant window was designed to withstand a peak reflective pressure of 80 psi. The window was designed in three parts; the anchoring frame, which is cast into the reinforced concrete test wall, a rigid window frame, and 1-1/4-inch-thick polycarbonate glazing. Figure 1 shows a schematic view of the design concept.

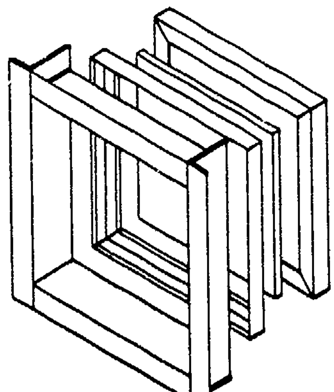

Fig.1

The critical element in designing the anchoring frame was to develop a large shear area across the thickness of the concrete test wall. The frame was designed to be positioned in the wall and cast in place, thereby, developing a shear area 1.5 times larger than the thickness of the wall (12-inches thick). The anchoring frame was fabricated using 4-inch by 8-inch by 1/2-inch thick steel angle with a minimum yield stress of 36,000 psi. To anchor the frame into the concrete, 5/8-inch diameter by 8-inch-long concrete anchors were welded to the frame. These anchors were attached to the frame at a centerline spacing of 4-inches. The frame was positioned and #3 steel reinforcing bar stirrups were added in the high shear region of the slab adjacent to the frame.

The test wall consisted of two layers of 5\8-inch-diameter reinforcing bars placed 5-inches on center in both directions and in both faces of the slab. The shear stirrups were added for a distance of 1 foot from the anchor frame. The concrete design used in the test wall had a minimum yield (f'_c) of 5000 psi at 28 days.

The window frame was designed to be structurally rigid; therefore, the remaining critical elements in the design of the window were the bite placed on the glazing and the type glazing used. The frame was fabricated using 4- by 3- by 1/2-inch steel angle, with the 4-inch edge providing the bite of the glazing. Figure 2 shows the design of the window frame. With this design, a bite of 1-1/4-inches was placed on the glazing.

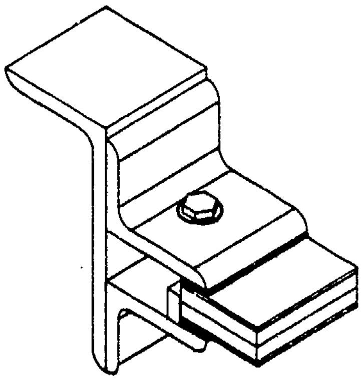

Fig. 2

The glazing selected for the window was 1-1/4-inch laminated polycarbonate (SP-1250). This material was selected for its ability to undergo large deflections and remain undamaged. The SP-1250 contains four layers of polycarbonate consisting of two - 1/2-inch layers placed in the center and two - 1/8-inch layers placed on the outside.

ANALYSIS

The determination of the dynamic response of a simple structural system using numerical procedures is presented in detail in References 1, 2, and 3. More complex systems, such as the window system reported herein, can also be analyzed with an SDOF, provided an accurate representation of the load function P(t), resistance function (load-deflection curve), and mass (M) can be obtained.

SDOF Analysis

The selection of the idealized spring-mass system in Figure 3a is such that the deflection of the mass, y, is the same as the centerline deflection of the window glazing. From the freebody diagram shown in Figure 3b, the equation of motion is derived and then solved numerically.

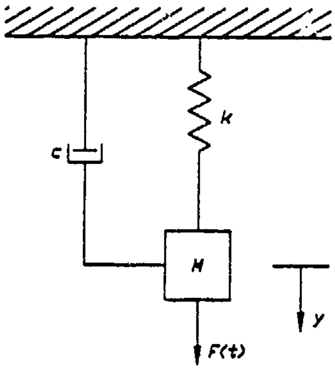

Fig. 3a

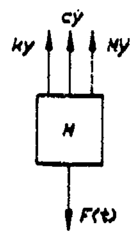

Fig. 3b

To solve for the dynamic response of the window, a static test was conducted to determine the resistance function, the P(t) was calculated from formulas developed in Reference 2, and the mass of the polycarbonate glazing was determined. Once these three values were obtained, the use of a computer code (SDOF) developed at WES was utilized in preforming the analysis.

Static Test Device

To conduct the static testing, WES designed and constructed a static test device as shown in Figure 4. The test device was designed to subject a test article to a maximum hydrostatic pressure of 200 psi. The parts of the device consist of a U-framed base, a test wall slab, and the hold-down slab.

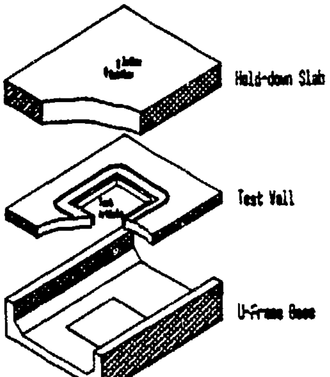

Fig. 4

This test device allows for the testing of a window as if the test article were installed in a building wall. Once the window is installed, the test wall is positioned on the U-frame base and the hold-down slab positioned on top. The two slabs are then bolted together. In this configuration, a chamber is formed between the window and the bottom of the hold-down slab. It is into this chamber that water is pumped to produce the uniform hydrostatic pressure. A maximum of 300 psi has been achieved with this setup.

By utilizing the U-shaped base, access to the underside of the window is possible and placement of instrumentation can be accomplished. The design also allows clearance for videotape equipment to be used in recording the response of the test article.

Static Testing

The window system was subjected to a hydrostatic pressure that produced failure of the window. Failure is taken to be the point where the glazing or window system cannot sustain additional load. In the test conducted, the failure mechanism for the window was the glazing slipping from the frame bite. With the data collected on the pressure and centerpoint deflection, a load-deflection curve was derived for the analysis. Figure 5 shows the resistance function developed from the test data.

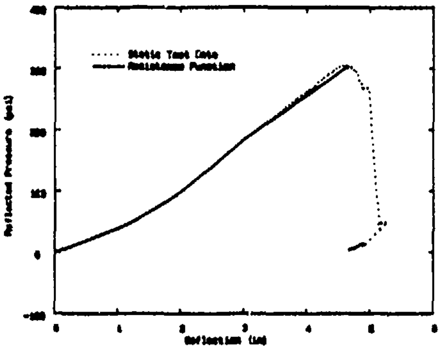

Fig. 5

SDOF Code

The procedure used in the SDOF code is described in Reference 1. The procedure is referred to as the constant-velocity or lumped-impulse procedure. The code requires the following information to perform the calculation: mass (M), area (A), load-mass factor (K_{LM}), percent of damping (c), time step (d_t), resistance function f(R), and forcing function P(t).

In the analysis of the window system, the mass was determined by weighting the glazing. The area was selected as the clear span area of the window (26 inches by 26 inches). The values for the load-mass factor and percent of damping were chosen to be 0.67 and 0.03, respectively. The numerical iterative time step of 0.0001 seconds was used for the SDOF calculation.

The analysis was performed by using a reflected pressure-time history, with clearing time, for a hemispherical high-explosive (HE) charge producing a peak pressure of 52.6 psi. The negative phase peak pressure was -4.0 psi. Figure 6 shows the calculated pressure-time history.

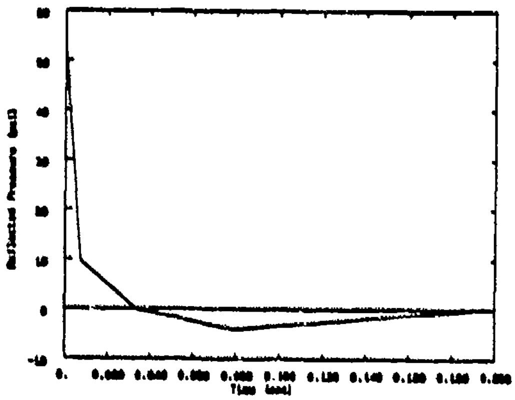

Fig. 6

Utilizing the input data, the SDOF analysis was conducted.

DYNAMIC TEST

To verify the analysis, a dynamic test was conducted on five WES blast windows. The window clear span openings were two - 26-inch by 26-inch, two - 36-inch by 36-inch, and a 40-inch by 40-inch.

The test was conducted and subjected the two 36-inch by 36-inch to an average peak reflective pressure of 49.2 psi and the two 26-inch by 26-inch and the 40-inch by 40-inch windows to an average peak reflective pressure of 57.4 psi.

COMPARISON OF CALCULATED RESPONSE AND TEST DATA

In determining the dynamic response of the three sizes of blast windows, an analysis was performed using the static load-deflection curve generated for the 26-inch by 26-inch window and a theoretical resistance function calculated for the 36-inch by 36-inch and 40-inch by 40-inch windows. The theoretical resistance functions were generated from equations developed in Reference 1.

The analysis predicted a centerpoint deflection of 1.81 inches for the two 26-inch by 26-inch windows, 6.1 inches for the two 36-inch by 36-inch windows, and greater than 10 inches for the 40-inch by 40-inch window. A comparison of the pretest prediction and actual test data is shown in Table 1.

Table 1 Summary of Deflection Data for WES Blast Windows

Window Sizes and Type PC	Predicted Deflection with SDOF (in)	Test Data Summary (in)
26x26 New PC	1.84	1.30 1.35
26x26 Old PC	1.84	1.32 1.34
36x36 New PC	6.1	3.25 3.10
36x36 Old PC	6.2	2.92 3.15
40x40 New PC	10	4.00 3.98

From comparison of the results from the test, it appears that revision of the calculated resistance functions will be required. The test data shows that the polycarbonate glazing has a higher stiffness (resistance) than predicted by the theoretical resistance function.

A posttest analysis was performed using the data from the 26-inch by 26-inch window. The pressure-time history used in the analysis was the average of the records from the six pressure gages used in the test. From this analysis the peak centerpoint deflection was calculated to be 1.58 inches. Although this comparison is based on one test, it is concluded that the proposed procedure can be used to verify or determine the blast resistance of a window system. The good agreement between the predicted value and actual test data suggests that the resistance function developed from static testing correctly described the spring (k) of the SDOF system.

The poor agreement of the predicted spring (k) and test response data indicates that the boundary conditions are more complicated than assumed for the theoretical resistance function. This is one area where further studies are needed.

ACKNOWLEDGMENTS

This research was sponsored by the U.S. Department of State, Physical Security Branch, Washington D.C., under the project entitled "Blast Standards Verification Program." The technical monitors were Messrs. Larry Binner, Jerry Felt, and Gerald Meyers. The work was accomplished by the US Army Engineer Waterways Experiment Station (WES), Structures Laboratory, Structural Mechanics Division. Project Manager was Mr. James M. Watt, Jr. (WES). The Project Engineers were Messrs. David L. Tilson and Lebron Simmons. We gratefully acknowledge permission from the Chief of Engineers to publish this paper.

REFERENCES

1. Biggs, John M., "Introduction to Structural Dynamics," McGraw-Hill Book Company, New York, 1964.
2. "Fundamentals of Protective Design for Conventional Weapons," Technical Manual 5-855-1, Department of the Army, Washington, D.C.
3. "Structures to Resist The Effects of Accidental Explosives," Technical Manual 5-1300, Department of the Army, Washington, D.C.

FINITE ELEMENT MODELING OF UNPROTECTED STRUCTURES USED IN CONVENTIONAL WEAPON EFFECTS TESTS

Mark Amend and Carlos Coe
MSD/ENYW The BDM Corporation

ABSTRACT

Finite element modeling is an analysis technique which is commonly used in the design and analysis of structural systems. The approach has been applied in conventional weapon effects research particularly in the detailed analysis of structural subsystems and components. Limited studies have been conducted using finite element models to simulate the complete structural system subjected to conventional weapon effects. This paper addresses the analysis of three-story pre-cast and reinforced concrete structures subjected to interior detonations of general purpose bombs.

TEST SERIES DESCRIPTION

In support of OSD tri-service requirements, AFATL and 3246 Test Wing conducted a test series which addressed the effects of general purpose air delivered munitions against standard office building construction. Specifically, the tests involved three-story structures: two of which were constructed using pre-cast concrete panels and the third representing cast-in-place reinforced concrete construction. Figure 1 shows an isometric view of the test structures while Figure 2 illustrates the floor layout and building dimensions. All wall elements consisted of 6-inch thick reinforced concrete. The pre-cast panels were assembled and fastened using standard pre-cast construction techniques including the use of weld plates as the connection type between panels. Figure 2 also shows that each building was constructed in two segments with a dividing wall in the center. The only structural connection between the two building halves was the foundation system. Separating the buildings into two separate sections allowed testing to be conducted on each building section.

The tests were conducted using dynamic and static placement of the test weapon. For dynamic placement tests, a rocket sled track propelled the weapon into the first floor of the structure. The weapon fuzing was designed such that the weapon penetrated the building and detonated in the first room as shown by the weapon trajectory line in Figure 2. In the static tests, the event consisted of placing the munition in the desired room and then remotely detonating the weapon.

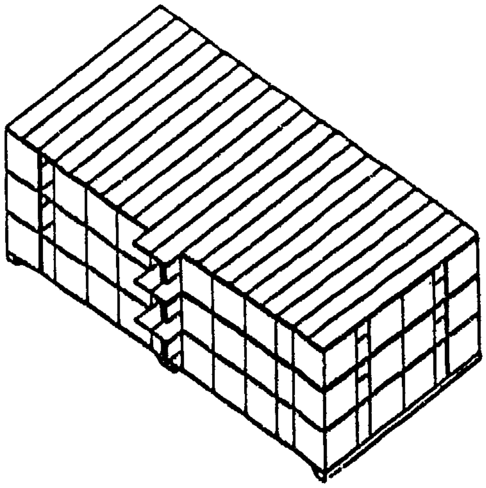

Figure 1: Test Structure Exterior Perspective

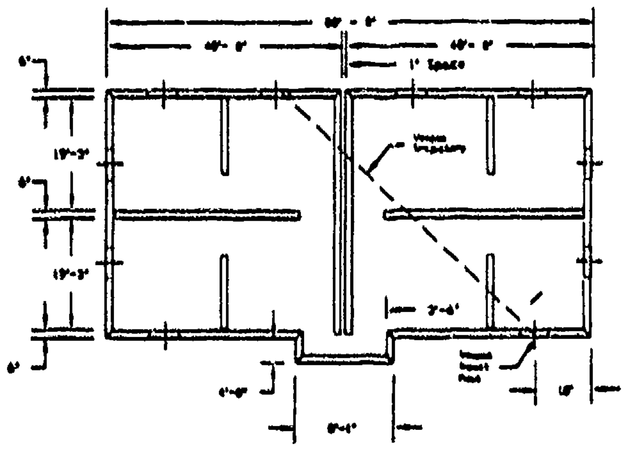

Figure 2: Test Structure Floor Plan

In several of the events, the test structures were instrumented with accelerometers and pressure transducers. The transducer array was designed to monitor the weapon loading on the structure, structural response, and the documentation of the interior environment. In addition to the instrumentation array, exterior and interior cameras documented the building collapse/damage and the interior building environment. In selected events, the test structure interior included office furniture, computer equipment, and test manniquins.

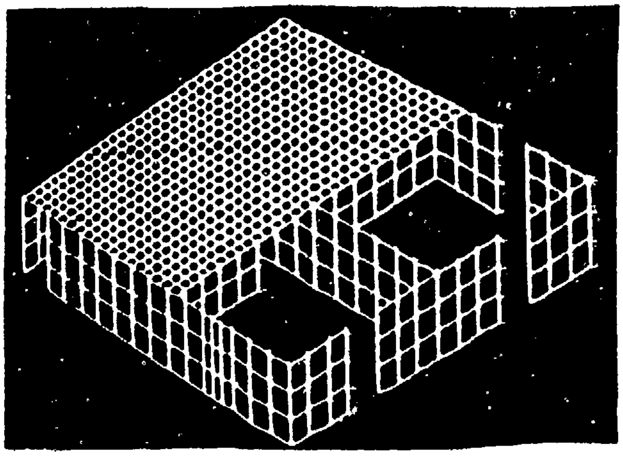

Figure 3: First Floor Segment of Test Structure Finite Element Model

ANALYSIS OVERVIEW

A parallel effort to the test series was the finite element modeling of the test structures. The intent of the study was to identify aspects of the finite element modeling that seemed promising and, more importantly, limitations and other areas requiring further development. A second purpose of the analytical study was to support the test instrumentation setup by providing pre-test predictions.

The analysis effort consisted of two general phases: pre-test modeling effort and the post-test analysis. The pre-test analysis centered on providing the pre-test predicting for the instrumentation system and included the development of models for the entire structure, substructure systems, and components. The pre-test modeling effort used COSMOS[1] a general purpose finite element code. The post-test analysis focused on analyzing selected substructure systems and components using ADINA[2] (Automatic Dynamic Incremental Nonlinear Analysis) finite element code. The post-test analysis included nonlinear material models and direct comparisons with test results.

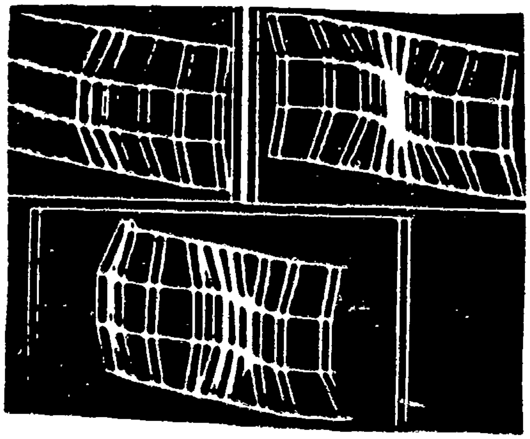

Figure 4: First Three Mode Shapes For Wall Panel Subsystem

PRE-TEST ANALYSIS

The primary task in the pre-test analysis was the development of finite element models for the entire structure, substructure systems, and components. Figure 3 shows the first floor segment of the entire structure finite element representation. The models were developed using COSMOS interactive environment and were constructed using wall and floor panels as the basic building blocks for the mesh. Connectivity between the wall and floor panel finite element blocks replicated the connection between the wall and floor panels in the pre-cast test structure. For the cast-in-place structure model, the finite element mesh represented a monolithic structural system. The substructure models represented a series of wall or floor panels while the component models consisted of single wall or floor panels. In each case, the natural frequencies and mode shapes of the finite element models were determined. Figure 4 shows the first three mode shapes of a substructure system consisting of three wall panels.

During the development of the finite element models, free-vibration tests were conducted on the test structures. The free-vibration tests consisted of the static loading of the test structure at a selected location and then suddenly unloading the structure. The free-vibration response of the structure was observed by an accelerometer transducer array. The pull-tests allowed the direct observation of building substructure natural frequencies. The natural frequencies observed compared well with the natural frequencies computed by the finite element model.

The final effort of the pre-test analysis was to predict the structural response for the acceleration transducer array. The analysis consisted of estimating blast loading on the structure caused by the weapon detonation and using the modal representation of the structure to predict peak structural accelerations at the transducer locations. The blast loading were estimated using an empirical approach which using an initial impulse loading equal to the first three reflections of the blast and a time varying pressure load equal to the pseudo-static confined blast pressure.

WEAPON EFFECTS TESTS

The weapon effects tests conducted on the test structures provided excellent information regarding the general vulnerabilities of the two construction types tested, collapse mechanisms for pre-cast and cast-in-place structures, blast pressure propagation through unprotected facilities, structural response, and interior environment definition. Figure 5 shows the interior detonation of the test munition on the test structure while Figure 6 shows a typical interior pressure time history recorded during the test series. The test data was used extensively in the post-test analysis which is discussed in the next section.

Figure 5: Interior Detonation on Test Structure

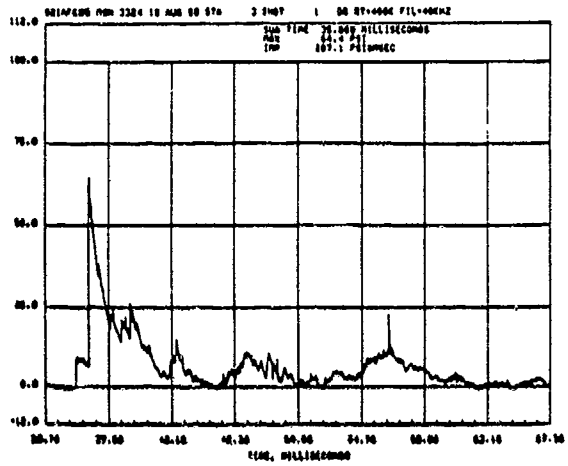

Figure 6: Typical Interior Pressure Time History

POST-TEST ANALYSIS

The post-test analysis centered on the analysis of selected substructure systems and components monitored during the test series with active instrumentation. The finite element modeling described in this section was accomplished using ADINA. The analysis included linear and nonlinear material models as well as the elemination of structural connections and elements during the loading event. The analysis used the pressure loading measured during the test series (Figure 5) and standard time integration methods to predict the response of structural subsystems, components, and connections. Figure 6 shows a typical response of wall panel section subjected to an airblast loading.

For the pre-cast construction, the weak points or failure modes centered on the panel connections and the collapse of the floor panels. For the cast-in-place construction, the predicted failure mode followed the classic shear and flexural failure. Shear failures are localized near the explosive source while flexural failure is more widespread. In the vicinity of the explosive source, the finite element representations in both cases (pre-cast and cast-in-place) quickly exceed the model limitations but the models do approximate when the structural component or connection fails (given the correct failure stresses or forces). Future analytical efforts should focus on ADINA's capability to kill elements and incrementally progress through a collapse event. Reasonable micro- to macro- models could be used to predict and evaluate conventional weapon effects against structures provided that key empirical models are incorporated into the analysis process.

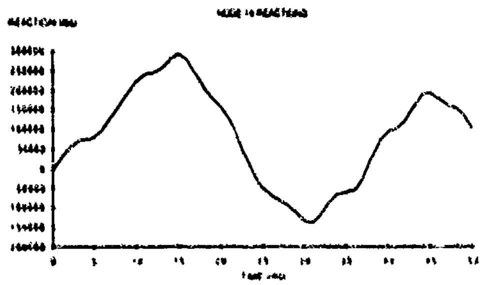

Figure 7: Typical Wall Panel Subsystem Response to Airblast Loading

SUMMARY

The study has highlighted the capabilities and limitations of the finite element approach in modeling weapon effects against structures. The advantages include great flexibility in model characterization, generalized loading functions, nonlinear analysis, stability analysis, and elimination of destroyed elements (ADINA capabilities). The disadvantages center on the lack of available information on the material parameters to use, numerical instabilities, no generalized approach to incorporate empirical models, and the appropriate mix of macro-micro models (reasonable analysis with reasonable cost). For this effort, the finite element results compared favorably with the test data. The modeling exhibited the weak elements of the structural system and provided better pre-test estimates for the instrumentation system. The post-test analysis demonstrated failure modes which were not obvious from the test results. It is clear that an appropriate level of finite element modeling enhances conventional weapon tests against structures particularly in the pre-test stages.

ACKNOWLEDGEMENTS

1
COSMOS is a registered trademark of the Structural Research Corporation.

2
ADINA is a registered trademark of ADINA R&D, Incorporated.

The authors gratefully acknowledge the technical support of Mr. Marty Fertal who conducted the ADINA simulations described in this paper.

DELAYED VENTING OF INTERNAL BLASTS

D. H. Nelson, J. M. Watt, and R. L. Holmes

U. S. Army Engineer Waterways Experiment Station
P.O. Box 631
Vicksburg, Mississippi 39181-0631

ABSTRACT: When calculating internal blast loads for chambers having frangible panels covering vent openings, it may be necessary to consider the effect of the panel connections on the venting initiation time. If the panel connections temporarily resist failure, the onset of venting can be significantly delayed. This delay will result in a greater internal loading than would be calculated if the panel connections failed instantaneously. This paper presents a method, coupled with existing analytical computer codes, that will predict the time at which panel connections fail and the resulting internal blast load.

INTRODUCTION

An internal explosion typically produces a complex load composed of highly transient multiple shock pressures and a relatively long duration gas pressure. In a closed chamber, these pressures can be structurally damaging. Therefore, to help reduce internal pressures, openings are sometimes provided to quickly vent the pressures out of the chamber. Normally, these openings are covered with a frangible panel that offers minimal resistance to blast pressures. The effectiveness of the vent opening in the reduction of internal pressures is dependent on the response of the frangible panel.

Frangible panels are typically lightweight and break away without significantly confining the internal blast. The panel connections are usually designed to fail. Movement of the panel is assumed to begin with the arrival of the initial shock pressure. The panel movement produces a variable vent area that increases from zero to a maximum as the panel moves away from the opening. For the particular case in which the panel is recessed within the vent opening, variable venting does not initiate until the panel has moved the distance of the recess. Tancreto and Helseth (Reference 1) have presented a method for calculating the internal pressure decay when variable venting occurs, including the effect of a recessed panel. In this method, available from the Naval Civil Engineering Laboratory on a microcomputer program called FRANG, the frangible panel is treated as a rigid plate that accelerates under the action of the internal load. Panel connections, which are usually designed to fail quickly, are ignored. FRANG has been shown to produce good estimates of internal blast loads for these conditions.

This paper addresses a condition in which venting is delayed because the frangible panel connections momentarily resist failure. A similar application, not addressed in this paper, is one in which a chamber wall, not specifically designed as a vent area but known to be considerably weaker than the rest of the chamber, may fail as a frangible panel. In both cases, if an estimate of the reaction capacity of the panel or wall can be obtained, then the method presented in this paper would be useful for estimating the internal load. A general outline of the method will be presented first, followed by an illustrated example of the method and comparisons with actual test results.

EFFECT OF DELAYED VENTING ON INTERNAL BLAST LOADS

When panel connections do not fail immediately, venting is delayed. This delay can cause a significant increase in the internal loading by confining the blast and allowing the gas pressure to build up to a higher level before venting is initiated. Note that this is a different type of delay than that caused by a recessed panel as described above. A recessed panel poses no calculational problem for the FRANG code because the panel is still assumed to begin moving under the influence of the initial shock impulse. For the case when panel connections cause the delay, a structural calculation is required to determine the time at which the connections fail and panel movement begins. Calculating the internal load in these cases involves several steps and cannot presently be done using a single computer code. For discussions in this paper, "delayed venting" will be used to identify cases in which panel connections do not fail instantaneously. Also, "time of failure" will be used to refer to the time at which these panel connections do fail.

CALCULATING TIME OF FAILURE AND THE INTERNAL LOAD

A primary point in calculating internal blast loads for delayed venting is to determine the time of connection failure. Once the time of failure is known, the pressure time-history can be easily constructed using existing computer codes. Calculating the time of failure requires consideration of the airblast load function and the flexural resistance of the panel, both of which are functions of time. The internal load is calculated in two segments, one before and one after the panel connection failure. The two segments are then joined together to form the total estimated airblast load funtion.

The method presented employs four computer programs. In addition to the FRANG program mentioned above, the following programs are used: BLASTINW, an internal blast code (Reference 2), SDOF, a single-degree-of-freedom dynamic structural analysis code (Reference 3), and FAILTIME, a code which interfaces with SDOF to calculate the time of panel connection failure (Reference 4).

The method involves five major steps and requires a working knowledge of single degree of freedom equivalent system analytical procedures. A thorough discussion of dynamic structural response and SDOF analysis is found in References 5 and 6. In the steps that follow, no attempt is made to list all of the assumptions and limitations of the four codes used. This information can be obtained by contacting the parties referenced for each code.

STEP 1: CALCULATE INTERNAL LOAD FOR CLOSED CHAMBER

If it is assumed that the pressure time-history prior to the time of failure is identical to the pressure time-history in a closed chamber up to that point in time, then the BLASTINW code can be used to quickly construct the first segment of the load function. The first step is to run BLASTINW for a closed chamber identical to the actual chamber with the exception that venting is not allowed. This calculation produces a pressure time-history, P(t), for a fully contained explosion without any decay associated with venting. At this point, the venting initiation time is unknown.

This closed chamber pressure time-history, P(t), will be used to drive the calculations in Steps 2 and 3 until the time of failure is determined. It is necessary to integrate the closed chamber pressure time-history, P(t), to obtain the impulse time-history, I(t), for use in Step 4. In Step 4 the FRANG code will be used to calculate the decaying gas pressure time-history, Pg(t), resulting from variable venting following the time of failure. Finally, in Step 5 the closed chamber pressure time-history will be truncated at the time of failure, and the decaying segment of the pressure time-history from Step 4 will be appended to construct the final estimated pressure time-history within the chamber.

STEP 2: CALCULATE THE DYNAMIC RESPONSE OF THE PANEL

The panel is analyzed using the SDOF code to determine the panel center displacement time-history, D(t), using as input the closed chamber pressure time-history, P(t), of Step 1; the flexural resistance function of the panel, K(d); and the mass of the panel. The resistance function, K(d), is the variation in panel flexual resistance with displacement. The panel connections are assumed infinitely strong. The SDOF displacement time-history, D(t), is calculated well past the time of expected panel connection failure. This displacement time-history is used in Step 3 to calculate the resistance time-history, R(t), of the panel.

STEP 3: CALCULATE THE TIME AT WHICH PANEL CONNECTIONS FAIL

FAILTIME first constructs a resistance time-history, R(t), using the SDOF displacement time-history, D(t), from Step 2 and the flexural resistance function, K(d), of the panel. Then FAILTIME constructs the dynamic reaction, V(t), by solving

$$V(t) = a[P(t)] + b[R(t)] \quad \text{(Equation 1)}$$

(Reference 6) using the resistance time-history, R(t), and the closed chamber pressure time-history, P(t), from Step 1. In this equation, "a" and "b" are coefficients that vary according to whether the response is elastic or plastic.

Once the dynamic reaction, V(t), is known, the time at which the panel connections fail can be determined. The connections are assumed to fail when the dynamic reaction, V(t), at the ends of the panel exceeds the connection capacity, V(max), of the connections. The connection capacity is the largest dynamic reaction that can be sustained by the panel connections before failure occurs. When one of several modes of failure are possible (for example, bolt failure in shear or tension, anchor pullout, concrete breakout, etc.), the connection capacity is based on the mode of failure requiring the least reaction. The dynamic reaction, V(t), at one end of the panel is calculated in units of force (pounds). The connection capacity, V(max), must also be expressed in units of force. After entering the connection capacity, V(max), FAILTIME checks to see if the connection capacity was exceeded by the dynamic reaction, V(t). By plotting the dynamic reaction, V(t), with the constant connection capacity, V(max), a determination can be made as to when and if the panel connection failed.

FAILTIME is written for simply supported, uniformly loaded, one-way panels. Future revisions of the FAILTIME code will allow treatment of panels having all four sides supported.

STEP 4: VARIABLE VENTING CALCULATION

With an estimate for the time at which the panel connections will fail, the FRANG code can be used to calculate the gas pressure decay, Pg(t), in the chamber as the panel moves away from the opening and venting occurs. To do this the impulse acting on the panel at the time the panel connections fail, I(fail), must be obtained from the closed chamber impulse time-history, I(t), from Step 1. This is the impulse that is used by FRANG to accelerate the panel. (In a standard FRANG calculation, when there is no delay of venting caused by the panel connections, the initial shock impulse is used to accelerate the panel). After additional input, including the equivalent charge weight, the panel weight, and dimensional parameters of the chamber and vent area, FRANG calculates the gas pressure time-history, Pg(t), as it decays to zero.

STEP 5: CONSTRUCTION OF THE TOTAL PRESSURE TIME-HISTORY

As stated earlier, for delayed venting the FRANG calculation represents only that segment of the pressure time-history consisting of the pressure decay following the time of failure. The BLASTINW calculation, P(t), from Step 1, based on a closed chamber, does not include the effects of venting. Therefore, the final step is to truncate the closed chamber pressure time-history, P(t), at the estimated time of failure and then append the FRANG decaying pressure time-history, Pg(t), at this point to construct the final estimate of the total internal blast loading.

COMPARISON OF CALCULATIONS WITH TEST RESULTS

The following example compares calculations from the five-step method of analysis and actual test results. An explosive charge was detonated inside a chamber having a volume of approximately 2,600 cubic feet and one vent area of 120 square feet. The opening was covered with a panel having an approximate weight of 0.20 psi. The panel measured 10 feet high by 12 feet wide and was connected only across the top and bottom edges. The panel was considered to have one-way action in flexure and simple supports. An 18-inch-wide section of the panel was analyzed. This section had an estimated connection capacity, V(max), at each end of 25,200 pounds based on combined shear and tensile stresses in the panel connections. In the following discussion, reference to the "backwall" will identify the chamber wall opposite the vent area.

Calculations were made, following the five steps outlined above. First, using the actual test chamber dimensions, charge data, etc., BLASTINW calculated the average pressure time-history, P(t), on the backwall as if venting had not occurred; that is, for a closed chamber (Figure 1). Using this closed chamber pressure time-history and the structural properties of the panel, SDOF calculated the displacement time-history, D(t), of the panel. The SDOF input and resulting displacement time-history are shown in Figures 2 and 3, respectively. FAILTIME then constructed the resistance time-history, R(t), (Figure 4) using the flexural resistance function, K(d), and the displacement time-history, D(t). With the resistance time-history, R(t), and the closed chamber pressure time-history, P(t), FAILTIME then solved Equation 1 for the dynamic reaction, V(t). In Figure 5, the dynamic reaction, V(t), is compared to the connection capacity, V(max), of the panel. The calculated dynamic reaction builds and eventually exceeds the connection capacity about 48 msec after detonation of the explosive. Since the connection capacity was barely exceeded, a conservative estimate for the time of failure was taken as 55 msec.

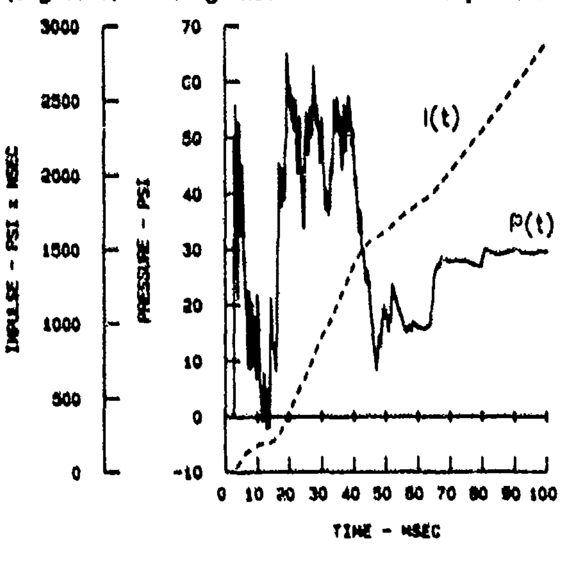

Figure 1. BLASTIN closed chamber pressure time-history

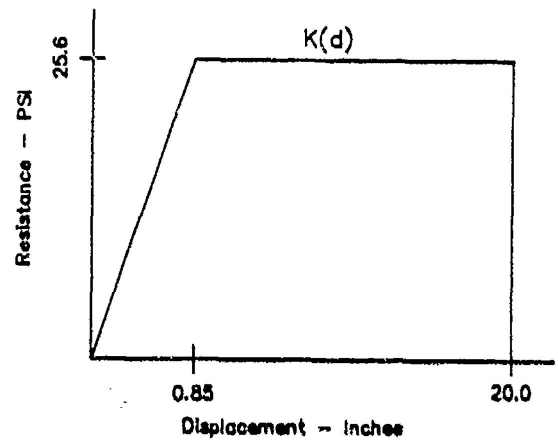

Load Mass Factor = 0.7
Critical Damping Ratio = 0.2
Unload Slope = 30.19 psi/inch
Unit mass = 0.000512 lb·sec^2/inch^3

Figure 2. Resistance function and SDOF input

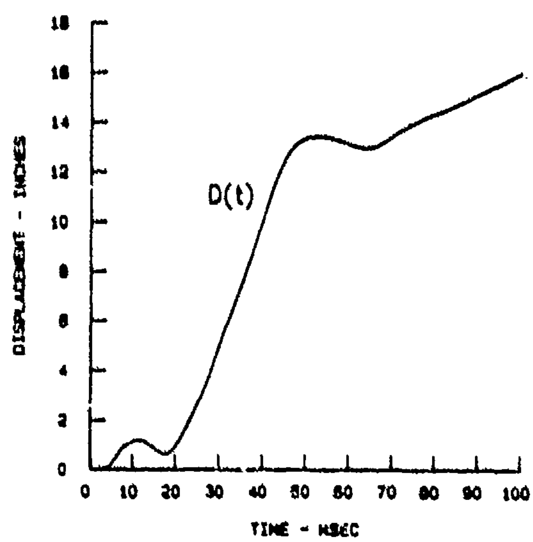

Figure 3. SDOF displacement time-history

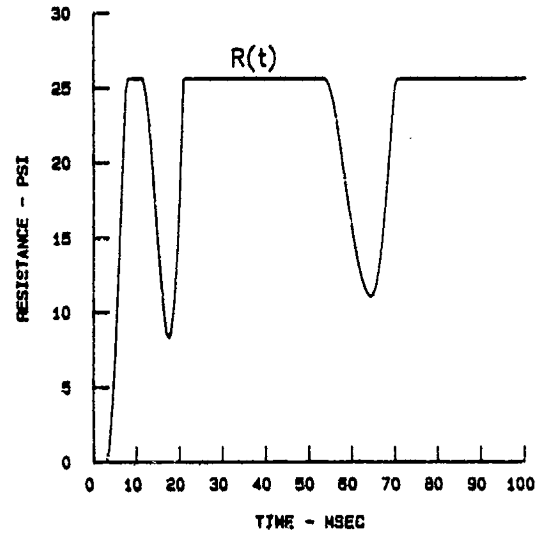

Figure 4. FAILTIME resistance time-history

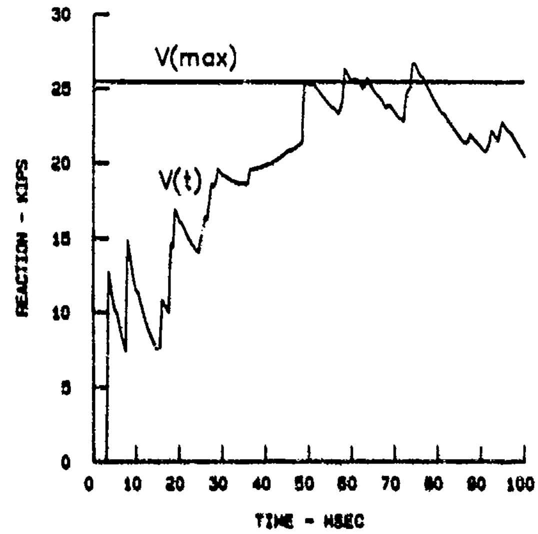

Figure 5. Comparison of FAILTIME dynamic reaction with estimated reaction capacity

The impulse at the time of failure, I(fail), equal to 1,750 psi-msec, was estimated from the closed chamber impulse time-history, I(t), in Figure 1. This impulse and other panel and charge data were entered into FRANG to calculate the decay of the gas pressure, Pg(t), in the chamber after the time of failure. This segment of the pressure time-history is shown in Figure 6. Finally, the closed chamber pressure time-history, P(t), was truncated at the estimated time of failure, and the gas pressure time-history decay, Pg(t), was appended (Figure 7) to obtain the final estimate of the total internal loading.

A typical recorded pressure and impulse time-history on the backwall from the actual test is shown in Figure 8. The gas pressure rise within the chamber is clearly discernable as a long duration swell between 15 and 100 msec on which the highly transient shock pressures are superimposed. Figure 9 is a comparison of the calculated and measured average impulse time-histories on the backwall. The calculated and measured maximum impulses compare well. The calculated maximum impulse (2,075 psi-msec) exceeds the measured maximum impulse (1,830 psi-msec) by a factor of only 1.13. It is interesting to note that the difference in the calculated maximum impulse between the delayed (2,075 psi-msec) and instantaneous (750 psi-msec) connection failure is a factor of 2.4. This observation stresses the importance of carefully considering the time of connection failure when calculating internal loads.

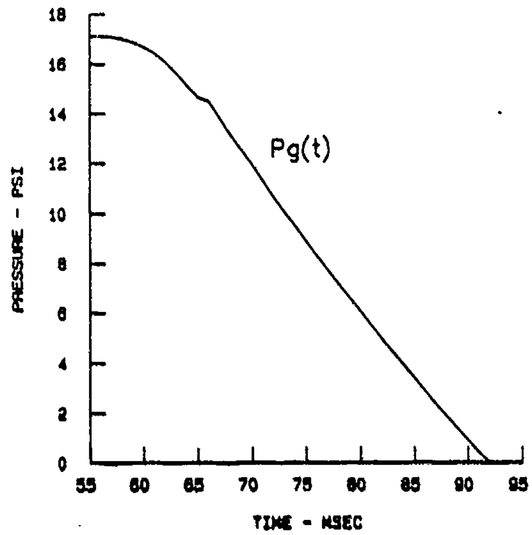

Figure 6. FRANG gas pressure decay time-history

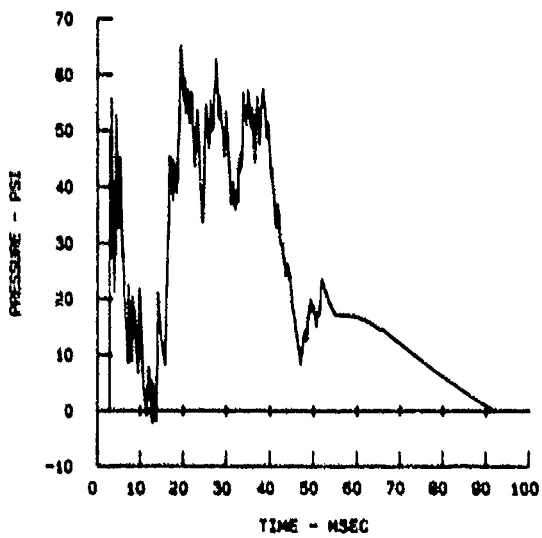

Figure 7. Total estimated pressure time-history

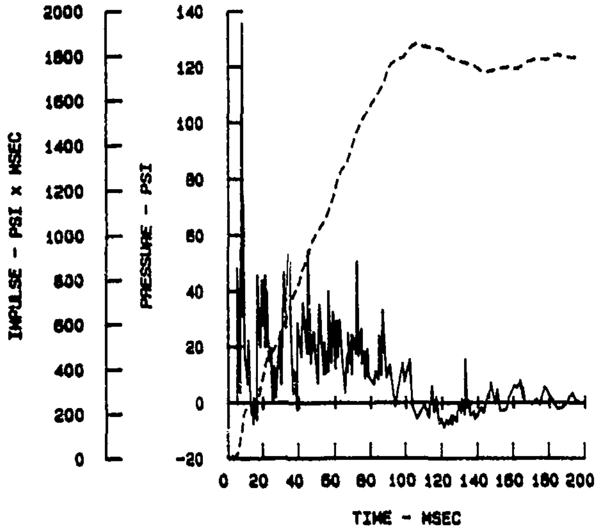

Figure 8. Typical measured pressure and impulse time-history

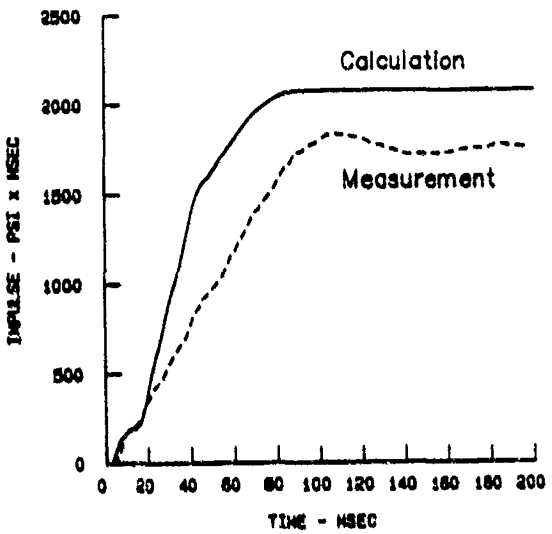

Figure 9. Comparison of average backwall impulse calculation with test data

In addition, high-speed photography shows that panel movement began at approximately 50 msec, which compares well with the calculated 55 msec delay time.

Therefore, the five-step method provided a good estimate of the time of failure and the internal blast loading in the chamber.

Although not presented herein, this method was also used to predict the time of failure and internal load for another test having the same type panel but a lower connection capacity. The method correctly predicted a time of failure of 20 msec. To help put the effect of venting delay in perspective, comparison of the maximum impulse from these two tests reveals an approximate 40 percent increase by delaying the time of failure from 20 to 50 msec.

CONCLUSIONS

With good engineering judgment, the method presented can be used to calculate internal loads for a variety of venting situations not treated before. With a good understanding of dynamic structural analyses and internal blast phenomena, the engineer can produce good approximations for internal loads when the initiation of venting is dependent on the delayed failure time of the panel.

ACKNOWLEDGMENTS

This research was sponsored by the US Department of State, Physical Security Branch, Washington, D.C. under the direction of Mr. Pat Fitzgerald. The technical monitor for the Department of State was Mr. Gerald Meyers. The work was accomplished by the US Army Engineer Waterways Experiment Station (WES), Structures Laboratory, Structural Mechanics Division. Project Manager was Mr. James M. Watt, Jr. (WES). The Project Engineers were Messrs. Donald H. Nelson and Randy L. Holmes. We gratefully acknowledge permission from the Chief of Engineers to publish this paper.

REFERENCES

1. Tancreto, J. E., and Helseth, E. S., "Effect of Frangible Panels on Internal Gas Pressures," Naval Civil Engineering Laboratory, Port Hueneme, California, March 1987.

2. Britt, J. R., Drake, J. L., Cobb, M. B., Mobley, J. P., "BLASTINW User's Manual," Applied Research Associates, Inc., Vicksburg, Mississippi, April 1986.

3. Hyde, D. W., SDOF computer code, US Army Engineer Waterways Experiment Station, Vicksburg, Mississippi.

4. Nelson, D. H., FAILTIME computer code, US Army Engineer Waterways Experiment Station, Vicksburg, Mississippi.

5. "Fundamentals of Protective Design for Conventional Weapons," Technical Manual 5-855-1, Department of the Army, Washington, D.C.

6. Biggs, John M., "Introduction to Structural Dynamics," McGraw-Hill Book Company, New York, 1964.

Backfill Effects on Buried Structure Response

James L. Drake, Robert E. Walker, and Thomas Slawson

Applied Research Associates, Inc.
Southern Division
Vicksburg, MS

ABSTRACT

In this paper, we further investigate the role of Structure Medium Interaction (SMI) on buried structure response. A simple SMI model can be constructed from applying the boundary condition between the soil and structure that requires continuity of both stress and displacement at the soil structure interface. Exploiting these simple boundary conditions, coupled with a simple model of the structural deflection, a set of differential equations that represent the response of a buried structure to explosively produced loading are derived. Limiting cases are developed for flexible, perfectly plastic structures to fully demonstrate the interaction between the incident ground shock loading and the structural deformation. It is shown that deformation is controlled by applied stress and displacement of the soil. For very flexible walls, it is shown that the wall separates from the soil very early in time, and the solution degenerates to the familiar impulsive load response case.

INTRODUCTION

Structure medium interaction (SMI) effects play an important role in the response of buried protective structures when subjected to ground shock loading from conventional weapons. The influence can be profound for highly flexible structures, with the effect diminishing as the structure becomes rigid. Several papers have appeared in the recent literature, for example, Drake, Frank and Rochefort (1), Hinman and Weidlinger (2) and (3), that have incorporated SMI models in the design of buried structures.

While the application of SMI models has only recently been introduced into the design of protective structures, the role of SMI on the response of embedded structures has been recognized for more than a century. For example, Rayleigh (4) studied the radiation field produced by plane sound waves impinging on rigid and gaseous spherical inclusions. The designs of naval structures (i.e., submarines and ships) have used the Taylor plate models and plane wave interaction models since World War II. Perhaps the most widely used formulation is the Doubly Asymptotic Approximation (DAA) developed by Geers (5) that embodies both the high frequency "plane wave approximation" and the low frequency effects where the motion of the structure and fluid are acting inphase.

It was demonstrated by Drake, et al. (1), that a simple SMI model can be constructed from applying the boundary condition between the soil and structure that requires continuity of both stress and displacement at the soil structure interface. Exploiting these simple boundary conditions, coupled with a simple model of the structural deflection, a set of differential equations that represent the response of a buried structure to explosively produced loading were developed. The equations have direct analogy to the familiar single degree-of-freedom (SDOF) system with damping and are easily solved by analytical and numerical means. A comparison of mid-span deflections measured on buried wall explosive tests and computations using this simple model was within ±30 percent of experiments.

In this paper, we further investigate the role of SMI on buried structure response. Limiting cases are developed for flexible, perfectly plastic structures to fully demonstrate the interaction between the incident ground shock loading and the structural deformation. It is shown that, to first order, deformation is controlled by both the incident stress and the displacement of the soil. For very flexible walls, it is shown that the wall separates from the soil very early in time, and the solution degenerates to the familiar impulsive load response case.

PROBLEM DEFINITION

A formulation of the SMI model is given by Drake, et al. (1) by a combination of simple wave propagation theory in the soil and rigid body mechanisms in the structure. Boundary conditions of continuity of both stress and displacement between the soil and structure are imposed for a SMI model. At the interface,

$$\sigma_i = \sigma_{ff} + \sigma_r \qquad (1)$$

where σ_i is the interface stress, σ_{ff} is the incident free-field stress and σ_r is the reflected stress from the structure. Also at the boundary, continuity of displacements requires that

$$V_{ff} - V_r = \dot{u} \tag{2}$$

where V_{ff} is the particle velocity associated with σ_{ff}, V_r is the reflected particle velocity and $\dot{u}$ is the velocity of the structure. The equation of motion for the structural motion is

$$\sigma_i = \rho_s L \ddot{U} + R(u) \tag{3}$$

where ρ_s is the mass density of the structure, L is the structure thickness, and $R(u)$ is the resistance per unit area. For an elastic-perfectly plastic structure

$$R(u) = \begin{cases} Ku & u \leq u_p \\ R_{max} & u > u_p \end{cases} \tag{4}$$

Using the relationship

$$\sigma_r = \rho c V_r \tag{5}$$

where ρ is the mass density and c is the propagation velocity of the soil and incorporating the boundary conditions, Eqs. 1, 2, and 4, results in the expression

$$\rho_s L \ddot{U} + \rho c \dot{U} + R(u) = \sigma_{ff} + \rho c V_{ff} \tag{6}$$

which is the equation of motion for the structure that includes the interaction effect. Strictly speaking, Eq. 5 is for a linear soil, but for real soils, the stress and velocity time histories have different waveforms during unloading. Note that the SMI effect manifests itself as a damping term related to the radiation damping provided by the reflected wave from the structure. Also note that

$$\sigma_{ff_{max}} = \rho c V_{ff_{max}} \tag{7}$$

at shock impingement on the structure. Thus the initial reflection factor is two times the incident stress which arises from the tacit assumption that the structure is moving as a rigid body. As pointed out in Reference 1, substituting a reflection factor based on acoustic wave propagation theory in place of the factor of two will not conserve momentum in this model. Also, the reflection factor produced by this model can be as low as one -- depending on the rise time of the incident stress pulse.

Note that during the early phase of the response when $R(u) \sim 0$, then Eq. 3 is $\sigma_i = \rho_s L \ddot{U}$, showing the interface stress is simply the acceleration of the structure times the mass. However, the stress quickly decays as the structure is rapidly accelerated to the particle velocity of the soil at the interface. The maximum structural velocity occurs when $\ddot{U} = 0$,

$$\dot{U}_{max} = 2 V_{ff} - R/\rho c \tag{8}$$

Thus the maximum velocity that the structure can obtain is twice the free-field particle velocity incident to the structure. It can also be seen from Eq. 3 that the interface stress is reduced to the resistance at the time that the maximum velocity is reached.

The role of the properties of the backfill material can be investigated parametrically by exploring the response of a perfectly plastic system. This solution is easy to obtain and can be used to illustrate the salient features of the SMI problem. Detailed integration of Eq. 3 with complex resistance functions are in good agreement with the simple bounding solutions.

SOLUTIONS FOR PERFECTLY PLASTIC RESPONSE

Consider a perfectly plastic structure with a constant resistance function,

$$R = R_{max}$$

Eq. 6 is easily integrated to give

$$\dot{U}(t) = \frac{1}{\rho_s L} \int_0^t [\sigma_{ff} + \rho c V_{ff} - R_{max}]\, e^{-\eta(t-\tau)}\, d\tau \tag{9}$$

where $\eta = \rho c/m$ and $m = \rho_s L$.

The free-field stress and velocity time histories can be estimated as (for example, see Reference 6)

$$\begin{aligned} \sigma_{ff} &= \rho c V_0 e^{-\alpha t} \\ V_{ff} &= V_0 e^{-\beta t} \end{aligned} \tag{10}$$

where $\alpha = r/c$, $\beta \sim 1/2.5\,\alpha$ and r is the distance to the structure from the explosion. Note that a simpler form of the velocity pulse is assumed here to facilitate the integration. Hence,

$$\frac{\dot{U}}{V_0} = \frac{1}{1-\alpha/\eta}(e^{-\alpha t} - e^{-\eta t}) + \frac{1}{1-\beta/\eta}(e^{-\beta t} - e^{\eta t}) - \frac{R_{max}}{\sigma_{max}}(1 - e^{-\eta t}) \tag{11}$$

where $\sigma_{max} = \rho c V_0$.

<u>Limiting Case $\eta \gg \alpha > \beta$</u>

For most flexible structures, $\eta \gg \alpha > \beta$. That is, the response time of the structure mass is much less than the duration of the free-field stress duration. For this case, as $t > 1/\eta$, $e^{-\eta t} \rightarrow 0$, the wall velocity becomes

$$\frac{\dot{U}}{V_0} = e^{-\alpha \tau} + e^{-\beta t} - \frac{R_{max}}{\sigma_{max}} \tag{12}$$

From this expression it can clearly be seen that the structure velocity simply follows the velocity history of the free-field stress and particle velocity components.

The displacement of the structure can be easily obtained by integrating Eq. 12 as

$$u = \frac{V_0}{\alpha}\left(1-e^{-\alpha t}\right) + \frac{V_0}{\beta}\left(1-e^{-\beta t}\right) - \frac{R_{max}}{\rho c}\, t \qquad (13)$$

Note that the free-field displacement is

$$u_{ff} = \frac{V_0}{\beta}\left(1-e^{-\beta t}\right)$$

and that $\alpha \sim 2.5\beta$, so that the displacement of the structure is following the displacement of the soil, to first order.

Thus for the case of $R_{max}/\rho c \ll V_0$, the maximum displacement of the structure is clearly bounded by

$$u_{max} \le u_{ff}\,(1+\epsilon) \qquad (14)$$

where $\epsilon = \beta/\alpha < 1$. Of course for very resistant structures the displacements fall below this bound, provided that the resistance is sufficient to maintain contact between the soil and structure at the interface.

Drake, et al. (1) demonstrated this by parametric calculations and plotted the results as shown in figure 1 for $\beta = \alpha$. It can be seen that the maximum deflection is proportional to the free-field displacements over a wide range of input conditions. The dashed lines indicate where the structure separates from the soil, as discussed in the next section.

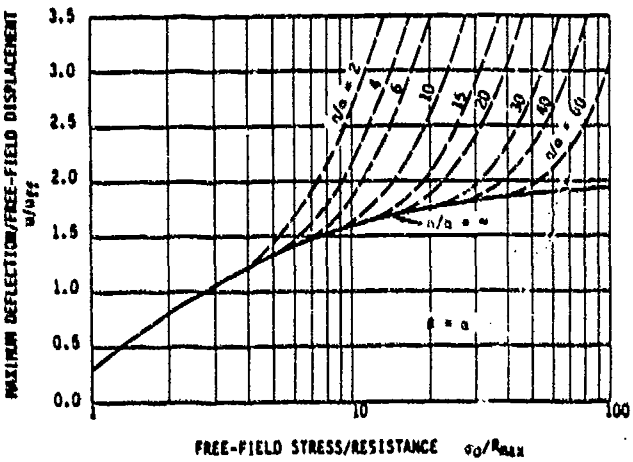

Figure 1. Maximum deflection of a perfectly plastic SDOF with SMI model from Drake, et al. (1).

Thus, we note that the structural response for flexible structures is dominated by the motion of the free-field incident to the structure. To first order, the structure velocity quickly obtains and maintains the particle velocity of the soil. The effect of the structure resistance is to reduce this velocity by a constant amount.

From the free-field ground shock equations, it is noted that at a constant standoff distance,

$$\left.\begin{array}{l} V_0 \approx \text{constant} \\ \sigma_{max} \propto \rho c \\ u_{ff} \propto 1/c \end{array}\right\} \qquad (15)$$

Thus a tradeoff in the design and backfill properties is suggested. High quality backfill materials will exhibit higher c values, resulting in lower free-field displacements, but higher incident stresses. As shown in figure 1, varying the resistance provides only a modest decrease in the peak deflection.

Limiting Case for Cavitation at Interface

For very flexible structures (L/D = 10), the structure mass is very quickly accelerated to velocities approaching twice the free field particle velocity. In these cases, tension can develop at the soil-structure interface, resulting in the structure being spalled or separated from the soil. Rejoining with the soil may occur later in time, depending on the decay characteristics of the incident pulse and the structure resistance. It can be shown from the solutions obtained in Eq. 9-11, that

$$\sigma_i \approx 2\,\sigma_{ff}\, e^{-nt}$$

for very early times. Therefore, from Eq. 3,

$$m\ddot{U} \sim 2\,\rho c V_0 e^{-nt} - R_{max}$$

and

$$\dot{U} \sim 2\,V_0 - R_{max}\, t/m \qquad (16)$$

where $m = \rho_s L$. The peak displacement occurs in this case at a time, $t = 2\,V_0 m/R_{max}$, and gives

$$u_{max} \approx \frac{2m}{R_{max}} V_0^2 \qquad (17)$$

which is the familiar impulse response of plastic systems.

The expression in Eq. 8 can be improved somewhat by using the peak velocity of the wall as given by Eq. 8, and estimating the time of peak velocity as

$$t_{max} \approx \frac{1-R_{max}/2\sigma_{max}}{(\rho c/m + \alpha)} \qquad (18)$$

which gives

$$\frac{\dot{u}_{max}}{V_0} \approx \frac{2-R_{max}/\sigma_{max}}{1 + \alpha m/\rho c} \qquad (19)$$

Thus a better estimate of the peak displacement is

$$u_{max} \approx \frac{1}{2}\frac{mV_0^2}{R_{max}}\left(\frac{2-R_{max}/\sigma_{max}}{1 + \alpha m/\rho c}\right)^2 \qquad (20)$$

Criteria for the cavitation at the interface can be established from Eq. 12. The interface stress can be calculated from Eq. 3 noting that

$$\frac{\dot{u}}{V_0} = -\alpha e^{-\alpha t} - \beta e^{-\beta t}$$

resulting in the expression

$$\sigma_i = R - mV_0\,(\alpha e^{-\alpha t} + \beta e^{-\beta t}) \qquad (21)$$

In order to remain in contact with the soil, $\sigma_i > 0$, which requires

$$\frac{R_{max}}{m} \geq V_0\,\alpha\,(e^{-\alpha t} + \beta/\alpha\; e^{-\beta t}) \qquad (22)$$

For purposes of developing an estimate, note that $\alpha = c/r$ and $\beta \sim \alpha/2.5$ so that

$$\frac{R_{max}}{m} > \frac{V_0 c}{r} \quad \text{or} \quad \frac{R_{max}}{\sigma_{max}} \geq \frac{\rho_s L}{\rho r} \qquad (23)$$

Thus to avoid cavitation and minimize the structure deflection, the ratio of the resistance to the incident stress must be greater than the ratio of mass of the structure to the mass of the soil between the structure and the explosion.

Therefore, in the case of very flexible structures where cavitation is the dominant response mode, the maximum deflection is largely independent of the soil medium, increasing somewhat for high velocity soils as the term $R/\rho c$ becomes small.

COMPARISON WITH TESTS AND CALCULATIONS

A number of buried structure tests were conducted by the U. S. Army Engineer Waterways Experiment Station in support of the U. S. Air Force Engineering and Services Center (7). The tests, as reported by Baylot, used slabs with length to thickness ratios of 5 and 10, and varied the weapon position to sustain different damage levels. Calculated wall deflections using the SMI model described in this paper were shown to be within ±30 percent of the observed deflections (see figure 2). All of the salient features observed in the tests were successfully predicted

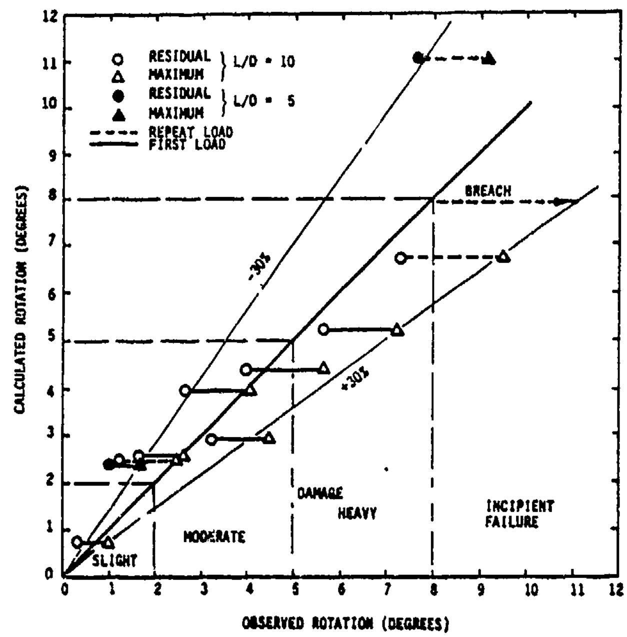

Figure 2. Comparison of calculated and observed rotation for buried wall tests from Drake, et al. (1).

by the theory; namely, (a) the rapid decay of the interface stress following the initial peak, (b) peak interface stress that was only slightly higher than the incident peak stress due to the finite risetime of the input pulse, (c) in some cases, separation (i.e., $\sigma_i = 0$) at the soil structure interface, (d) late time interface stresses that approach the structural resistance, (e) and, most importantly, the deflections were accurately calculated by a simple handbook idealization of the structure.

In these tests, the slabs with length to thickness ratios of 10 were observed to separate from the soil shortly after the shock arrival. Peak rotations at the support calculated by Eq. 20 is shown in figure 3 compared with the observed rotations. It can be seen that the calculations compare favorably with the test results for the charge parallel to the wall. Departure from the theory can be explained on the variation in the weapon effects due to weapon orientation. Lower deformations were observed for weapons orientated in an end-on configuration and larger for a vertical orientation.

Another case that of cavitation dominating the structural response is clearly shown by a parametric study by Weidlinger and Hinman (3). Their

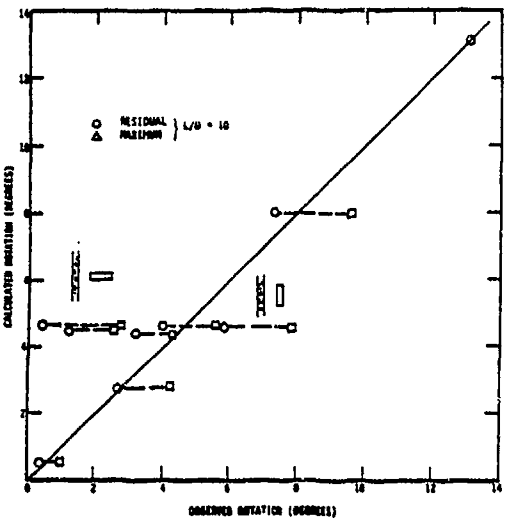

Figure 3. Comparison of calculated and observed rotation of buried wall tests using equation 20.

example is that of a 53-inch-thick slab with a span of 42 feet and resistance of $R_{max} = 45$ psi subjected to a partially coupled (f=0.4) weapon at the ground surface. The weapon yield was 1014 lbs of TNT, while the backfill soil was sand, with a $\rho c = 22$ psi/fps, $c = 1000$ fps and $n = 2.75$. For the problem considered the incident stress was about 185 psi, which resulted in a maximum computed displacement of 2.9 inches.

Using Eq. 20, we obtain $u_{max} = 2.4$ in. which agrees well with the more exact solution.

Both SDOF and finite element (FE) model solutions were developed in Reference 3 for this structure in several soil types, as shown in figure 4. From the bounds developed in Eq. 23,

$$\frac{R_{max}}{\sigma_{max}} > 0.315$$

in order to prevent the slab from separating from the soil. In the baseline case, $R_{max}/\sigma_{max} = 45/185 = 0.24$, so this clearly fails the test. As the soil is varied, the maximum particle velocity at a given range is nearly constant while the maximum stress increases proportional to ρc. Therefore for soils with $c > 750$ fps, the incident stress can always cause cavitation, and the bounding solution should provide good results.

Peak displacements estimated from Eq. 20 are also shown in comparison to the SDOF and FE computations in figure 2. Since we are not certain about the details of how the material was modeled in (3) for the variation in c, we provide two curves, one for $n = 2.75$ and $n = 2.5$, which bound the computations. The simple, impulse load estimate is very close to the FE calculation for the $n = 2.75$ curve up to $c = 3000$ fps. For higher values of c, it appears that the attenuation coefficient was varied to a value of $n = 2.5$ at $c = 5000$ fps.

SUMMARY

A SMI model is proposed that accurately models the interface condition between a structure and soil. During the loading phase, continuity of both stress and displacement between the soil and structure was maintained. Resulting equations of motion for this system resemble those of a SDOF system with damping. However, the damping term is the result of satisfying the stated boundary conditions and is not related in any way to viscous or frictional damping effects.

It was shown that interface stress is highly dependent upon the inertial effects and the deflection of the structural section. For many important cases, the interface stress approaches zero within twenty-five transit times through the structural section and then slowly approaches the resistance at late time. It was shown that the maximum structural velocity cannot exceed twice the incident free-field particle velocity even for very low resistance structures. In contrast, current design methods which apply the free-field stresses directly as the interface stress violate the basic displacement boundary condition and cause the structure element to be accelerated to velocities far greater than physically possible.

A comparison of theoretical results with buried wall experiments is excellent. Calculated wall deflections were within ±30 percent of those observed in tests. Interface stresses were accurately predicted as well. The theory is easily solved for any structure and incident loading by analytical methods or numerically on desktop or programmable calculators.

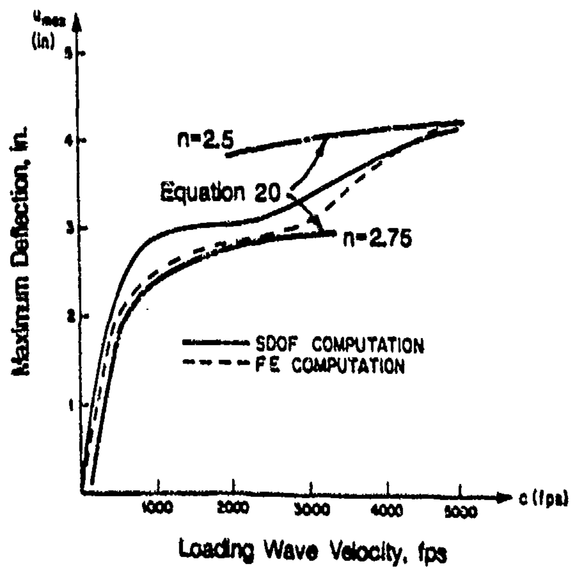

Figure 4. Maximum deflection computed by Eq. 20 compared with SDOF and FE analysis of a buried wall, from Weidlinger and Hinman (3).

REFERENCES

1. Drake, J. L., Frank, R. A., and Rochefort, M. A., "A Simplified Method for the Prediction of the Ground Shock Loads on Buried Structures," Proceedings of the International Symposium on the Interaction of Conventional Weapons with Structures, Mannheim West Germany, March 9-13, 1987, Federal Minister of Defense, 5300 Bonn 1.

2. Hinman, E. E. and Weidlinger, P., "Single Degree of Freedom Solution Structure-Medium Interaction," Proceedings of the International Symposium on the Interaction of Conventional Weapons with Structures, Mannheim West Germany, March 9-13, 1987, Federal Minister of Defense, 5300 Bonn 1.

3. Weidlinger, P. and Hinman, E. E., "Analysis of Underground Protective Structures," Journal of Structural Engineering, Vol. 114, No. 7, July 1988.

4. Rayleigh, J. W. S., The Theory of Sound, Dover Publications, New York, 1945.

5. Geers, T. L., "Doubly Asymptotic Approximations for Transient Motions of Submerged Structures," J. Acoust. Soc. Am., Vol. 64, pp. 1500-1508, November 1978.

6. Drake, J. L. and Little, C. D., Ground Shock from Penetrating Conventional Weapons, Presented at the Interaction of Non-Nuclear Munitions with Structures, U. S. Air Force Academy, Colorado, May 1983.

7. Baylot, J. T., Kiger, S. A., Marchand, K. A., and Painter, J. T., Response of Buried Structures to Earth-Penetrating Conventional Weapons, ESL-TR-85-09, Engineering & Services Laboratory, Air Force Engineering & Services Center, Tyndall AFB, FL, November 1985.

THE FOURTH INTERNATIONAL SYMPOSIUM
ON
INTERACTION OF NON-NUCLEAR MUNITIONS WITH STRUCTURES
PANAMA CITY BEACH, FLORIDA

17-21 April 1989

BACKFILL EFFECTS ON STRUCTURAL RESPONSE

by

S. A. Kiger, F. D. Dallriva, and P. G. Hayes
U.S. Army Engineer Waterways Experiment Station
Vicksburg, Mississippi

ABSTRACT:

Soil-Structure Interaction is an important consideration in calculating the response of buried structures to blast effects. Results from the Shallow-Buried Structures (SBS) research program, which is sponsored by the Defense Nuclear Agency, have shown that typical buried command and control type structures can survive as much as tenfold greater peak overpressure from a nuclear weapon than was thought possible. The unexpected hardness of the buried structures resulted primarily because the effects of soil-structure interaction had been underestimated. Data from the SBS research have resulted in significant revisions in vulnerability computational methods and in our estimates of buried structure vulnerability to nuclear weapons.

In attempts to extrapolate the analytical methods developed in the SBS research program to compute buried structural response to conventional weapons, there is a great deal of uncertainty becauee of the localized loading and response from conventional weapons. For example, the curves shown in Figure 1* indicate about the same predicted structural response in a backfill with low seismic velocity (about 1,000 fps), but show a considerable difference in predicted structural response at higher seismic velocities. There are many structures in backfills with higher seismic velocities, especially in Europe. Also, if backfill type does not affect structural

* From Hinman, Eve E., and Weidlinger, P. Proceeding from International Symposium on Interaction of Non-Nuclear Munitions with Structures, Mannheim, West Germany, 1987.

response, a considerable cost savings could be realized in future construction projects by not requiring a select backfill.

Unfortunately, there are very little data from conventional weapon tests on buried structures in backfill materials with seismic velocities outside the range of about 800 to 1,500 fps. The differences indicated by the curves in Figure 1 have recently assumed a greater importance, since the analytical methods from the Army Technical Manual 5-855-1 predict increasing structural response with increasing seismic velocity, and analytical methods in a new draft Air Force design manual predict structural response to be very nearly independent of seismic velocity.

This paper will review the applicable theory, evaluate the analytical methods depicted by the curves in Figure 1, and compare predictions using these methods with the limited data base available.

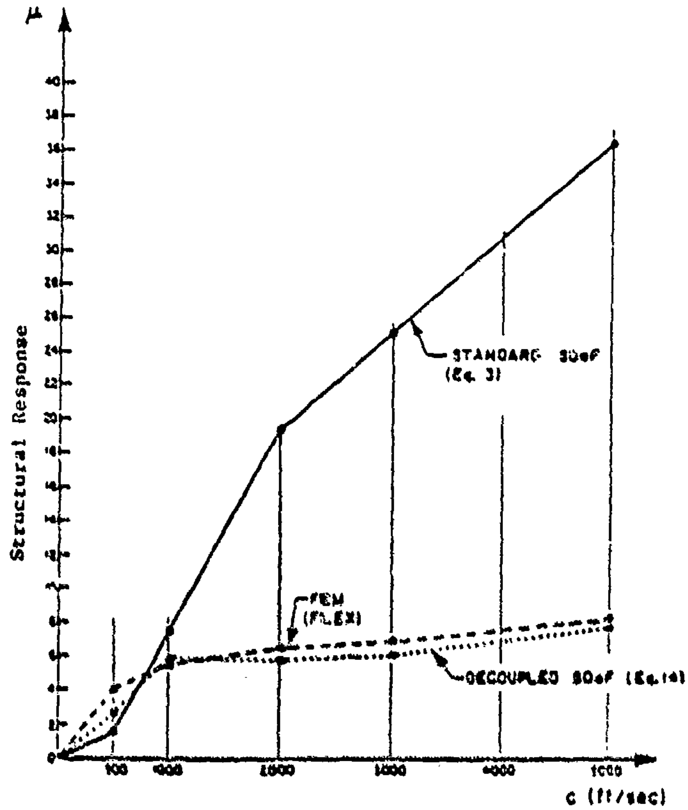

Figure 1. Structural response versus seismic velocity of backfill. (From Hinman, Eve E., and Weidlinger, P.)

REINFORCED AND PRECAST CONNECTIONS UNDER CLOSE-IN EXPLOSIONS

T. Krauthammer and M. DeSutter

Department of Civil and Mineral Engineering
University of Minnesota, U.S.A.

Abstract

The response of reinforced and precast connections under the application of close-in detonation effects has been studied. Typical connection details were analyzed by the finite element methods, and their performance under severe short-duration localized loads was evaluated. Observed deficiencies in the behavior were examined, and subsequent design modifications were shown to correct the response. The procedure for evaluating several knee- and tee-joints is presented and discussed. Recommendations are provided for the design of such connections.

Introduction

Usually, connections are assumed to be rigid systems which allows the adjoining elements to develop their full potential. However, if the connections are not designed adequately that will not be the case, and the structures will fail prematurely. Examples of this type of behavior are many as discussed in (Krauthammer, 1987), where it was shown that floor-arch joints exhibited major damage. Despite the fact that these structures were tested under a simulated nuclear environment, similar modes of behavior could exist under localized detonations. Recent studies on the modeling of concrete behavior under high rate load effects at the University of Minnesota have made it possible to accurately analyze connections subjected to this type of loading.

Load Definition

The magnitude and time pulse history of the blast load were determined through interpolation of data shown in Coltharp, et. al.(1985). A 20" wide strip was superimposed on the proposed pressure grid at the worst case location. The pressure was then converted to a concentrated load which will act on the end of a cantilever beam. The resultant peak load was set at 2451 kips. Based on the same report, the rise time to first peak was set at 0.04 msec. The duration of positive pressure was set at 0.53 msec.

Connection Models

Ten connection details were analyzed for their structural integrity under blast loading.

The analysis was completed with a finite element code SAMSON 2 written by Schreyer, et. al.(1984). This code utilizes a constiuative concrete damage model written by Stevens and Krauthammer (1988) at the University of Minnesota. In the compression domain the model utilizes a combination of plasticity and contiuum damage mechanics theories with a nonlocal definition of a scaler damage variable to model strain softening. In tensile regions a nonassociated flow rule with associated modification is used. This procedure will accurately predict strength states for tension and shear while holding dilational strains to a minimum and eliminating the possibility of spontaneous energy generation. The concrete was modeled with a mesh composed of quadratic 8 node rectangular and 6 node triangular elements. The mesh element size was refined until a change in stress of 5% or less was observed between adjacent elements. This mesh was then compared to a further refined mesh with a stress deviation of 5% or less recorded at identical points. The steel reinforcement was modeled using bar elements connected to the midline nodes of the concrete elements.

The adequacy of this procedure was checked by modeling reinforced concrete beams and comparing the results to those measured experimentally by Feldman and Siess (1958).

BEAM

MAX. DISPLACEMENT

(exper) (samson2) C-1

3.0" 3.2" H-1

8.4" 7.2" These results are very good considering the high degree of nonlinearity and erratic impulsive loading.

The approach used to model beam/column connection behavior is similar to that used by Nilsson (1973). The column is rigidly attached at its base (mid-height between stories) and the beam is cantilevered approximately one third of a typical span length. This method was chosen in order to predict a worst case scenario (i.e. beam/slab discontinuity due to openings or localized failure). A concentrated blast load similar to that outlined above was then applied to the end of the cantilever. The details represent a beam/column configuration. However, the actual simulation models a wall/slab structure by analyzing a slice through the section subjected to worst case loadings. This approach does not consider 3-dimensional load distribution in the slab for two reasons. The blast load under consideration is somewhat uniform over the width of the structure and the susceptibility to repeated loading is likely.

Three different connection types with varying details were chosen by their performance in previous research. These connections were then tested by the procedure outlined above for their structural integrity. Minor alterations in overall dimensions, area and location of steel reinforcing, and material properties were made until safe and efficient behavior was observed.

The parameters used to determine adequate connection behavior are as follows. Deflections should not exceed those specified in the ACI Building Code (318-83). Direct shear should not surpass the Hawkins shear limit as shown in Murtha and Holland (1982). Flexural shear and compressive stress in the concrete should not exceed ACI specified limits. Reinforcement stresses should not exceed 1/3 yield in the connection region and 2/3 yield at the hinge location. The location of the hinge should occur at a distance d from the face of the joint. Following these criteria will ensure adequate behavior under repetitive blast loadings.

Below is a brief summary of each connection and it's reinforcement details. All connections represent a slice (or thickness) of 20", reinforcement yield strength of 60 ksi, and concrete strength of 6 ksi as shown in Figure 1.

Monolithic Knee Joint

Five different geometries with varying reinforcement were tested.

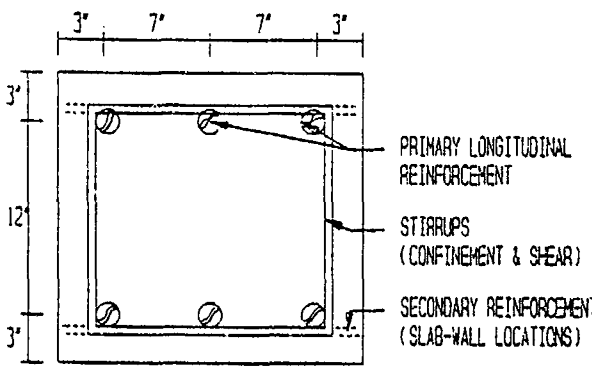

TYPICAL BEAM/COLUMN CROSS-SECTION

Figure 1 (SLAB-WALL)

The first connection (BL-1A, Figure 2) incorporates an 18" wide by 20" thick column and beam detail. The beam and column are reinforced with 1% steel (3 - #9 bars, fy = 60 ksi) on each face. Diagonal steel (2 - #8 bars) is placed on the inside corner of the beam-column interface at a 45 degree angle with 2" of cover. The #9 main flexural bars are anchored in the joint with standard 90 degree hooks. Transverse stirrups are tied around the #8 diagonal bars and the outer face flexural bars. The stirrups provide confinement for the joint core, compression resistance for the outside flexural bars, crack control at the interior of the joint, and buckling resistance for the diagonal steel under a closing moment. The size and spacing of the stirrups can be determined by the procedure proposed by Park and Paulay (1975).

The second connection (BSL2A, Figure 3) incorporates a 12" wide by 20" thick column and beam detail. The beam and column are reinforced with 1.5% steel (3 - #9 bars, fy = 60 ksi) on each face. Diagonal steel (3 - #8 bars) is placed 2" from the exterior face of an 8" diagonal concrete strut located on the inside corner of the beam-column interface. The #9 main flexural bars are anchored in the joint with standard 90 degree hooks. Transverse stirrups are tied around the #8 diagonal bars and the outer face flexural bars.

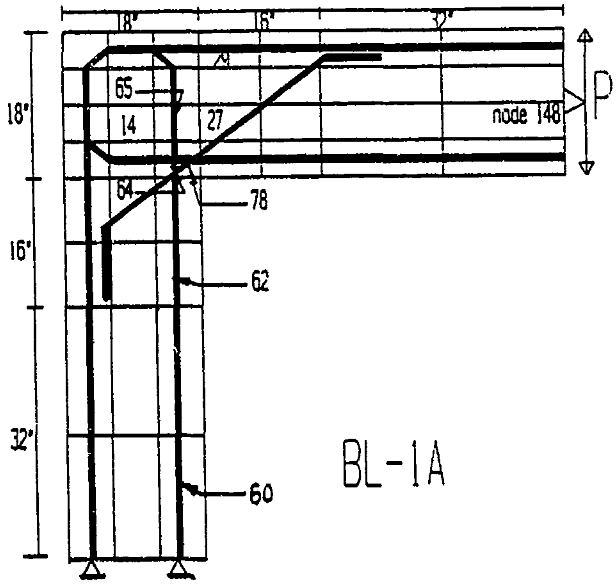

Figure 2 Connection BL-1A

The third connection (BL-6A, Figure 3) incorporates an 18" wide by 20" thick column and beam detail. The beam and column are reinforced with 0.6% steel (3 - #7 bars, fy = 60 ksi) on each face. Diagonal steel (2 - #6 bars) is placed 2" from the exterior face of an 8" diagonal concrete strut located on the inside corner of the beam-column interface. The #7 main flexural bars are anchored in the joint with standard 90 degree hooks. Transverse stirrups are tied around the #6 diagonal bars and the outer face flexural bars.

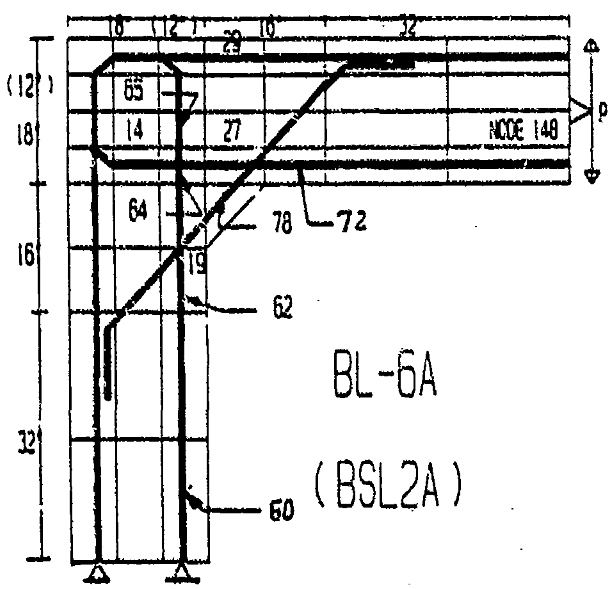

Figure 3 Connections BSL2A and BL-6A

The fourth connection (BL-6C) is identical to BL-6A with one exception. The diagonal bar steel is increased to 3-#7s which is equal to the amount of steel used for the main flexural bars.

The fifth connection (BLS6A) incorporates an 18" wide by 20" thick column and beam detail with sifcon material added in the connection region as shown in Figure 4. The material properties used for sifcon with 12% by volume deformed steel wires are as follows: modulus of elasticity 1200 ksi; compressive strength 12 ksi; and a tensile strength of 1.8 ksi (Homrich and Naaman, 1988). The geometry and reinforcement used in this detail are identical to the BL-6A connection.

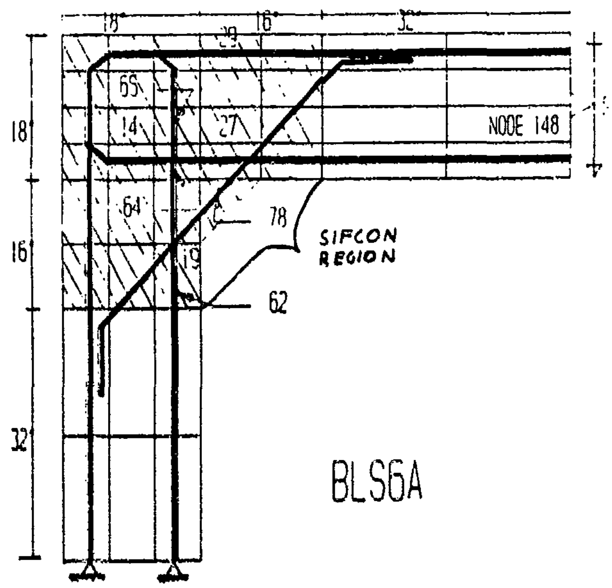

Figure 4 Connection BLS6A

Precast Knee Joint

Two types of precast details were tested. The first detail (PL-1D, Figure 5) incorporates an 18" by 20" thick beam and column. The beam is placed on a corbel which protrudes 6" from the face of the column. A 1/2" cotton duck pad is placed between the bottom of the beam and the top of the corbel. A second pad is placed between the end of the beam and the face of the column. The beam is then postensioned to the column with four #9 threaded rebar as shown in Figure 6. The #9 bars are placed in 3' long sleeves in the beam and threaded into lenton couplers located in the column. These bars are then stressed to 33 ksi which will compress the pad and insure a uniform seal. This detail (Figure 6) exhibited the best performance in a test of seven different precast connections subjected to severe dynamic loading (Jayashankar, 1987). In addition a continuous steel angle with a 3/8" diagonal strut located at 20" on center is welded to the face of the corbel and the bottom of the beam. The design of the corbel should follow standard practice as set fourth by the PCI Design Handbook (1985).

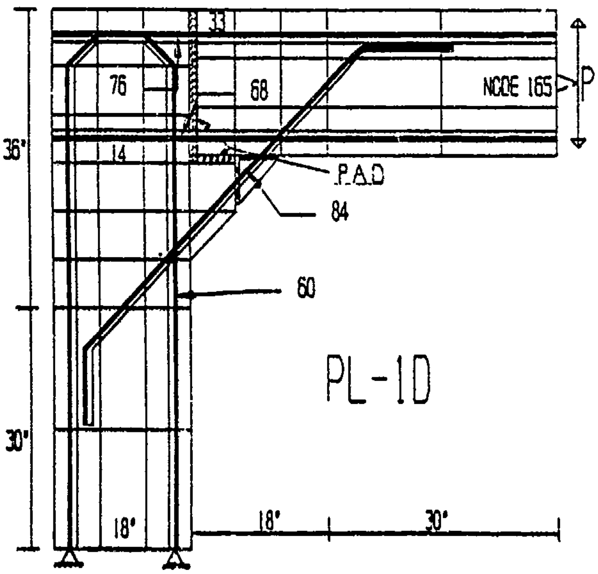

Figure 5 Connection PL-1D

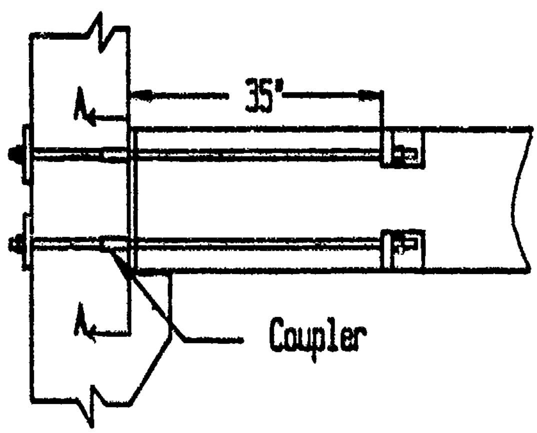

Figure 6 Postensioning Approach

The second detail (PL-2S, Figure 7) incorporates an 18" by 20" thick beam and column. The beam is placed on a corbel which protrudes 6" from the face of the column. A 1/2" cotton duck pad is placed between the bottom of the beam and the top of the corbel. A 4" gap between the end of the beam and the face of the column will be grouted solid. The beam is then postensioned to the column with four #9 threaded rebar similar to detail PL-1D.

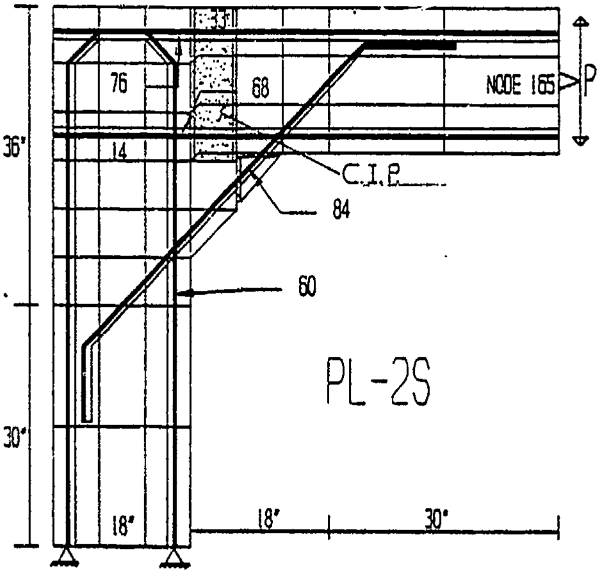

Figure 7 Connection PL-2S

Monolithic Tee Joint

Two types of tee joint details were tested. The first detail (BT-6A, Figure 8) incorporates an 18" wide by 20" thick column and beam. The beam and column are reinforced with 0.6% steel (3 - #7 bars, fy = 60 ksi) on each face. Diagonal steel (2 - #6 bars) is placed 2" from the exterior face of a 4.5" diagonal concrete strut located on the inside corner of the beam-column interface. The #7 flexural bars extending from the beam are anchored in the joint with standard 90 degree hooks. The column reinforcement is continuous through the joint.

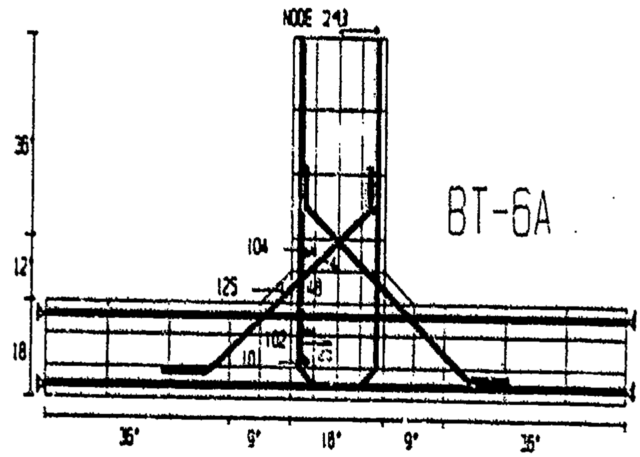

Figure 8 Connection BT-6A

The second detail (BT-8A, Figure 9) incorporates the same beam and column dimensions with identical steel reinforcement as for BT-6A. However, the diagonal strut is increased to 9" and the diagonal steel located 2" from the face of the strut is increased to 3-#7 bars.

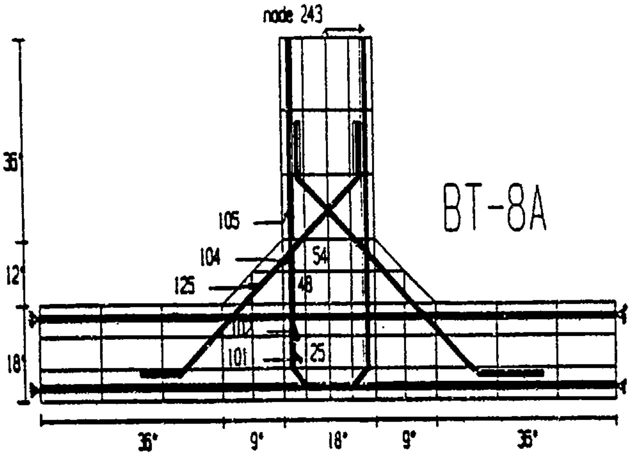

Figure 9 Connection BT-8A

RESULTS AND DISCUSSION

A summary of results for the five monolithic knee joint connection details are shown in Table 1. Peak deflections and stresses are shown for concrete and steel elements at critical locations in the detail. These values are compared to the allowable and a determination is made on the reliability of the detail.

Table 1 Monolithic Knee Joints

ELEMENT #	STRESS psi	ALLOW. stress	BSL2A	BL-1A	BL-6A	BL-6C	BLS6A
node 148	y-disp in.	0.5	1.03	0.63	0.57	0.56	0.48
19	Y-stra	5	0.61	0.28	0.42	0.42	0.18
28	X	-2700	-3600	-2400	-2400	-2300	-1400
14	shear	-608	-1100	-470	-480	-500	-480
27	shear	-608 610	-690 380	-460 410	-480 302	-480 301	-390 210
60	bar		65000	49000	52000	52000	65000
62	bar	43330	52000	32000	43000	43000	24000
63	bar	43330	46000	36000	32000	35000	17000
64	bar	21650	26000	31000	16000	16000	10000
66	bar	21650	19000	21000	7500	5100	6100
78	bar	43330	46000	46000	43000	30000	26000

The detail with a 12" beam and column (BSL2A) shows values of deflections and stresses which exceed the allowable in all respects. The size of the members in this detail are not sufficient to resist the design load. Detail BL-1A required a large amount of steel to obtain acceptable deflections and large bar stresses were recorded at the center of the connection (element #64). For these reasons a diagonal strut such as shown in details (BL-6A), (BL-6C), and (BLS6A) should be added. Detail BL-6A satisfied all the above criteria with a relatively low amount of steel reinforcement (0.6%). Increasing the amount of diagonal steel from half of the main flexural steel has little effect on the connections performance (see detail BL-6C). The connection which performed the best out of the five, incorporated "Sifcon" material in the joint region. Both deflections and bar stresses in the joint region decreased dramatically.

A summary of the precast knee joint connection behavior is shown in Table 2. Detail PL-1D transfers all compressive loads through a flexible, reinforced fiber pad. Deflections are maintained at an acceptable value, however compressive stress in the top reinforcement is well into yield which may cause buckling. The stress in the tensile reinforcement does not reach yield, however the stress is 20% higher than allowable. Reducing the amount of prestress to 10 ksi should alleviate this problem.

Table 2 Precast Knee Joints

ELEMENT #	STRESS psi	ALLOW.	PL-1D	PL-2S	PL-4S
node 166	Y-disp in.	0.5	0.53	0.45	0.47
14	shear	-620	-506	-424	-365
33	X	-2700	-1550	-2060	-1460
60	bar	43000	41000	42600	44100
68	bar	21600	66000	36000	23000
70	bar	43000	53000	63000	57000
71	bar	43330	59000	62000	49000
76	bar	21600	65000	27000	10000
84	bar	27000	26000	63000	68000

Details PL-2S and PL-4S are grouted in place with a 6000 psi concrete. Compressive stress in the top reinforcement is well within allowable. Tensile stress in the bottom bars is very near yield. Reducing the amount of prestress in (PL-4S) to 10 ksi has lowered the stress to near acceptable values. Stiffening the compressive region of this connection with grout has greatly increased the tension on the continuous angle assembly located at the corbel. The spacing of the stiffeners on this assembly should be decreased to 10" on center.

The results for the monolithic tee joint are shown in Table 3. Detail BT-6A uses a 4 1/2" diagonal strut. The tensile reinforcement in the beam is stressed well into the yield range. Therefore we increased the strut size to 9" and the area of the diagonal steel to (0.6%) in detail BT-8A. This reduced the tensile stresses in the joint region and relocated the hinge to an acceptable distance from the joint interface. Both details have shown high flexural shear stresses at the interface and interior of the joint. This is due to a stiff column flexible beam configuration. Correct design of shear stirrups at these regions of concentrated moment and shear is a necessity. The reinforcement in the column was subject to very light stress (20 ksi max.).

Table 3 Monolithic Tee Joints

ELEMENT #	STRESS psi	ALLOW.	BT-6A	BT-6A
node 243	X-disp in.	0.5	0.33	0.29
25	shear	-620	-650	-640
54	shear	-620	-490	-520
46	Y-strain	%	0.33	0.33
101	bar	21600	10000	2300
102	bar	21600	35000	19000
103	bar	43330	65000	52000
104	bar	43330	65000	63000
126	bar	43300	65000	61000

REFERENCES

"Building Code Requirements for Reinforced Concrete (ACI 318-83)," American Concrete Institute, Detroit, Michigan, 1983, 111 p.

Coltharp, D.R., Vitayaudom, K.P., and Kiger, S.A., "Semihardened Facility Design Criteria Improvement", report ESL-TR-85-32, U.S. Army Waterways Experiment Station, Sep. 1985.

Cook, W., and Mitchell, D., "Disturbed Regions in Reinforced Concrete", ACI Structural Journal, Mar.- Apr. 1988, pp. 206-216.

Feldman, A., and Siess, C.P., "Investigation of Resistance and Behavior of Reinforced Concrete Members Subjected to Dynamic Loading, Part II," Structural Research Series No. 165, University of Illinois, Sep. 1958.

Hawkins, N.M., Lin, I., and Ueda, T., "Anchorage of Reinforcing bars for Seismic Forces", ACI Structural Journal, Sep.- Oct. 1987, pp. 407-418.

Homrich, J.R., Naaman, A.E., "Stress-Strain Properties of Sifcon in Uniaxial Compression and Tension", report AFWL-TR-87-115, University of Michigan, Aug. 1988.

Jayashankar, V., "An Interior Moment Resistant Precast Connection", M.S. Thesis, University of Minnesota, 10/1987.

Krauthammer, T., "Reinforced Concrete Arches Under Blast and Shock Environments", The Shock and Vibration Bulletin, NO. 57, part 4, January 1987, pp. 19-27.

Krauthammer, T., and Stevens, D.J., "Development of an Advanced Computational Approach for the Analysis of Buried Reinforced Concrete Structures Subject to Severe Stress Transients", Structural Engineering Report ST-88-05, Department of Civil and Mineral Engineering, University of Minnesota, Sep. 1988.

Leon, R., "Performance of Interior Joints with Variable Anchorage Lengths", ACI Structural Journal, (to appear).

Leon, R., "Shear Strength and Hysteretic Behavior of Interior Beam - Column Joints", ACI Structural Journal, (to appear).

Murtha, R.N., and Holland, T.J., "Analysis of WES FY82 Dynamic Shear Test Structures," Naval Civil Engineering Laboratory, Technical Memorandum No. 51-83-02,, Dec., 1982.

Nilsson, I.H.E., "Reinforced Concrete Corners and Joints Subjected to Bending Moment", National Swedish Building Research, Document D7, 1973.

Park, R., and Paulay, T., "Reinforced Concrete Structures", Wiley ,1975.

"PCI Design Handbook, Third Edition," Prestressed Concrete Institute, Chicago, Illinois, 1985.

"Recommendations for Design of Beam-Column Joints in Monolithic Reinforced Concrete Structures," reported by ACI-ASCE Committee 352, ACI Journal, May-June 1985, No. 2, V. 82, pp. 266-284.

Schreyer, H.L., Richards, C.G., Bean, J.E., and Durka, G.R., "SAMSON2 Users Manual", Air Force Weapons Laboraty, AFWL-TN-82-18, September 1982 (Revised June 1984).

Soroushian, et al., "Pullout behavior of Hocked Bars in Exterior Beam - Column Connections" ACI Structural Journal, May - June 1988, pp. 269-276.

A NONLOCAL CONTINUUM-DAMAGE PLASTICITY APPROACH FOR RC BEAMS SUBJECTED TO LOCAL IMPULSE

David J. Stevens
Asst. Prof. of Civil Engrg.
Clarkson University
Potsdam, NY 13676

Theodor Krauthammer
Assoc. Prof. of Civil Engrg.
University of Minnesota
Minneapolis, MN 55455

ABSTRACT: In this paper, a rate-independent constitutive model for plain concrete is proposed for application to the analysis of impulse loaded structural members. The model combines a continuum damage approach, using a scalar damage variable, with a pressure sensitive plasticity model. The plasticity model incorporates a nonassociated flow rule in regions of low compressive or tensile hydrostatic pressures and an associated flow rule. The concrete model is combined with a uniaxial steel model and a layered, large strain, Timoshenko beam element to perform the analysis of impulse loaded, simply supported, reinforced concrete beams.

INTRODUCTION AND BACKGROUND

The analysis of the response of impulse and blast loaded structures, buried and above ground, has received a continuous but varying level of attention over the past 40 years. Due to the almost infinite number of permutations of a given structure's parameters (i.e, geometry, material properties, depth of burial, etc.) and anticipated threats, and, due to the costs of performing full- and small-scale tests on such structures, the amount of available experimental data, while broad, is also scant relative to any particular combination of structure and impulse load. Thus, the development of analytical/computational tools are required in order to: 1) understand the complex nonlinear behavior of the structure (and soil, if buried), 2) perform parametric studies, and 3) develop design guidelines.

One analytical tool is the Finite Element Method, which has been applied with great success to geometrically and materially nonlinear continuum and structural problems. The geometric nonlinearities can be modelled with the well known kinematic formulations of large displacement analyses (Lagrangian, Eulerian, Updated Lagrangian); the material nonlinearities are not as easily accounted for. While adequate models exist for the nonlinear behavior of steel, the development of an accurate, self-consistent, and unified model for the nonlinear response of plain concrete is still an active area of interest.

In order to achieve a high-quality numerical solution to a given boundary value problem, an improved, rate independent, strain softening, nonlocal Continuum Damage/Plasticity (CDP) model for plain concrete is presented in this paper and certain attributes of this model are developed to facilitate its application in structural elements, such as beams, plates, and shells.

Given the complex behavior of concrete, it is not surprising that a large number of distinctly different constitutive models for concrete have been proposed over the years. Here, only the Continuum Damage Mechanics/Plasticity models and models for strain softening are discussed.

The nonlinear response of concrete is created through the combination of microcrack growth and frictional slip. The theory of Continuum Damage Mechanics accounts for the phenomena of strength and stiffness degradation due to microcracking; the plastic flow and prepeak nonlinearity of concrete can be modelled with the theory of Plasticity. Recently, the two theories have been combined to form a number of successful approaches for modelling plain concrete. One of the first attempts at combining the damage and plasticity phenomena was made by Bazant and Kim '79, who merged a conventional plasticity approach with a strain based fracturing theory. Later, Han and Chen '87 combined a stress based hardening plasticity theory for the pre-failure response of concrete with a strain based plastic/fracturing theory for the response after failure. Using the internal variable theory of thermodynamics, Yazdani and Schreyer '87 developed a Von Mises plasticity surface and a mean pressure sensitive damage surface that accommodates the two modes (shear and tensile) of cracking by taking into account the current stress state at the crack surface as determined by the orthogonal projections of the stress tensor. Also, Simo et al. '87 coupled a conventional stress based Cap model with a scalar damage variable that evolves using the rule suggested by Mazars '82; this approach yielded excellent results. Lastly, Frantziskonis and Desai '87 combined a scalar damage approach with plasticity theory and found good agreement between predictions and test results.

The application of softening, rate independent constitutive models in the treatment of initial boundary value problems leads to a loss of hyperbolicity in the governing equations of motion and to mesh dependency, localization of strains, and erroneous predictions of energy dissipation in numerical calculations; thus, the potential for such negative side effects exists for each of the models mentioned in the previous paragraph. As discussed by Read and Hegemier '84, strain softening in concrete is the direct result of the formation of discrete internal structure due to microcracking. Thus, in the softening range, concrete can no longer be represented as a continuum and some form of representation of the internal structure must be included in the constitutive model. In order to overcome this difficuty in modelling, various methods for enforcing finite energy dissipation over a discrete region of the body and for removing the mesh dependency have been proposed; these include: a composite damage formulation which incorporates a "damage volume" and distinguishes between tensile and shear cracking (Willam, Bicanic, and Sture '84); the introduction of higher order spatial derivatives into the strain displacement relations (Lasry and Belytschko '87); and, the introduction of the strain gradient into the definition of the strength or yield function (Schreyer and Chen '86).

One method of particular interest involves the use of "nonlocal" constitutive laws, in which the dependent variable at a point is not solely a function of the state variables at that point but rather depends on what occurs in the neighborhood of that point. Such an approach was formulated for concrete by Bazant et al. '84, who averaged both stress and strain over the neighborhood of the point and used the nonlocal definitions of the stress and strain directly in the governing equations. Recently, Pijaudier-Cabot and Bazant '87 applied an averaging approach to a nonlocal definition of the damage variable in a Continuum Damage Mechanics model. With this approach, the field equations have the standard form and no extra boundary conditions are needed. Their work is particularly interesting in that they successfully combined their nonlocal approach with a layered beam element to analyze the response of a statically loaded beam; they showed that, due to Euler's hypothesis of plane cross sections, the length for damage averaging can not be less than the beam depth. It should be noted that the use of the beam depth for averaging the damage can be validated physically by examining the hinge formations in beams that have been loaded to failure (Corley '66); in most cases, the hinge length is on the order of 85 to 95 percent of the total depth.

As is well known, rotatory inertia and shear effects significantly alter the response of structural elements that are loaded over a very short time period relative to the element's natural period, and, therefore, a layered, large displacement, large strain, Timoshenko beam element is developed. The proposed constitutive model is combined with this Timoshenko beam element and a strain hardening plasticity model for the reinforcing steel to successfully analyze two simply supported, impulse loaded, reinforced concrete beams tested by Feldman and Siess '58.

A NONLOCAL CONTINUUM DAMAGE/PLASTICITY MODEL FOR PLAIN CONCRETE

The concrete model developed herein is a combination of Continuum Damage Mechanics and Plasticity theories and it uses a nonlocal definition of a scalar damage variable to model strain softening. Various researchers have combined plasticity and continuum damage approaches to successfully reproduce test results of material elements; however, without a consistent technique for stabilizing the strain softening calculations, they appear doomed to the same shortcoming discussed above (mesh dependency, unrealistic energy dissipation, etc.) when applied to realistic boundary value problems. The nonlocal approach described in the following successfully incorporates strain softening effects.

The Continuum Damage Mechanics portion of the approach developed herein and discussed by Stevens and Krauthammer '88 (to appear), is based loosely on the approach proposed by Frantziskonis and Desai '87, in which the strength and stiffness degradation are modeled with a scalar damage parameter. It can rightfully be argued that a complete three dimensional treatment of microcracking effects on the response of concrete requires a higher order definition of the damage variable, and, first, second, fourth, and even eighth order tensors have been proposed. However, in cases where damage directionality is not a dominant feature, such as in the plane strain or plane stress conditions of beams, frames, and slabs, a scalar parameter is sufficient (Resende '87).

The determination of how the averaging of damage is to be performed (in order to develope a nonlocal damage parameter) and the value of the characteristic length, l, (over which the averaging is to be performed) are based on considerations of the proposed application of the constitutive model. As Pijaudier-Cabot and Bazant '87 show, the use of the Euler hypothesis in a beam analysis requires that the averaging length be greater or equal to the beam depth. Therefore, since this constitutive model will be implemented into a Timoshenko beam element, which is based on the Euler principle and, in which, the shear strain is represented kinematically by a rotation of the cross section similar to the flexural rotation (as discussed later), the damage averaging is performed uniaxially at each layer of the beam element, in the direction parallel to the long axis of the beam, and the characteristic length, l is taken as the beam depth. This one dimensional averaging scheme restricts the possibility of strain softening through the depth of the beam; thus, while the nonlocal scalar damage parameter does degrade both shear and normal stresses, a monotonic loading path of pure shear at a cross-section of the beam will result in a constitutive response that is elastic/strain hardening plastic in shear, providing damage has not occurred at the integration points adjacent to the cross section. This shortcoming might be overcome through use of two nonlocal scalar damage parameters, representing tensile and shear damage, separately. However, as the results presented later show, this uniaxial damage averaging technique is suitable for the beams that were analyzed.

The next issue is the form of the evolution equations for the local damage parameter; in this approach, the evolution equations will be parameterized using the concept of equivalent tensile strain (Mazars '82; Ortiz '85; Simo and Ju '87).

The response of the topical (undamaged)

material is controlled by the plasticity portion of the CDP model, which employs a continuous, smooth yield surface that combines a strain hardening modified Drucker-Prager failure surface with a curved cap; this model was developed by Schreyer and Bean '87, who refer to it as a "Prager-Drucker" cap model to differentiate it from the Drucker-Prager cap model commonly used for modelling soils.

A typical modified Prager-Drucker yield surface in the $J_2^{\frac{1}{2}}$, P plane is plotted in Figure 1.

Over the majority of the yield surface, the plastic strain tensor evolves through use of an associated flow rule; however, when the model is specialized from the three dimensional state to a plane strain state (as is typically assumed for analyses of structures that are "long" in the direction perpendicular to the plane of loading), a nonassociated flow rule provides more reasonable results in regions of tensile hydrostatic pressures and low compressive hydrostatic pressures. Under plane strain conditions, the associated flow rule generates dilation, which creates, in turn, an unrealistic confinement stress in the out-of-plane direction; since concrete is a pressure sensitive material, this out-of-plane compressive stress can lead to erroneous predictions of shear and tensile strengths.

In order to obviate this shortcoming, the concrete model proposed herein uses a nonassociated flow rule in regions of tensile or low compressive (less than 0.1 f_c') hydrostatic pressure to reduce the dilational strain predictions while at the same time allowing adequate predictions of strength.

The nonassociated flow rule is implemented with a plastic potential that is chosen as another modified Drucker-Prager surface as shown in Figure 2.

There are two shortcomings to the use of a nonassociated flow rule. First, nonassociated flow rules lead to asymmetric tangential elastic-plastic compliance tensors, which, in turn, are difficult to accommodate computationally in the typical solution schemes used in Finite Element applications. However, since the central difference technique is used to integrate the equations of motion in the Finite Element approach discussed later, the tangential compliance is never explicitly calculated or inverted and this difficulty is avoided on the computational level. Second, and most importantly, the main criticism leveled against the use of nonassociated flow rules is the potential for spontaneous energy generation. This unpleasant feature was first discussed by Il'iushin '61 (a summary of Il'iushin's proof is presented by Sandler and Rubin '87).

The modified Prager-Drucker plasticity model has the following advantages: 1) strain hardening is predicted for all paths, 2) more ductility is predicted for paths associated with large mean pressures, 3) the yield surface intersects the hydrostatic axis at right angles for both positive and negative mean pressures so no special algorithm is needed at these intersection points, and 4) the flow surface is continuous and has a continuous derivative everywhere so a corner algorithm is not required (Schreyer and Bean '87). Although the number of required material constants is large, the values may be deduced directly from conventional uniaxial and triaxial test results; also, Schreyer and Bean '87 and Stevens and Krauthammer '88 present representative values for low, medium, and high strength concretes.

The proposed concrete model (using the local definition of the damage variable) was evaluated successfully, on a material level, through comparisons with three sets of concrete test data; for a full presentation of the results, the reader is directed to Stevens and Krauthammer '88.

TIMOSHENKO BEAM ELEMENT

The kinematic relations for the layered Timoshenko beam element are based on the usual assumptions: 1) plane sections originally normal to the neutral axis remain plane after deformation but not necessarily normal to the neutral axis and 2) the shear strain is constant over the beam's cross section and may be defined as a rotation of the cross section. Assuming small to moderate rotations and small axial strains and, using the definition of the Green-Lagrange strain tensor, the nonzero, nonlinear, strain displacement relations may be written as

$$\epsilon_{11} = U' - \xi_1(\theta'-\gamma') + \frac{1}{2} V'^2 \quad \ldots\ldots\ldots\ldots\ldots (1)$$

$$\epsilon_{12} = \frac{1}{2}[\gamma + U'(\gamma-\theta)] \quad \ldots\ldots\ldots\ldots\ldots (2)$$

where $U = U(\xi_1)$ is the axial displacement of the neutral axis along the beam, $\gamma = \gamma(\xi_1)$ is the shear deformation, β is the total rotation of the cross section, $V = V(\xi_1)$ is the transverse displacement of the neutral axis along the beam, ξ_i are the local beam coordinates ($i = 1,2$), $\theta = V'$, and $(\ )' =$ derivative w.r.t. the independent variable. In this formulation, the axial displacement and the shear rotation are interpolated with linear shape functions acting on the nodal variables, and the transverse displacement is interpolated using the standard cubic Hermetian polynomials acting on the total rotations, or $\beta_i = \theta_i - \Gamma_i$ where θ_i and Γ_i are the flexural and shear rotations, respectively, at node i of the beam. The shear rotations are retained as independent degrees of freedom and continuity of shear across elements is preserved.

In the implementation of the Finite Element method using central difference time integration, the calculation of the internal force vector must be performed. The internal force vector is equivalent, in a virtual work sense, to the internal element stresses created during the deformation of the element and it is defined as

$$\{F_{INT}\} = \int_{Vol} [B]^T \{\sigma\} \ dVol \quad \ldots\ldots\ldots\ldots\ldots\ldots (3)$$

where $\{F_{INT}\}$ is the internal force vector equivalent to the element's stress state, $[B]^T$ is the three dimensional strain displacement matrix, and $\{\sigma\}$ is the Cauchy stress tensor (matrix). For integration through the depth, the element is subdivided into 10 layers and the integration is performed by a summation of the stresses at each layer; the stresses in the steel and concrete are calculated with the models discussed above and a perfect bond is assumed between the reinforcement and concrete. The integration over the length of the element is performed using three point Gaussian integration. Also, the movement of the neutral axis due to the material nonlinearities is tracked with an iterative technique developed by Puglisi and Krauthammer '87.

BEAM ANALYSIS AND DISCUSSION

The Timoshenko beam element was combined with the proposed CDP concrete model and a uniaxial elastic/strain hardening plastic model for the reinforcement steel (see Park and Paulay '75); the shear contribution of the steel reinforcement is assumed small compared to the shear force resisted by the concrete and, thus, the steel response is modelled as uniaxial. The resulting approach was applied to the analysis of simply supported reinforced concrete beams, which were subjected to large amplitude, short duration loads at midspan (Feldman and Siess '58). Figure 3 presents the dimensions, cross sectional geometry and some of the instrumentation for beams H1 and C1; Figures 4 and 5 present the linear approximations of the applied loadings of beams H1 and C1, respectively. During testing, both beams experienced considerable damage and large permanent deflection. The residual midspan displacements were approximately 8 inches and 2.5 inches in beams H1 and C1, respectively.

Due to the symmetry of the beams, loads, and boundary conditions, only one half of the beam was modeled, using the coarse and refined meshes shown in Figure 6. At the right hand node, the horizontal displacement, shear rotation, and bending rotation are restrained.

As is typical with most test reports, only the compressive strength of the concrete and the yield strain and stress of the steel were reported by Feldman and Siess '58. The concrete compressive strengths of beams H1 and C1 were 5960.0 psi and 5830.0 psi, respectively, so "typical" values for medium strength concrete are used in the analysis, as listed in Table 1. Also, typical values for the reinforcing steel were assumed, as listed in Table 2. The densities of the concrete and steel were taken as 150 pcf and 490 pcf, respectively.

The equations of motion were integrated temporally with the conditionally stable central difference technique; the integration time step was chosen as half the critical time step (which was governed by the flexural frequency).

Comparisons between the experimental and calculated displacement histories of Gages 3, 4, and 5 of beam H1 are shown in Figure 7 for coarse mesh. Mesh-sensitivity was checked by using the model with refined mesh and it was observed that this algorithm is not sensitive to the fineness of the model. As this figure shows, there is good agreement between peak displacement, residual displacement and the time when peak displacements occur.

The results in Figure 7 when considered alongwith the mesh-independence of this algorithm and the fact that a significant amount of strain softening has occurred at midspan, show that the computational difficulties normally present with strain softening models have been alleviated with the nonlocal CDP model. In order to verify the benefits of the nonlocal approach, beam H1 was reanalyzed using the coarse and refined meshes <u>and</u> the CDP model <u>without</u> the damage averaging; the computed histories of the midspan displacement for the local and nonlocal, coarse and refined mesh analyses are plotted in Figure 8. As shown in this figure, the local strain softening model overestimates the displacement with the coarse mesh, and, with the refined mesh, the displacement appears to continue to infinity. An examination of the output for these local analyses showed that the damage localized into the element directly next to the load; for the refined mesh, this element became a kinematic hinge and hence the increasing displacement.

Comparisons between the measured reaction at the left end of the beam and the calculated reaction using the coarse mesh for beam H1 are shown in Figure 9. Again, there is very good agreement with the peak reaction and the time of peak reaction, as well as the time when the reaction force returns to zero. However, after approximately 60 msec, the calculated reaction oscillates with a higher frequency than the measured reaction; this difference is due to the fact that the unloading stiffness predicted with the continuum damage/plasticity model is too large (as discussed in Stevens and Krauthammer '88), resulting in a stiffer beam with a higher natural frequency. A correction to the constitutive model would improve the results for the response after 60 msec; however, the key point is that the peak value is correctly predicted as is the time at which the peak occurs and the time when the reaction returns to zero.

CONCLUSIONS

A nonlocal Continuum Damage/Plasticity model has been developed and implemented for the analyses of reinforced concrete beams. In the development of the model, previously proposed formulations were modified and combined into a comprehensive constitutive relationship. This model has been verified for various stress paths and by the analysis of reinforced concrete beams under impulse loading.

The results of the analyses of the two impulse loaded beams agree quite well with the experimental data. The analyses predicts the displacement, reaction, and strain histories very closely. The observed mesh independence is particularly pleasing considering the shortcomings usually associated with strain softening constitutive models.

In conclusion, it appears that the combination of the Timoshenko beam element with the nonlocal CDP model and the uniaxial steel model is capable of representing the dynamic behavior of reinforced concrete beams quite accurately.

ACKNOWLEDGEMENTS

This work was sponsored by the Defense Nuclear Agency under Contract No. DNA001-35C-0410 with the University of Minnesota. The authors wish to thank Dr. H. Schreyer and Mr. J. Bean of the New Mexico Engineering Research Institute for supplying the Prager-Drucker cap model and for their helpful discussions.

Prager-Drucker Cap Model							
	f'_c, psi	E, ksi	ν	n	ϵ_c^p	α	β
H1 C1	5960. 5830.	4400. 4350.	0.20 0.20	0.50 0.50	0.003 0.003	0.60 0.60	1.25 1.25
	P_o, psi	P_{co}, psi	S_m	h_o	m	q	c_1
H1 C1	12000. 12000.	5960. 5830.	$25f'_c$ $25f'_c$	0.60 0.60	0.65 0.65	0.35 0.35	0.40 0.40
	P_t, psi	c_2	c_3	c_{cap}			
H1 C1	-350. -350.	1.00 1.00	1.00 1.00	0.70 0.70			

Continuum Damage Mechanics Model								
	η, psi^{-1}	d_c	r_o	B	C	D	A_{ts}	A_{cs}
H1 C1	0.0005 0.0005	0.875 0.875	0.0035 0.0035	1.30 1.30	8. 8.	10. 10.	700. 700.	50. 50.

Nonassociated Flow Rule				
	ϕ	β	Ω	ω
H1 C1	0.10 0.10	0.001 0.001	0.003 0.003	2.0 2.0

Table 1. Concrete Material Parameters for Beams H1 and C1

Park and Paulay Steel Model					
	f_y, ksi	f_u, ksi	ϵ_y	ϵ_{sh}	ϵ_u
H1 C1	47.2 46.1	72.0 72.0	0.0016 0.0016	0.0144 0.0144	0.150 0.150

Table 2. Steel Properties for Beams H1 and C1 (f_y = yield stress, f_u = ultimate stress, ϵ_y = yield strain, ϵ_{sh} = strain at initiation of strain hardening, ϵ_u = ultimate strain)

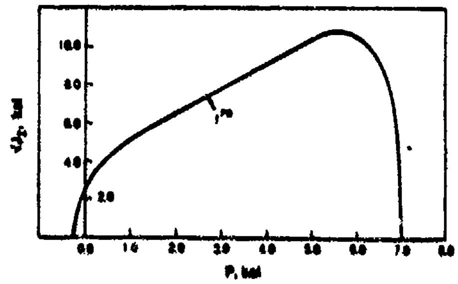

Figure 1. Modified Prager-Drucker Yield Surface

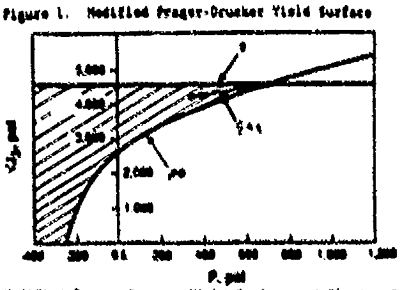

Figure 2. Modified Prager-Drucker Yield Surface and Plastic Potential Surface with Predicted Elastic Stress State Inside the "Wedge"

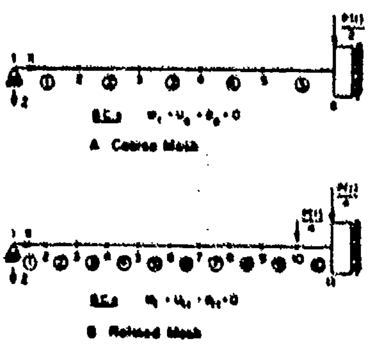

Figure 4. Finite Element Mesh. A) Coarse Mesh. B) Refined Mesh

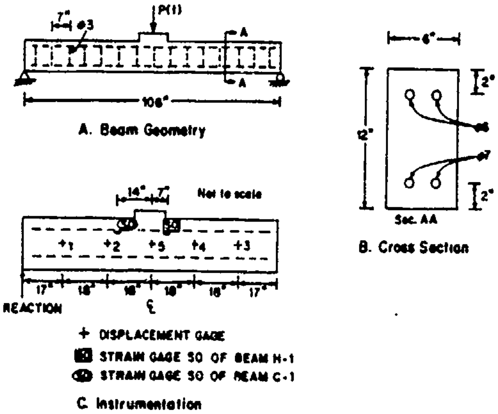

Figure 3. Geometry and Instrumentation of the Feldman and Siess Beams.

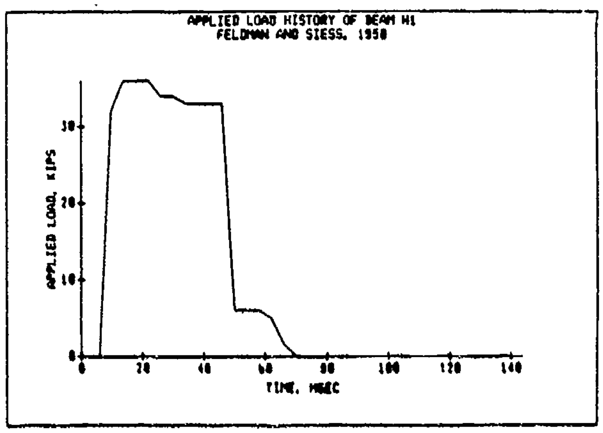

Figure 5. Applied Load of Beam H1 (Linearized).

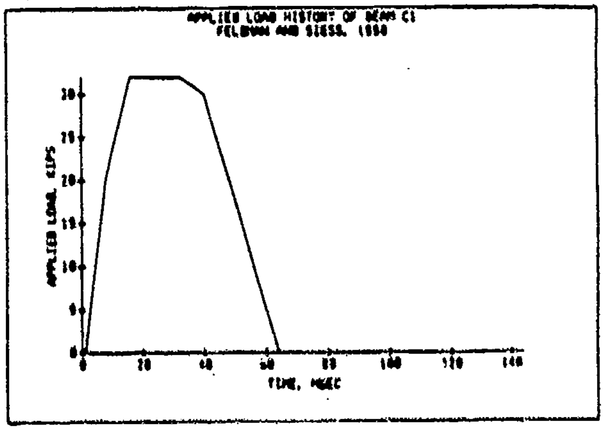

Figure 6. Applied Load of Beam C1 (Linearized)

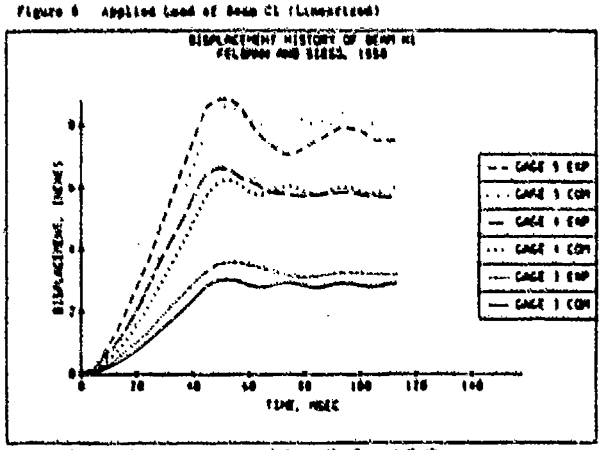

Figure 7. Displacement History of Beam H1, Coarse Mesh.

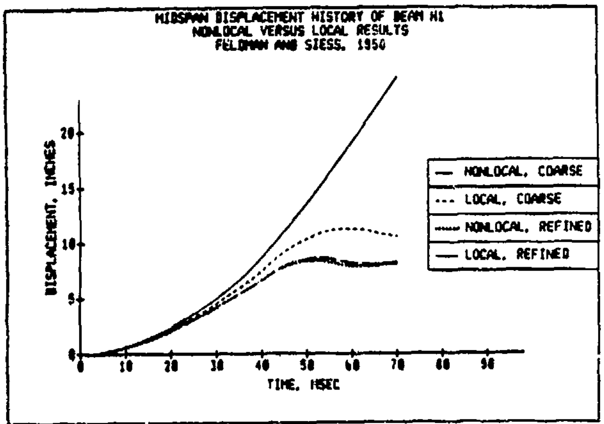

Figure 8. Displacement Histories of Beam H1. Local vs. Nonlocal Approach. Coarse and Refined Meshes.

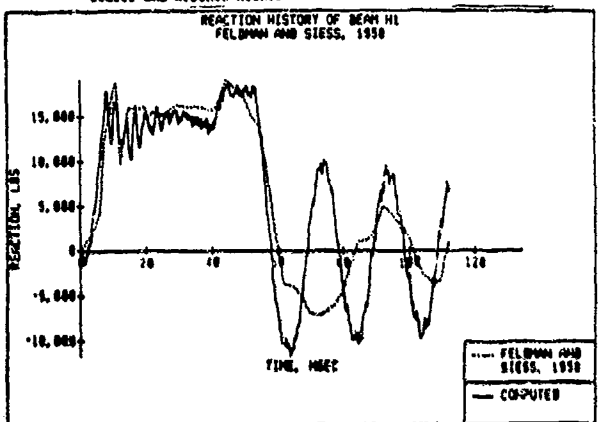

Figure 9. Reaction History of Beam H1. Coarse Mesh.

APPENDIX I. REFERENCES

Bazant, Z.P., Belytschko, T.B.. and Chang, T.P. (1984). "Continuum Theory for Strain Softening." J. Engrg. Mech., ASCE, 110(12), 1666-1692.

Bazant, Z.P., and Kim, S.S. (1979). "Plastic-Fracturing Theory for Concrete." J. Engrg. Mech., ASCE, 105(3), 407-428.

Corley, W.G. (1966). "Rotational Capacity of Reinforced Concrete Beams." J. Struct. Engrg., ASCE, 92(5), 121-146.

Feldman, A. and Siess, C.P. (1958). "Investigation of Resistance and Behavior of Reinforced Concrete Members Subjected to Dynamic Loading, Part II." AFSWP No. 1088, U. of Illinois, Urbana, IL.

Frantziskonis G. and Desai, C.S. (1987). "Elastoplastic Model with Damage for Strain Softening Geomaterials." Acta Mechanica 68, 151-170.

Han, D.J. and Chen, W.F. (1987). "Constitutive Modeling in Analysis of Concrete Structures." J. Engrg. Mech., ASCE, 113(4), 577-593.

Il'iushin, A.A. (1961). "On the Postulate of Plasticity." Prikl. Mat. Mekh., 25(3), 503-507.

Lasry, D. and Belytschko, T.B. (1987). "Localization Limiters in Transient Problems." submitted to Int. J. Solids Struct., Dept. of Mech. Eng., Northwestern University, Evanston, IL.

Mazars, J. (1982). "Mechanical Damage and Fracture of Concrete Structures." in Advances in Fracture Research (Fracture 81), 4, Pergamon, 1499-1506.

Ortiz, M. (1985). "A Constitutive Theory for the Inelastic Behavior of Concrete." Mech. of Mat., 4, 67-93.

Park R. and Paulay, T. (1975). Reinforced Concrete Structures. Wiley-Interscience, John Wiley and Sons, New York.

Pijaudier-Cabot, G. and Bazant, Z.P. (1987). "Nonlocal Damage Theory." Report No. 86-8/428n, revised January 1987, Center for Concrete and Geomaterials, Northwestern University, IL.

Puglisi, R.D. and Krauthammer, T. (1987). "Dynamic Response Analysis of Shallow-Buried Reinforced Concrete Arches." Civil and Min. Engrg. Rep. ST-87-06, University of Minnesota, Minneapolis, MN.

Read, H.E. and Hegemier, G.A. (1984). "Strain Softening of Rock, Soil and Concrete - A Review Article." Mech. of Mat., 3, 271-294.

Resende, L. (1987). "A Damage Mechanics Constitutive Theory for the Inelastic Behaviour of Concrete." Comp. Met. in App. Mech. and Eng., 60, 57-93.

Sandler, I.S. and Rubin, D. (1987). "The Consequences of Non-Associated Plasticity in Dynamic Problems." in Constitutive Laws for Engineering Materials: Theory and Applications, Edited by C.S. Desai et al., Elsevier Science Publishing Co., 345-352.

Schreyer, H.L. and Bean, J.E. (1987). "Plasticity Models for Soils, Rock and Concrete." Report to the New Mexico Engrg. Res. Inst., Albuquerque, NM.

Schreyer, H.L. and Chen, Z. (1986). "One Dimensional Softening with Localization." J. Appl. Mech., ASME, 53, 791-797.

Simo, J.C. and Ju, J.W. (1987). "Strain- and Stress-Based Continuum Damage Models--II. Computational Aspects." Int. J. Sol. Str., 23(7), 841-869.

Simo, J.C., Ju, J.W., Taylor, R.L. and Pister, K.S. (1987). "On Strain-Based Continuum Damage Models: Formulation and Computational Aspects." in Constitutive Laws for Engineering Materials: Theory and Applications, Edited by C.S. Desai et al., Elsevier Science Publishing Co., 233-245.

Stevens, D. J. and Krauthammer, T. (1988). "Development of an Advanced Computational Approach for the Analysis of Buried Reinforced Concrete Structures Subjected to Severe Stress Transients." Civil and Min. Engrg. Rep. ST-88-05, University of Minnesota, Minneapolis, MN.

Stevens, D. J. and Krauthammer, T. (1988) "Nonlocal Continuum Damage/Plasticity Model for Impulse Loaded RC Beams." J. Struct. Engrg., ASCE, (to appear).

Willam, K.J., Bicanic, N. and Sture, S. (1984). "Constitutive and Computational Aspects of Strain- Softening and Localization in Solids." in Constitutive Equations: Macro and Computational Aspects, edited by K.J. Willam, ASME, New Orleans, LA, 233-252.

Yazdani, S. and Schreyer, H.L. (1987). "A Unified Plasticity and Damage Mechanics Model for Plain Concrete." University of New Mexico Report, Unpublished.

RELIABILITY-BASED DESIGN METHODS FOR PROTECTIVE STRUCTURES SUBJECTED TO NON-NUCLEAR MUNITIONS EFFECTS

L. A. Twisdale and R. H. Sues

Applied Research Associates, Inc.
Southeast Division
6404 Falls of Neuse Road, Suite 200
Raleigh, North Carolina 27615

Abstract:

This paper summarizes the result of a Phase I SBIR research effort with an overall objective of reviewing and analyzing stochastic process methodologies for their applicability to protective structure design [1]. The research focused on the following tasks: (1) develop an overview of the phases of protective structure design and identify specific areas where probability-based methods are applicable; (2) identify the steps required for the development of reliability-based design methods for protective structures; and (3) illustrate the application of reliability methods to the analysis of an aboveground structure and a buried structure. The Phase I results indicate that fundamental improvements to the design of protective structures can be achieved through research and application of modern concepts of structural reliability. These improvements include: (1) systematic identification of uncertainties and failure modes; (2) development of reliability-based design factors; and (3) development of an analysis tool for survivable structures and facilities.

USES OF PROBABILISTIC METHODS IN PROTECTIVE DESIGN

The protective design process involves a number of activities or phases that interact in various ways over the design life cycle of a facility. Five basic phases were identified: (1) threat evaluation; (2) mission and performance criteria development; (3) design and analysis; (4) construction; and (5) test and operation. These phases cover the entire range of operations of protective design. Following is a brief summary from Reference 1 of each phase with respect to key uncertainties and the potential applications of probabilistic methods.

Threat Evaluation Phase

The objective of threat evaluation is to determine the wartime attack strategy and types of weapons to which the facility/structure would likely be subjected. Three general types of uncertainties are associated with threat evaluation: (1) attack strategies (decision variables such as aimpoints, number of sorties, and weapon types) that the enemy force might employ on a facility; (2) the modeling or prediction errors associated with a model of attack and enemy weapon characteristics; and (3) the random uncertainties (such as CEPs, fuse performance, bomb survivability) about the mean values of predicted performance. Probabilistic methodologies with direct application to treating and analyzing these uncertainties include (1) decision analysis and game theory; (2) Monte Carlo Simulation; and (3) extreme value theory.

Mission/Performance Criteria Development Phase

In the mission and performance criteria development phase, the stated mission is translated into a set of design requirements for each facility, which can be used to develop design criteria for individual structures. General design criteria specify the acceptable structural performance in terms of limiting damage relative to internal equipment or personnel. In addition to the general design criteria, there are often requirements on design performance. These requirements may be treated as constraints that the design must satisfy. Cost, survivability, maintainability, reliability, and constructability are elements that may be expressed as general criteria or constraints on the design performance. These parameters are essentially decision variables that are established during the criteria development phase. These variables specify the requirements of the facility, and as such, there is generally no need to treat uncertainties. However, uncertainties that result from the predicted performance of a design to meet these criteria may be significant and should be treated in the analysis phase.

Design and Analysis Phase

The design and analysis phase is the central activity of protective design and the one with the greatest focus of research activity. It can be subdivided into three elements: design synthesis, system failure mode analysis, and design analysis. Design synthesis begins with the development of a protective design concept based on the specified threats and the general design requirements. Structural form, material, construction method, location, and external protection are attributes that the designer can select in the development of the design concept. Research in this area deals with basic topics, such as improved materials, as well as innovative concepts for protective construction and basing alternatives. In addition, research tools from optimal design theory and artificial intelligence are relevant.

System failure mode analysis involves the identification of potential failure modes of each element and developing the structure and facility failure paths. For quantitative analysis and complex systems, event tree and fault tree methodologies are useful tools to perform system modeling, identify vulnerabilities, and assess consequences of damage and loss of function. The integration of event and fault trees provides an analytic approach for systematic identification and modeling of the sequence of failure and the determination of the critical elements of a complex system. They provide the best available means for identifying and understanding facility design and operation in a manner that leads to a quantification of system reliability.

The design analysis phase follows the development of the preliminary design concept and the identification of all relevant failure modes. The four basic steps are: (1) obtain information on weapon characteristics; (2) assess weapon effects; (3) develop structural loads from specified weapon threats, characteristics and effects; and (4) analyze structural response. This phase is the central activity of many structural analysts/designers for conventional weapon effects.

Reliability-based design (RBD) methods provide a rational method to treat uncertainties in the design and analysis phase. Once these methods are developed and documented in a research phase, the designer would work with design factors (such as load and resistance factors) and is not required to perform "probabilistic" analysis. As summarized by Ellingwood et al. [2], the principal advantages of probabilistic limit state design are: (1) more consistent reliability (survivability) is attained for different design situations because the different variabilities of the various structural strengths and loads are treated; (2) the reliability level can be chosen to reflect the consequences of damage on structural collapse; (3) the designer achieves a better understanding of the fundamental structural requirements and of the behavior of the structure in meeting these requirements; (4) the design process is simplified by encouraging the same design philosophy and procedures to be adopted for all materials of construction; (5) better judgment can be applied to nonroutine situations; and (6) design manuals can be updated in a more rational manner.

Many subdisciplines of structural reliability analysis provide the methods for developing and implementing reliability-based design. These include second moment methods, stochastic load combination, stochastic finite elements, and design code calibration. Common mathematical tools include applied statistics, Monte Carlo simulation, error propagation, and experimental design. Optimization theory has also been applied to structural design to identify designs that optimize performance (minimum cost, maximum reliability) for specified design criteria.

Construction

Permanent protected structures are often constructed in-place and are therefore subject to construction errors and tolerances. While research and some data on nonprotected construction errors and uncertainties exist, research has not been performed for protective construction. A general belief is that these uncertainties are small compared to those resulting from the response analysis. It is noted that construction errors associated with field fortification and nonengineered structural upgrades should be treated separately.

Test and Operation

The test and operation phase represents the final activity of the integrated design process and structural life cycle. It can be divided into two time periods: peacetime and wartime. In peacetime, controlled experiments and tests are performed to assess structural performance. Experiment design concepts and methods of statistical inference are useful probabilistic methods for these applications. In wartime, the structures will be subjected to effects from enemy weapons. Many structures will be damaged to different degrees. Damage assessments and analyses of safety will need to be performed, both at a field level, and later, in a more detailed engineering analysis. Useful methodologies are system identification, engineering databases, and expert systems technology.

BURIED STRUCTURE ANALYSIS EXAMPLE

This example compares deterministic and probabilistic analyses of a box-shaped structure buried in sandy clay. The threat is given and the damage probability is to be determined as a function of scaled standoff (λ) for $0.5 < \lambda < 3.0$ ft/lb$^{1/3}$. The structure contains critical shock sensitive communications equipment, which has a frequency of 10 Hz in the dominant response mode and is hard mounted to the floor. The structure is assumed to fail to perform its mission if the equipment is damaged.

Deterministic Analysis Methodology

The scope of the deterministic analysis methods for this example is limited to existing design manual type methods. Two failure modes are evaluated: wall flexual failure and excessive floor accelerations.

Wall Flexual Failure. The deterministic method for computing the flexual response of the buried wall is the equivalent single-degree-of-freedom structure-medium interaction (SMI) model [3]. The solution of the equation of motion gives the displacement of the center of the wall. In this approach, the peak free field stress is multiplied by an equivalent uniform load factor given by Kiger [4]. This factor accounts for the nonuniform nature of the loads due to conventional explosives and is a function of the wall aspect ratio and the distance between the bomb and the wall.

Figure 1 shows the center deflection of the structure wall as a function of scaled standoff (λ) predicted by the SMI model. Also shown in the figure is the empirical National Defense Research Committee (NDRC) damage curve for buried reinforced concrete walls. Note that the NDRC curve is for walls with length to thickness ratios (l/d) in the range of 5:1 to 15:1 and face dimensions ratio (a/b) of about 3:5. The example problem wall, however, has an l/d ratio of approximately 2.5:1 and a face dimensions ratio of approximately 0.8:5. Hence, the flexual model used in the SMI analysis is expected to be conservative in predicting damage for this very thick wall. Based on damage level as a function of support rotation [5], the SMI model predicts that wall damage is less than or equal to slight for $\lambda > 2.3$, moderate for $1.7 < \lambda \leq 2.3$, heavy for $1.4 < \lambda \leq 1.7$, and is at incipient failure for $\lambda \leq 1.4$.

Figure 1 shows a sharp transition between predicted damage states for small changes in λ. This is due to the steepness of the deflection versus range curve, which is partly a result of the fast attenuation of peak free field stress with range. The steepness of the curve presents a difficult problem to the analyst since, in a deterministic evaluation, it suggests that he is able to predict that small, almost unnoticeable, changes in standoff result in large changes in predicted damage. Since all the uncertainties in the analysis have been neglected, there is no quantitative procedure to assess the margin between the structure capacity and the predicted response.

In-Structure Shock. The in-structure shock environment is characterized by estimating the response spectra at the center of the structure floor. This response spectra is obtained from estimates of the maximum floor acceleration, velocity, and displacement, using the procedures in References 6 and 7. For this example, only the horizontal motion resulting from the specified side-on burst is considered.

The response spectra for equipment hard mounted to the floor is estimated by scaling the peak floor acceleration, velocity, and displacement by 2.0, 1.5, and 1.2, respectively, as recommended by Kiger [7]. These factors give the amplified motion in the acceleration, velocity, and displacement regions of the spectra, respectively. The resulting analysis indicates that for equipment capacity of 10 g's (for a short duration pulse typical of a conventional weapon), equipment failure would be predicted for $\lambda < 1.0$.

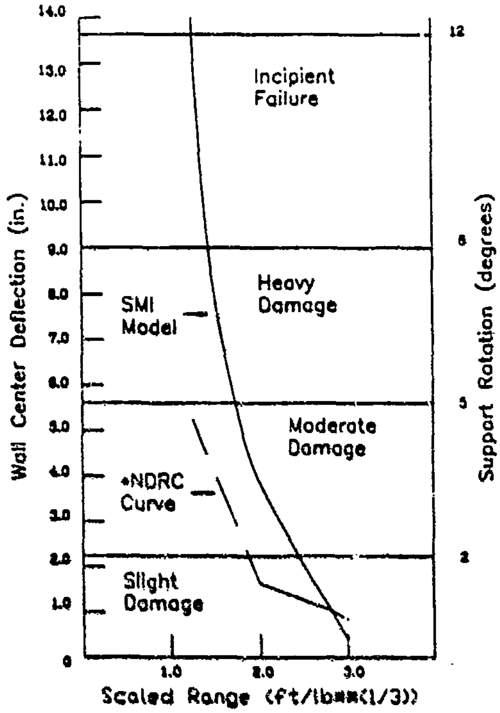

FIGURE 1. Deterministic Prediction of Wall Deflection

Reliability-Based Analysis

Reliability-based analysis involves the performance of a sequence of steps, including failure mode analysis and quantification of uncertainties, prior to the probabilistic evaluation. These steps are described in detail in Reference 1. One of the key outputs of this procedure is the quantification of parameter uncertainties and model prediction errors for existing deterministic analysis approaches. For example, Table 1 summarizes the results of the uncertainty analysis for the flexural failure mode, which are based on both direct data analysis and comparisons of model predictions and experiments, where appropriate.

Monte-Carlo simulation was used to propagate these uncertainties through the deterministic structural response models. The following paragraphs summarize the results of the analysis for each failure mode (wall flexure and in-structure shock), the combined failure probability, and sensitivity analysis.

Wall Flexure Damage. Table 2 compares the deterministic (nominal) and the reliability-based predictions of the deflection of the center of the wall. The differences in the mean and nominal deflections are due to the 15 percent under bias (see Table 1) in the nominal model and the fact that the wall response is nonlinear. Another important observation in Table 2 is the large standard deviations of the reliability-based analysis results.

Figure 2 shows predicted damage as a function of scaled range for the deterministic and probabilistic analysis. Note the so-

Table 1. Uncertainty Analysis for Buried Structure Example

Uncertainty Type, Model and Parameters	Uncertainty Characterization	
	Mean/ Nominal	Coefficient of Variation
1. Prediction Error		
Wall Flexure Model		
Max Deflection	1.15	0.25
L/d Outside Data	1.0	0.15
Limited Data	1.0	0.05
Groundshock Model		
Peak Free-Field Stress	1.0	0.65
2. Random Uncertainties		
Structure		
Concrete Density	1.0	0.05
Concrete, E_c	1.0	0.10
Concrete, f_c'	1.4	0.20
Steel, f_y	1.5	0.15
Soil		
Unit Weight	1.0	0.05
Seismic Velocity	1.0	0.30
Free-Field Stress		
Stress-Decay, α	1.0	0.10
Attenuation Coefficient, N	Treated in Model Pred. Error	
Yield, W	Deterministic	
Range, R	Deterministic (Par. Variation)	
Damage Criteria (Support Rotation)	1.0	0.20

Table 2. Buried Wall Center Deflection Statistics

Range (ft/lb $^{1/3}$)	Deflection(in)		
	Deterministic (Nominal)	Probabilistic Mean	Probabilistic Standard Deviation
1.0	-*	-*	-
1.5	7.9	12.6	20.7
2.0	3.6	5.0	7.6
2.5	1.4	2.2	3.9
3.0	0.4	1.0	2.3

*Wall Collapsed

called "cookie-cutter" shape of the deterministic approach. This sensitivity presents a problem to a designer in light of the obvious uncertainties associated with the predictions of structural response. The probabilistic approach presents a more realistic picture in terms of a continuous, monotonically decreasing curve of damage probability versus scaled range.

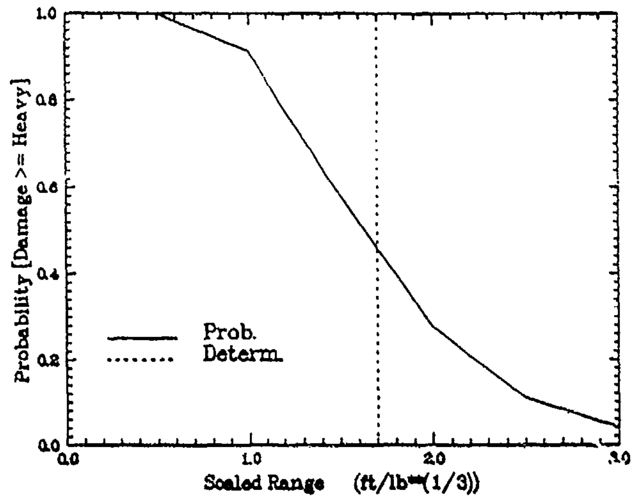

FIGURE 2. Comparison of Predicted Wall Response

In-Structure Shock. The probabilistic analysis of in-structure shock considered uncertainty in the free field ground shock, motion of the structure floor, dynamic properties of the equipment, and response of the equipment [1]. The results are compared in Table 3 to the deterministic analysis. In contrast to the wall response failure mode, there is very little difference in the nominal and mean values.

The predicted in-structure shock accelerations can be used to estimate probability of equipment failure. For this example, the uncertainty in the capacity of the equipment (fragility) is modeled using a lognormal distribution with a mean capacity of 10g's and a coefficient of variation of 25 percent. Figure 3 shows the predicted probability of equipment failure as a function of scaled range.

Combined Failure Modes. The structure mission is compromised if either the wall sustains heavy damage or a critical piece of equipment fails by in-structure shock. These damage modes have been combined exactly within the Monte Carlo simulation. Figure 3 shows the results of this combined failure mode analysis. The probability of failure for the combined modes is equal to or slightly higher than the maximum of either failure

Table 3. Equipment Response Statistics Due to In-Structure Shock

Range ($ft/lb^{1/3}$)	Deflection(in)		
	Deterministic (Nominal)	Probabilistic	
		Mean	Standard Deviation
0.5	14.0	14.2	11.9
1.0	9.6	9.7	8.1
1.5	7.0	..1	5.9
2.0	5.3	5.3	4.5
2.5	4.1	4.2	3.5
3.0	3.3	3.3	2.8

mechanism. The difference between the maximum of the individual modes and the combined curve is not large because only two failure modes have been considered and these are correlated. Also, the wall probability of failure is much larger than the equipment probability of failure (except at the higher scale ranges) so that wall failure dominates. At a scaled range of 3.0, the two models have almost equal failure probabilities and the combined failure probability is approximately double.

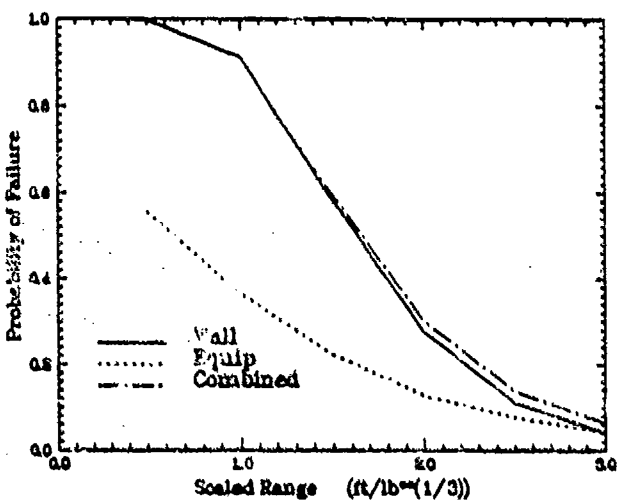

FIGURE 3. Individual and Combined Failure Probabilities

Uncertainty Ranking. The reliability-based analysis indicates large uncertainties about the predicted mean values. Uncertainty ranking and sensitivity analysis are useful byproducts of a probabilistic analysis. For example, the source of the large uncertainty in the predicted wall deflection can be quantified by rank evaluation, based on partial r^2 ($0 \le r^2 \le 1$). The rank analysis was performed by applying stepwise regression analysis procedures to the Monte Carlo simulation outputs. This analysis indicates that uncertainties in predicting structural wall response are dominated by the ground shock model uncertainties in prediction of free-field stress ($r^2 = 0.77$). Soil seismic velocity ($r^2 = 0.03$) and SMI flexure response model ($r^2 = 0.02$) uncertainties contributed to the uncertainty, but were much less important. Uncertainties in structural material properties, strengths, etc., did not significantly contribute to the predicted response uncertainty.

RELIABILITY-BASED DESIGN FACTORS

Probability-based analyses are not always expedient for design, particularly when the structural analyst does not have a background in probabilistic methods. For this reason, reliability based design factors (RBDF) are developed as a research product for application by the designer, much as safety factors are used in traditional design.

The RBDF format is based on the concept of a design factor, which is the ratio of the required *nominal* capacity to the *nominal* structural response. The use of the term *nominal* implies that the capacity and response are computed using ordinary deterministic analysis procedures. Hence, the designer computes structural response (say, for example, wall ductility or equipment acceleration), using standard methods, compares this to the capacity (ductility capacity or acceleration capacity). If the ratio of capacity to response does not meet or exceed the required design factor, then the design is modified to increase the capacity or reduce the response. The required design factor is selected from a table that gives design factors as a function of the survival probability. For example, Table 4 summarizes preliminary design factors developed in the Phase I research effort.

Table 4. Design Factors for In-Structure Shock and Buried Wall Deflection

Desired Reliability Goal (Probability of Survival)	Design Factor	
	In-Struc. Shock*	Wall Deflection**
0.75	1.3	4.9
0.85	1.8	3.0
0.90	2.1	4.0
0.95	2.8	6.2

* Required equipment acceleration capacity = design factor x predicted equipment response acceleration

**Required wall deflection capacity = design factor x predicted wall deflection

These preliminary factors for design reliability (survivability) goals of 0.75, 0.85, 0.90, and 0.95 range from about 1.3 to 3.0 for in-structure shock and from 2 to 6 for buried wall response. Note that the factors are considerably higher for the buried wall design, quantitatively reflecting the much greater uncertainty in predicting wall deflection response. It should be pointed out that, in addition to design application, the RBDF tables can be used as an analysis tool. For a given structure and a given threat, the analyst need only perform a conventional deterministic analysis and compute the inherent design factor (ratio of capacity to response). By entering the design factor table with this computed ratio the probability of survival is obtained.

CONCLUSIONS

The following conclusions are based on the results summarized herein and presented in detail in Reference 1:

1. The potential uses of probability-based approaches to the analysis and design of protective structures have been identified and the advantages illustrated.

2. There is a significant amount of data in many of the key areas that has not been systematically analyzed for uncertainties and model errors. Preliminary analysis of some of these data and comparisons to design methods indicates that nominal design are not always conservative; *i.e.*, (P_s < 0.50) for the cases considered.

3. Fundamental improvements to the analysis and design of Air Force facilities can be achieved through research and application of modern concepts of structural reliability. These improvements would result from:

(a) development of a reliability-based design methodology that would put all protective structure design on a consistent, cost-effective, and a balanced basis, and would bring protective structure design up-to-date with conventional design;

(b) identification of key uncertainties in protective structure analysis and design that would allow a prioritization of important research areas;

(c) development of a systems analysis tool for structures and facilities to develop improved concepts of survivable structures for escalating threats.

REFERENCES

1. Twisdale, L. A., Sues, R. H., and Murphy, C. E., "Assessment of Reliability-Based Design Methodology for Protective Structures," Contract F08635-87-C-0370, Engineering and Services Laboratory, AFESC, Tyndall AFB, Florida, August 1988.

2. Ellingwood, Bruce, Galambos, Theodore V., MacGregor, James G., and Cornell, C. Allin, *Development of a Probability Based Load Criterion for American National Standard A58, Building Code Requirements for Minimum Design Loads for Buildings and Other Structures*, Special Publication No. 577, National Bureau of Standards, Washington, D. C., June 1980.

3. Drake, J. L., Frank, R. A., and Rochefort, M.A., "A Simplified Method for the Prediction of Ground Shock Loads on Buried Structures," *Third Symposium on the Interaction of Munitions with Protective Structures*, Vol. 1, Mannheim, West Germany, March 1987, pp. 3-14.

4. Kiger, S. A., and Albritton, G. E., "Response of a Buried Hardened Arch Structure to the Effects of Localized Explosions," TR-SL-79-13, U. S. Army Engineer Waterways Experiment Station, Vicksburg, Mississippi, December 1979.

5. "Structures to Resist the Effects of Accidental Explosions," TM 5-1300/BNBAVFAC P-397/AFM 88-22, Departments of the Army, the Navy, and the Air Force, Washington, D. C., 1969.

6. Department of the Air Force, *Design for Protective Structures for Conventional Weapons*, Contract F08635-84-C-0275, Air Force Engineering and Services Center, Tyndall AFB, Florida, October 1987 (Draft).

7. Kiger, S. A., Balsara, J. P., and Baylor, J. T., "A Computational Procedure for Peak Instructure Motions and Shock Spectra for Conventional Weapons," *The Shock and Vibration Bulletin*, No. 54, June 1984.

ACKNOWLEDGMENT

This work was supported by a Phase I SBIR contract from the Air Force Engineering and Services Center, Tyndall AFB, Florida.

EXPEDIENT METHODS OF PROTECTION TO MITIGATE STRUCTURAL DAMAGE AND SPALL

D. W. Hyde

U.S. Army Engineer Waterways Experiment Station
Vicksburg, Mississippi

ABSTRACT

A series of full-scale tests using general purpose bombs was conducted on a hardened reinforced concrete aboveground structure. Several expedient methods of mitigating structural damage due to airblast and fragment impacts were tested, and the response of the walls of the structure was monitored.

Results from these tests indicate that bare reinforced concrete walls will be significantly damaged by the given weapon. On the exterior surface, several inches of concrete cover will be destroyed by fragment impacts, and on the interior surface, high-velocity spall will occur. This damage can be prevented by the use of any number of expedient methods outlined in this paper. The most cost-effective method appears to be a soil berm.

BACKGROUND

The U. S. Air Force, Europe (USAFE) is responsible for the design and construction of military facilities which meet the NATO semihardened structure requirements for protection against conventional weapons. NATO requirements and current design procedures have led to the use of heavily reinforced 25.5-inch thick concrete walls to resist these loads. However, tests conducted in 1980-1982 by the German Bundeswehr Infrastructure Staff (References 1 and 2) indicated that these walls were typically over-reinforced and that more economical designs with less steel reinforcement would provide the required protection.

A series of NATO Semihardened Design Criteria Full-Scale tests were conducted by the Air Force Engineering and Services Center (AFESC) and the U.S. Army Waterways Experiment Station (WES) during the summer of 1987 (Reference 3). The objective of this test series was to determine the effects of revetments and sand berms on the response of reinforced concrete walls subjected to the nearby detonation of a cased munition.

TEST DESCRIPTION

The full-scale series was composed of several tests with a nearby detonation of a general purpose bomb located at various positions around the test structure. The bombs were placed at the same range from the test structure for each of the test events discussed in this paper. The test structure was of reinforced concrete construction, approximately 50 feet wide by 60 feet long. All of the tests were instrumented to record airblast pressure loading on the walls, in-structure acceleration, and wall deflection versus time.

Each of the walls discussed in this paper were 25.5-inch thick sections with 0.25 percent steel reinforcement. One bare wall was tested as a baseline; additional protective measures tested included a sand berm, a sacrificial pre-cast panel, sand-grid revetments, and a portable Bitburg revetment.

Each of the 25.5-inch walls had 0.25 percent vertical steel reinforcement in each face consisting of Number 5 bars spaced at 5 inches. Horizontal reinforcement consisted of Number 3 bars spaced at 4.5 inches. Single-leg stirrups fabricated from Number 3 bars provided shear reinforcement. The stirrups were spaced at 18 inches on each vertical bar, and staggered at 9 inches off-center every other bar. Each of the walls had a clear span of about 13 feet-2 inches, and a concrete cover of about 3 inches on the exterior face and 3/4 inch on the interior face.

Several concepts designed to attenuate the airblast and minimize spalling were considered in the full-scale test: (1) a 4-foot-7-inch sand berm with a 2:3 slope; (2) a 6-inch thick lightly reinforced pre-cast panel, anchored to the structure with removable bolts at the top and with a small gap between panel and structure; (3) sand-grid revetments; (4) portable Bitburg revetments.

1. Sand Berm

Previous half-scale tests (Reference 4) have indicated that the addition of a berm to the exterior of the structure will reduce midspan deflections and virtually eliminate spalling. A berm of silty sand (taken from the test site) with a slope of 2:3 was placed against one 25.5 inch wall. The berm extended only part way up the wall, since previous tests had indicated that the most severe blast loads and fragment damage occurred near the ground surface. The berm was about 4 feet-7 inches high.

2. Pre-Cast Panels

The German Bundeswehr Infrastructure Staff had previously conducted half-scale tests of 4- and 6-inch pre-cast panels with favorable results. In the German tests, the pre-cast panels were completely destroyed, but they did protect the main structure walls from fragment damage and eliminated spall. The panel used in the full-scale series was

6 inches thick.

3. Sand Grids

Sand-grids were developed at WES as a rapid means of constructing roadways on beaches for military vehicles (Reference 5). These sand-grids have since been tested as revetments for artillery emplacements with good results (Reference 6). Sand-grids consist of 8-inch high high-density polyethylene strips connected by ultrasonic or heat welds. They are manufactured and shipped in collapsed 4-inch thick sections that expand to 20 feet during construction. Each expanded grid section is either 4 or 8 feet wide by 20 feet long and contains a honeycomb arrangement of cells.

4. Bitburg Revetments

The Bitburg portable revetments are modular reinforced concrete sections intended to protect items less than 6 feet tall (see Figure 1). Each section was about 6 feet-7 inches wide and 6 feet-7 inches high.

RESULTS

Although each of the test events was unique, a few general observations can be made. For all aboveground tests against unprotected walls, damage to the exterior of the structure was similar. The cover concrete on the exterior face of the lower half of the wall was eroded away by the fragments, exposing the reinforcing steel. Spalling on the interior face of the unprotected walls was limited to the depth of the reinforcement, and was greatest in the lower one-third of the wall span. No spall was associated with the pre-cast panels or sand berm, and there was very little sp[illegible] damage with the Bitburg revetments or sand-grid revetments. Direct comparisons of peak pressure measurements made on the exterior face of each wall are given in Table 1, and wall response f[illegible] each event is given in Table 2. A detailed description of all test results follows.

1. Pre-Cast Panels

The lower half of each of the panels was completely destroyed during the test event, while the upper halves were left intact, but fell to the ground. The panels prevented all but a few fragments from penetrating the wall of the structure (See Figure 2). The average peak pressure behind the panels was about 350 psi, compared to peak pressures of 2000-5000 psi at similar ranges on an unprotected wall. The peak acceleration of the wall, measured 5 feet from the floor surface and opposite the weapon, was about 8900 g's, and the peak measured deflection was about 1.6 inches. The interior of the test wall sustained minor cracking, but had no spall damage.

2. Bitburg Revetments

The Bitburg revetments were originally designed to protect fuel storage tanks and other items less than 6 feet tall from fragmentation and airblast effects. The Bitburg design was selected for testing because of its ready availability on US Air Force bases and because of its portability. The revetments were placed directly against the wall of the structure, with about 8 inches clearance between the wall and the vertical section of the revetments. The revetments directly in front of the threat weapon were almost completely destroyed by a combination of airblast and fragmentation effects (Figure 3), but the wall behind the revetments was largely undamaged. As in previous test events, there was extensive concrete cratering on the unprotected portion of the wall. The interior of the test wall sustained minor cracking in addition to slight spall damage (Figure 4).

The peak airblast measurements from this event illustrate the benefit of using revetments to shield a structure from airblast: the peak pressure measured 3 feet, 4 inches from the ground surface and directly opposite the weapon was about 232 psi, while the peak pressure 6 feet, 7 inches above the ground surface (just above the top of the revetments) was about 2270 psi. The peak acceleration of the wall, measured 5 feet from the floor surface and opposite the weapon, was about 900 g's, and the peak measured deflection was about 1.4 inches.

3. Sand-Grid Revetments

The sand-grid configuration tested consisted of twelve layers of 4-foot wide sand-grid sections (total height about 8 feet), placed with a small clearance (about 4 inches) between the revetment and the structure. Construction of the revetment is shown in Figure 5. The sand-grid, as expected, was badly damaged by the test event (Figure 6), but allowed no new fragment penetrations into the structure below about 10 feet, and significantly attenuated the peak pressures measured on the exterior of the structure wall. The peak airblast measurements on the structure and behind the revetment ranged from about 109 psi to 297 psi. The peak airblast measurement on the wall was about 2500 psi, occurring just below the roof, directly opposite the weapon. The peak acceleration of the wall, measured 5 feet from the floor surface and opposite the weapon, was about 170 g's, and the peak measured deflection was about 0.7 inches. The interior of the test wall sustained minor cracking in addition to slight spall damage.

4. Sand Berm

This test event was designed to evaluate the performance of a sand berm in attenuating the damage to the exterior of the structure. Constructed from a silty sand taken from the test site, the berm was about 4 feet-7 inches high with a 2:3 slope. The berm is shown pretest in Figure 7.

A posttest photograph of the berm is shown in Figure 8. The peak interface pressures measured at the interface of the berm and structure ranged from 74 psi to 512 psi directly opposite the weapon. The peak airblast measurements on the wall and above the berm ranged from 326 psi near the roof of the structure to 3380 psi directly above the top of the berm. The berm proved to be one of the more effective measures evaluated in mitigating structural damage. Cratering of the exterior face of the structure was limited to that portion of the wall above the berm. This area could easily be minimized by increasing the height of the berm. As shown in Figure 8, an added advantage to the use of soil berms is their inherent multiple strike capability: most of the material of the berm was left in place. The peak measured acceleration of the wall about 5 feet from the floor surface was about 1750 g's. There was no spall and only minor flexural cracking associated with this test event.

5. Baseline 25.5 inch Wall

This test event was designed to test a baseline unprotected 25.5 inch wall. For this test event, the weapon was kept at the same standoff distance from the structure as in previous events.

As expected, this test resulted in much more damage to the exterior of the structure than any of the previously mentioned tests (Figure 9). Unlike any of the previous test events, this event resulted in a large quantity of high-speed spall fragments (Figure 10). The interior of the structure was littered with spall fragments located anywhere from immediately inside the test wall to the other side of the structure, about 60 feet distant. The peak pressures measured outside the structure and immediately opposite the weapon ranged from 400 psi to over 2800 psi. The peak acceleration of the wall, measured 5 feet from the floor surface and opposite the weapon, was about 21000 g's, and the peak measured deflection was about 2.5 inches.

SUMMARY

Loading on the exterior face of the structure from the detonation of the criteria threat is due to a combination of airblast and fragment impact. For walls unprotected by berms or revetments, the peak pressures are highest near the ground surface and directly opposite the weapon, and lower on other portions of the wall. The airblast distribution is highly transient, concentrated near the bottom of the wall at early time after detonation and decaying at a fast rate to a lower magnitude later in time. The greatest density of fragment impacts occurs on the lower portion of the wall. These impacts destroy the cover of concrete in this area, exposing the exterior reinforcing steel and weakening the wall.

For walls with berms and revetments, the peak pressures are highest on the upper portion of the wall (just above the berm or revetment), and are significantly reduced on the lower portion of the wall under the cover of the berm or revetment. Both the average blast pressure and impulse are significantly lower for the protected walls. The berms and revetments are also very effective in stopping fragments.

All expedient methods used in the full-scale test to reduce spallation were effective. The use of berms eliminates spall entirely and is the most cost effective solution. The portable Bitburg revetments work well (for a single hit only), and are portable and easily replaced. The sand grid is an expedient means of protection for single hits. The polyethylene grid can be compressed for easy storage prior to it's use.

Since the primary damage mechanism for the bare walls was spallation, increasing the steel reinforcement from 0.25 percent is ineffective, unless additional shear reinforcement is added and rebar spacing is minimized. Walls protected by a berm or revetment performed the best due mostly to the fact that the berm or revetment reduces the load. They respond in a flexural mode with very little deflection and only minor structural damage.

ACKNOWLEDGEMENTS

This research was sponsored by the U.S. Air Force Engineering and Services Center, Tyndall AFB, FL, under the direction of LTC Bob Majka. Permission to publish this paper was granted by the Office, Chief of Engineers.

REFERENCES

1. Pahl, H., and Kropatscheck, M., Explosive Tests on Reinforced Concrete Elements Performed By Test Site 91 of the Federal Armed Forces at Meppen, Infrastrukturstab Der Bundeswehr, WWTB-80-17, Summer 1980.
2. Loos, G., and Pahl, H., Quick Look Report - Explosive Tests on Underreinforced Model Structures in Incirlik (Republic of Turkey) and Meppen (Federal Republic of Germany), Infrastrukturstab Der Bundeswehr, TB-82-01, January 1982.
3. Hyde, D.W., NATO Semihardened Facilities Full-Scale Tests (draft), U.S. Air Force Engineering and Services Center, April 1989.
4. Coltharp, D., Vitayaudom, K, and Kiger, S., Semihardened Facility Design Criteria Improvement, US Air Force Engineering and Services Center, Technical Report ESL-TR-85-32, September 1985.
5. Webster, Steve L., Sand-Grid Demonstration Roads Constructed for JLOTS II Tests at Fort Story, Virginia, Technical Report GL-86-19, U.S. Army Engineer Waterways Experiment Station, Vicksburg, Mississippi, November 1986.
6. White, Robert J., Field Artillery Emplacements Development and Weapons Effects Evaluation, Technical Report SL-83-1, U.S. Army Engineer Waterways Experiment Station, Vicksburg, Mississippi, March 1983.

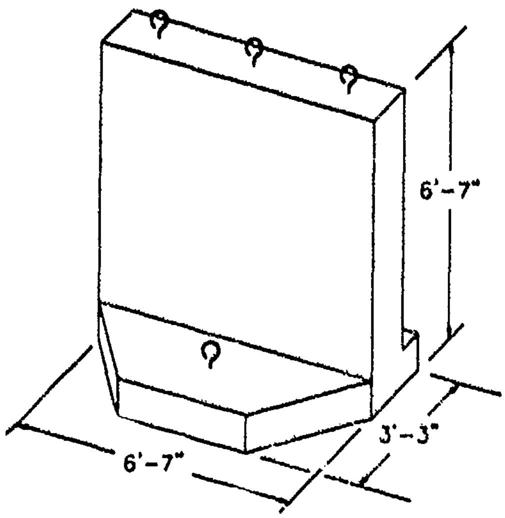

Figure 1. Bitburg revetment

Table 1. Peak Pressure Comparisons

Distance up Wall	Peak Pressure Measurement, psi				
	Baseline*	Pre-Cast Panels	Bitburg Revetment	Sand-Grid Revetment	Sand Berm
0	7035.	385.	714.	125.	512.
2'-3"					482.
3'-4"	1720.	370.	232.	150.	
6'-7"	2565.	359.	2270.	297.	>3300.
13'-2"	1214.	203.	497.	2500.	806.

* Composite from several test events.

Table 2. Wall Response Comparisons

	Baseline	Pre-Cast Panels	Bitburg Revetment	Sand-Grid Revetment	Sand Berm
Accleration, g's	21000	8900	900	170	1750
Deflection, inches	2.5	1.6	1.4	0.7	>2.

Figure 2. Damage to precast panels

Figure 3. Damage to Bitburg revetments

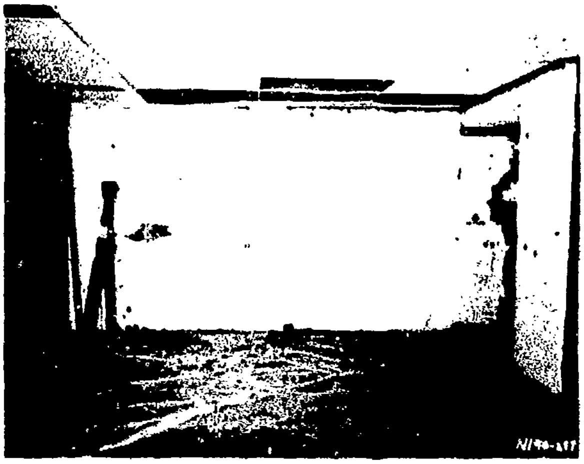

Figure 4. Interior of structure following Bitburg revetment test

Figure 6. Damage to Sand-Grid revetment

Figure 5. Construction of Sand-Grid revetment

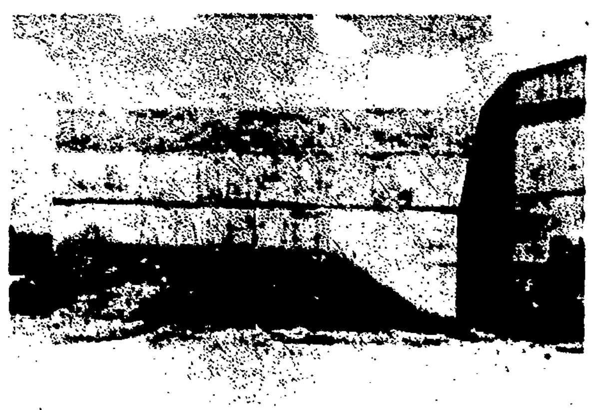

Figure 7. Pretest view of sand berm

Figure 8. Postest view of sand berm

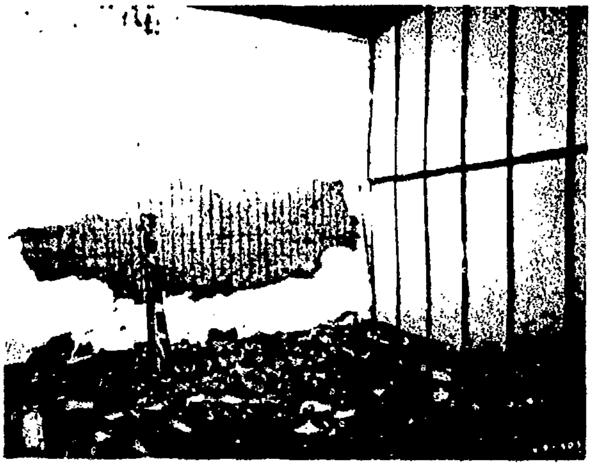

Figure 10. Interior damage to baseline test wall

Figure 9. Damage to baseline test wall

PROTECTIVE CONSTRUCTION DESIGN VALIDATION

LT COL ROBERT J. MAJKA AND MR WALTER C. BUCHHOLTZ

HQ AIR FORCE ENGINEERING AND SERVICES CENTER

Air base facilities that will resist the effects of a conventional weapons system are expensive. Elements include tons of concrete, tightly spaced heavy reinforcing bars, and costly blast-resistant air valves which prevent explosive overpressures from entering the shelter through heating or air conditioning systems.

Recent validation of the North Atlantic Treaty Organization (NATO) aircraft shelter design, conducted by the Air Force at Tyndall AFB, Fla., proved that less costly shelter design could be just as effective.

The test goal was to determine the optimum combination of structural features needed to protect personnel and equipment while reducing construction costs.

Background

Headquarters, U.S. Air Forces, Europe (USAFE) is responsible for the design and construction of military facilities that comply with NATO protective structure requirements.

Tests by the German Bundeswehr Infrastructure Staff showed that the typical semihardened facility was overreinforced and that a more economical design was appropriate. Shelters are designed to resist large localized loads from conventional weapon detonations on exterior walls.

Two considerations not satisfied in the German concept were interior wall spall and deflection of walls. Spall occurs when blast pressure loading or the impact of a high energy object (such as a large fragment) cause a stress wave to travel through a wall and reflect off the interior wall surface. The concrete between the reinforcing bars and the surface is spalled at velocities high enough to damage equipment or critically injure personnel inside the structure.

Spalling is related to the rate of deflection. Deflection can also displace the primary shelter structure from its foundations.

Test methods were significant because they were done in two phases. The first utilized scale model structures. After confidence limits were established on concepts being tested, a full-scale test was used. Most earlier shelter testing used costly full-scale shelters subjected to explosive events. This restricted a multiple trial approach.

Values gained from the scale-model effort were then used to design a full-scale facility. Research dollars were saved by incorporating these results into one full-scale test.

The full-scale test offered an opportunity to evaluate several protective blast valves and doors at the same time. These were

NATO full-scale hardened shelter, shown during construction.

previously evaluated only against blast pressures generated in a laboratory and not tested against fragment and blast loadings generated by conventional weapons.

All construction was accomplished in-house by the HQ AFESC Operations Support Branch, further saving money. Support in design, instrumentation and photography was received from the Corps of Engineers, Waterways Experiment Station (WES), Vicksburg, Miss.

The first scaled test series addressed the deflection problem. Walls were constructed with various percents of principal steel reinforcement. Also evaluated to determine the best shear reinforcement and resistance to deflection were the performance of stirrups (concrete shoes which hold walls in place) and dowels (large pins which anchor overstructures to their foundations).

The second scaled test series evaluated various ways to prevent spall.

All tests were conducted at the HQ AFESC Facilities and Pavements Test Site.

Subscale Testing

Half-scale, reinforced concrete box structures were used in both scaled test series. Each was designed to model wall, roof and floor slab sections of a typical semihardened facility. Scaled, cased charges at a specified threat distance were used to simulate a conventional weapon detonation.

Fourteen scaled tests were conducted in two series (six in Series I and eight in Series II). In Series I, various percentages of the structural volume occupied by principal steel including high-density, medium low density, and two levels of low density were used in each face. (The current design requires one of the high-density standards). The floor and roof designs were consistent with current semihardened design requirements. Test sections were placed against an L-shaped reaction structure so that movement was minimized (Figure 1). Past testing indicated that shear failure in the wall was possible. Single-leg shear stirrups were used in four tests, while dowels were used in two tests.

The Series II tests evaluated three methods for controlling spall (Figure 2): earth berms, interior spall plates, and thicker walls. Berms were constructed from silty sand with slopes of 1:1.5 extending partially up the walls.

Series I tests provided blast and fragment patterns and established critical heights for the protective devices. Steel spall membranes were installed halfway up on the interior low-thickness wall. Thicker walls were also tested. Because of reinforcement, the thicker wall had the same flexural capacity as one with a high-percentage of steel reinforcement and low thickness.

Full-Scale Facility Testing

A full-scale facility (15m wide x 18m long, x 7.5m high) was completed in April, 1987. A partial penthouse along the east side (2.7m high by 3.7m wide by 18M long) contained various blast valves.

One set of blast valves was connected to an operational test ventilation system.

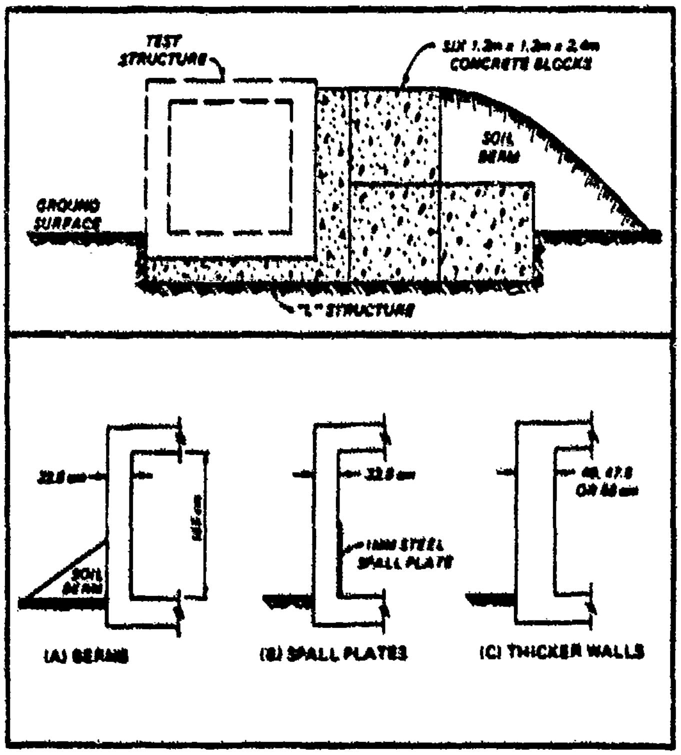

Figures 1, top, and 2, bottom.

The blast valves were placed at three locations to test their performance under different conditions (see Figure 3 on next page) along the east wall of the penthouse, in a protective structure at the north end of the penthouse, and behind a blast wall along the west wall of the facility. This was the lowest location and subjected the valves to the most critical environment, including bomb fragments, dust, soil, and concrete fragments from the facility components.

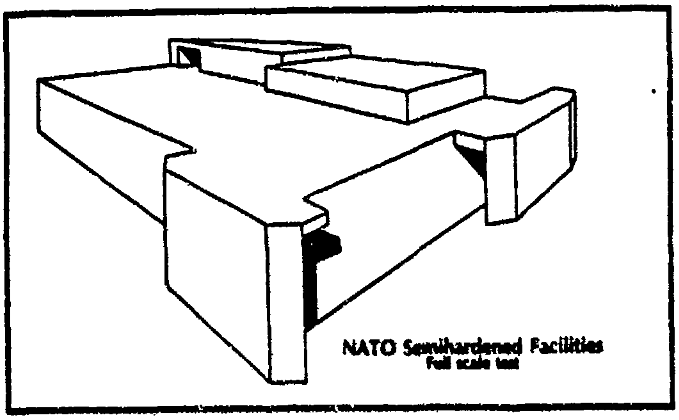

Figure 3. NATO semihardened facilities full-scale test.

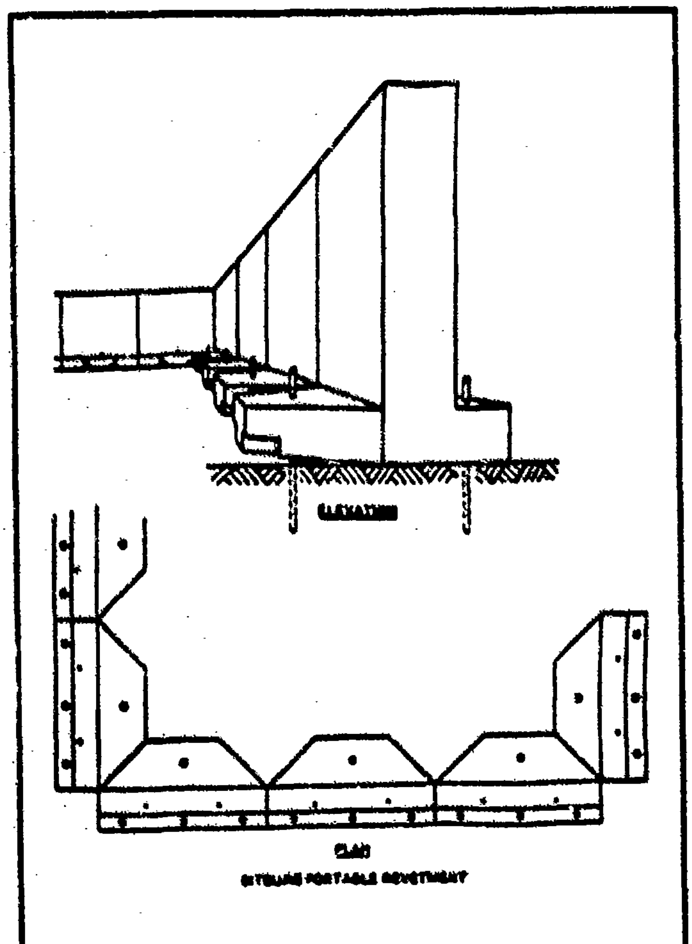

Figure 4. Bitburg portable revetment.

The south, east and west walls were 65 cm thick with high principal steel reinforcement at both faces. Because the north wall was 80 cm thick with medium principal steel at both faces, it had the same flexural capacity as the 65 cm wall.

The five blast doors tested included two from WES, and one each from Luwa Ltd. (Switzerland), Temet USA INC., and the United Kingdom Public Services Agency, manufactured by Energy Equipment Co. Four blast valve designs were tested from Luwa Corp., J.P. Sheltec (Sweden), Bately Valve Co. (England), and Temet USA Inc.

The north half of the facility also had a basement constructed underneath it to be tested against buried weapons. Motion data, using standard office furniture and instrumented mannequins, were recorded principally in the basement and on the first floor. In-structure shock or acceleration of the floor was recorded to determine equipment response and operability. A backup power generator bolted directly to the floor, with no shock isloation equipment, was operational during the first two tests. Spall plates inside of the east wall were welded to a steel frame and anchored along the ceiling and floor by angle iron. Anchors extended from the plates and were cast in place when the concrete walls were poured.

Several other protective systems were tested to determine their effectiveness in preventing spall. Full-height precast concrete panels were bolted to the south wall, with 3-inch air gaps between the wall and the panel. Bitburg revetments approximately 2 m high were also tested (see Figure 4). A sand berm (see Figure 5 on next page) constructed along the west wall was tested for spall protection, as was a sand grid system along the south wall. Ressembling a corrugated paper packing carton bottle protector, when pulled apart, the grid material forms a honeycomb pattern. Sand is poured into the honeycomb openings until they are filled, after which new sand and honeycomb layers are completed until the sand grid is approximately 2 m high.

Chamber revetments were also

tested against a different weapons threat, because they were located farther from the detonation. These revetments can be tasked to 3 m height and connected inside with steel straps and filled with sand. They are made from standard concrete and are reinforced with steel mesh, steel fiber or polypropylene fiber. The mesh and fibers were also combined for reinforcement in several chambers (Figure 6).

Equipment Test Results

The half-scale tests provided valuable installation data. The anchors, steel frame and angle iron installation were the keys to the successful performance.

All blast doors received damage in different amounts from the bomb fragments. Locking devices, hinges and door frames were weak. Several doors were subjected to mulciple detonations. Outer steel surfaces were damaged but no doors were penetrated completely by the bomb fragments. All doors provided adequate blast protection, although one door frame, damaged by fragments, was breached and interior facility damage occured.

All blast valves functioned adequately when first tested. Location of the valves was critical because dust, soil and concrete fragments affected their operation. After repeated testing, several valves failed to open. The valves are normally installed in banks of several valves each. Overall performance of the valves is still being analyzed.

The ventilation system and power generator functioned properly during the tests, with no damage to system components. The spall plates functioned extremely well, with minimum wall deflection and no spalling.

Structural Test Results

The facility systems performed extremely well against specified weapons threats. There are some additional conclusions: Blast doors must not be in the weapon line-of-sight or severe fragment damage may result. Blast valves must be placed above the facility, in a protective enclosure, to minimize or eliminate blast pressure, bomb fragment damage, and damage from soil or concrete fragments.

Thick walls with sheer stirrups and a reduced percent of reinforcing steel worked extremely well, with deflection low. The unprotected wall experienced spall problems, but when protected by precast panels, Bitburg revetments, sand grid or sand berm, no spall was observed. The sand berm provided the best overall protection.

The chamber revetments combining steel mesh and fiber reinforcement (steel or polypropylene) were effective. Although sections were subjected to six detonations, no fragments penetrated the rear surfaces, demonstrating excellent protection for equipment or facilities against fragment damage. The thickest wall provided no additional protection over the less thick wall, therefore additional construction costs are not justified. Deflection was minimal but spall still occured.

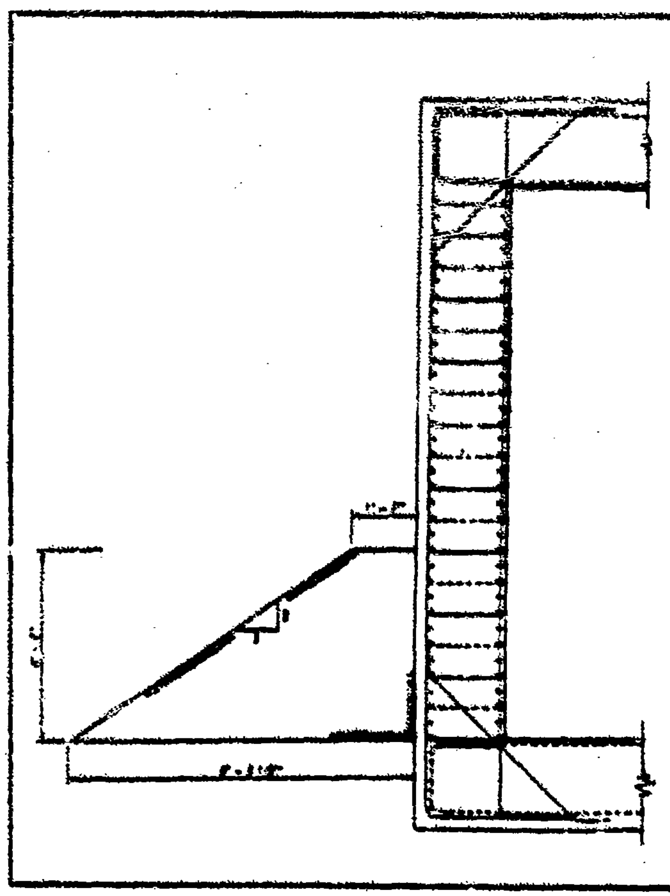

Figure 5. Cross section, bermed wall.

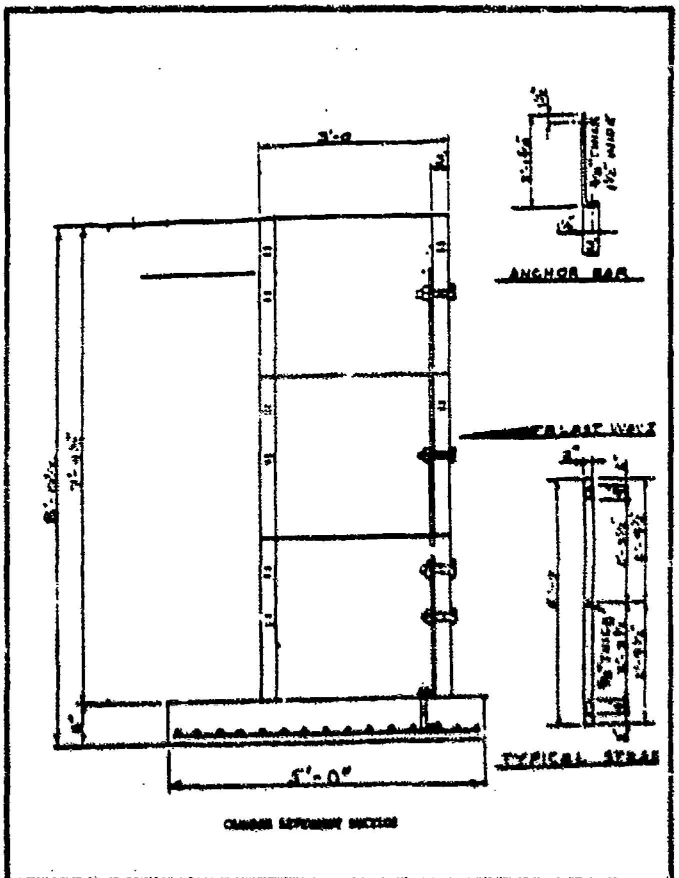

Figure 6. Chamber revetment section.

Conclusion

Limited full-scale testing validated design parameters established in reduced scale tests. The newly developed wall design provided protection and reduced construction costs by reducing the percent of steel used to reinforce the wall. Conducting scaled tests to check a multitude of research areas reduces test costs and saves valuable research dollars.

SHOCK ISOLATION FOR CONVENTIONAL WEAPONS

S. A. Kiger, J. H. Weathersby, D. W. Hyde

U.S. Army Engineer Waterways Experiment Station
Vicksburg, Mississippi

ABSTRACT

A series of full-scale tests using general purpose bombs was conducted on a hardened reinforced concrete aboveground structure with a partial basement. Weapons were placed in both above- and below-ground configurations, and the response of various types of equipment, computers, and instrumented mannequins were monitored.

Results from these tests indicate that any equipment not restrained against movement, i.e. simply sitting on the floor or isolation pads, will undergo significant rigid body displacements. In general the best isolator performance was obtained from the cupmount series neoprene isolators. Results also indicate that the only real danger of injury (from shock) to personnel is from falling equipment, e.g. bookshelves, cabinets, or light fixtures.

BACKGROUND

Shock isolation for equipment in blast-resistant structures can be a costly and uncertain procedure for conventional weapon threats, especially for aboveground structures with combined airblast and fragment loading. The in-structure shock environment is known only approximately at best. Methods for calculating in-structure shock for aboveground structures generally assume plane wave loading on the structure, instead of the highly localized transient loads generated by conventional weapons, and they typically ignore fragment loads. Also, there are almost no data on modern communication and computer equipment fragility. This usually leads to an over-designed and expensive shock-isolation system whose performance is uncertain.

A series of NATO Semihardened Design Criteria Full-Scale tests was conducted by the Air Force Engineering and Services Center (AFESC) and the U.S. Army Waterways Experiment Station (WES) during the summer of 1987 (Reference 1). During August 1988, the WES conducted a second series of tests on the same full-scale structure (Reference 3). The 1988 tests were sponsored by the Defense Nuclear Agency (DNA) in cooperation with AFESC to further evaluate in-structure shock and shock isolation methods. Equipment tested in this second series included a computer, several pieces of electronic equipment, a large air-handling unit, and a 1,000-kw generator. Shock-isolation methods were evaluated by repeating tests under several different isolation conditions, including a baseline test with the equipment hard-mounted.

In the 1987 test series all equipment was bolted directly to the floor in a hard-mounted configuration, or simply unattached, as with some desks and bookshelves. Data from these tests indicate relatively high acceleration levels within the structure, but the generator and air-handling equipment remained operational before, during, and after the tests. In Figure 1 the shock spectra generated from a typical acceleration data record measured near the base of the air-handling unit is compared to a fragility curve for air-handling equipment from TM5-855-1 (Reference 2). The measured acceleration levels clearly exceed the allowable limits indicated by the fragility curve. Since the air-handling unit continued to operate, the fragility curve (at least in this case) is conservative. Peak in-structure spectra accelerations from 1000 g's for buried shots to 10,000 g's for aboveground shots were calculated from the acceleration data; however, relative displacements associated with these accelerations were very small (0.01 inch to 0.001 inch). Figure 2 shows a postest view of prepositioned mannequins in sitting and standing positions. Data from these tests indicate the only injury to personnel would have been from falling objects, such as the bookshelf in Figure 2. Data from the test series conducted in 1988 are summarized below.

TEST DESCRIPTION

A series of three experiments using buried general purpose bombs were conducted on the full scale semihardened test structure at Tyndall AFB, FL. The objective of these experiments was to determine the shock attenuating capabilities of four simple shock isolation systems. Several pieces of equipment were placed inside the building, and acceleration measurements made with the equipment both hard-mounted and shock isolated using various shock isolation methods. The equipment varied in weight from 50 lbs. to 2000 lbs. The equipment layout for the three experiments is shown in Figure 3.

The general purpose bombs were placed in the same buried location for each test. Each item of equipment was hard-mounted, i.e. bolted directly to the floor, in at least one test, and isolated from the floor in various configurations for the remaining tests as shown in Table 1. Horizontal and vertical acceleration was measured on each item of equipment and on the floor near the item in every test. The isolation systems consisted of Cupmount Series Isolators, 500 Series Isolators, and neoprene pads, as shown in Figure 4. The neoprene pads were in some instances simply placed beneath the equipment while in other instances the pads were secured to the equipment and floor slab as shown in Figure 5.

RESULTS

Peak values of acceleration for each item of equipment for the various mounting configurations are tabulated in Table 2. Comparing hard-mounted and isolated acceleration values from Table 2 indicates that the Cupmount Series mounts reduced the peak acceleration in the X (horizontal) direction by about 50 percent, and reduced the peak acceleration in the Y (vertical) direction by about 30 percent. The 500 Series mounts increased the average peak acceleration in the X direction by about 20 percent while decreasing the peak acceleration in the Y direction by about 15 percent. The neoprene pads, when not attached to the floor slab, decreased the acceleration in the X direction by about 15 percent, but increased the acceleration in the Y direction by about 5 percent. Also, larger displacements were seen with the unattached pads than with any other isolators. For example, Figure 6 shows an approximate 11 inch rigid body displacement of the 1000-kw generator when it was placed on two layers (about 1/4 inch thick) of neoprene pads. The neoprene pads, when attached to the equipment and floor as shown in Figure 5, performed very well. They reduced the peak acceleration in the X direction by about 43 percent and reduced the peak acceleration in the Y direction by about 34 percent. These numbers were very similar to those obtained using the cupmount series mounts. All of the data from the 1988 tests are given in Reference 3.

SUMMARY

Relatively high peak in-structure acceleration levels (in excess of 1,000 g's) occurred in these tests. However, relative displacements were very small and no equipment damage or personnel injuries were observed, except due to falling objects. More data are needed on equipment fragility in this very high-frequency, high-shock environment. Rigid body motions of unattached equipment and furniture can be a problem. Positive connections to the floor slab should always be required, and taller items should be prevented from overturning. The commonly used Cupmount Series isolator performed very well, and can be expected to reduce peak acceleration values by about 50% compared to a hard-mounted configuration.

ACKNOWLEDGEMENTS

This research was sponsored by the U.S. Air Force Engineering and Services Center, Tyndall AFB, FL, under the direction of LTC Bob Majka. Permission to publish this paper was granted by the Office, Chief of Engineers.

REFERENCES

1. Hyde, D.W., NATO Semihardened Facilities Full-Scale Tests (draft), U.S. Air Force Engineering and Services Center, April 1989.

2. Department of the Army Technical Manual, TM 5-855-1, Fundamentals of Protective Design for Conventional Weapons, November 1986.

3. Weathersby, J. H., Data Package for the Defense Nuclear Agency (DNA) Response of Equipment to In-Structure Shock Test, Defense Nuclear Agency, November 1988.

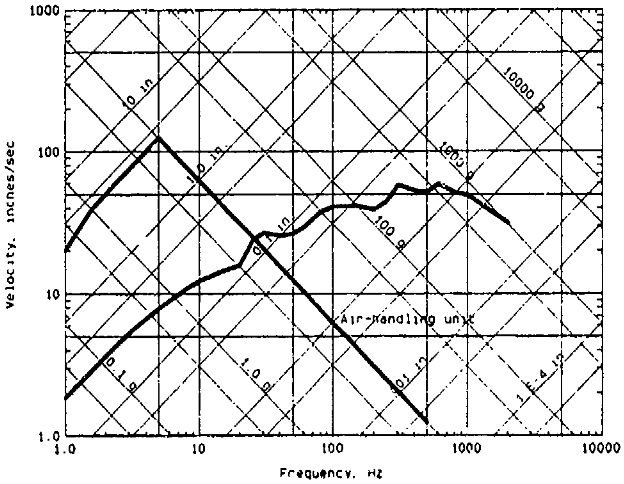

Figure 1. Shock spectra for aboveground detonation

Figure 2. Posttest view of mannequins

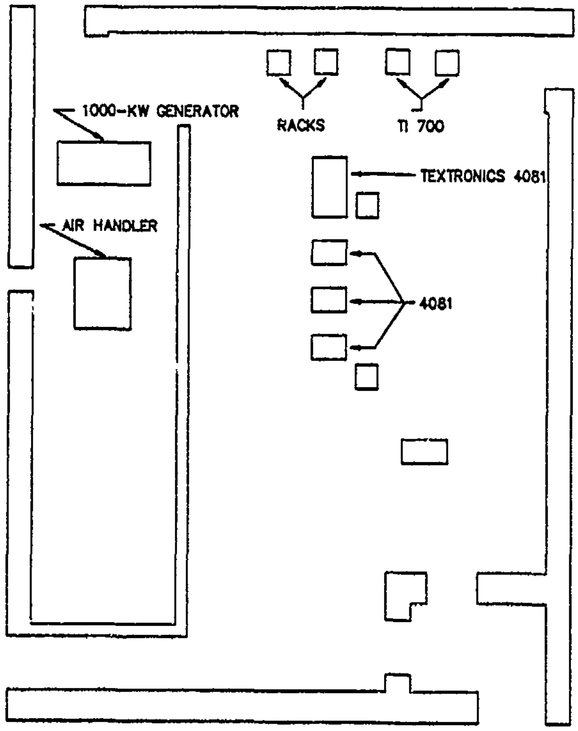

Figure 3. Equipment layout

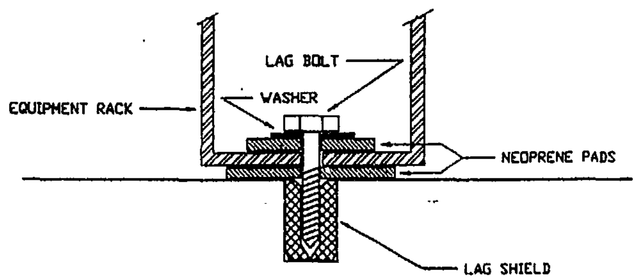

Figure 5. Attachment of neoprene pads to floor slab

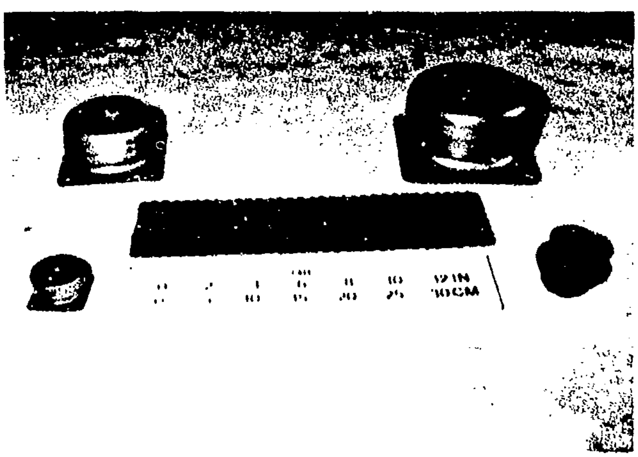

Figure 4. Isolation systems

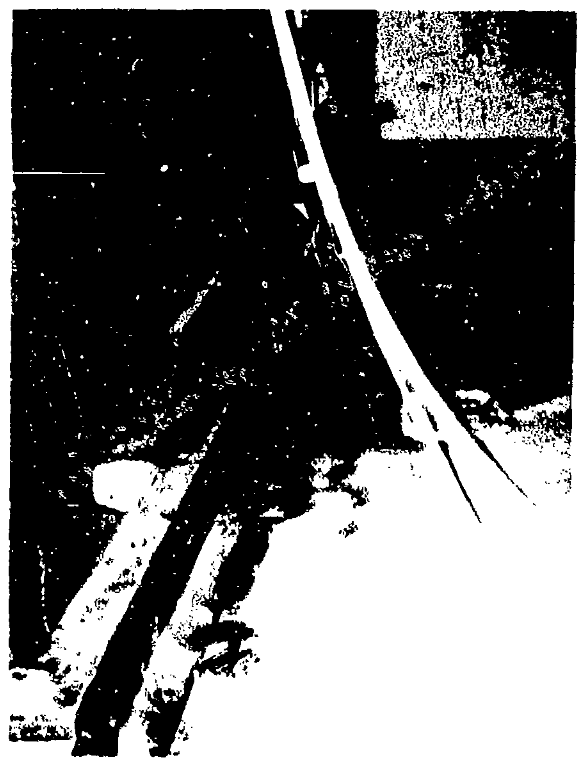

Figure 6. Postest view of 1,000 kW generator

Table 1. Shock isolation configurations

Item	Test 1	Test 2	Test 3
1,000 kW generator	Hard-mounted	Cupmount series	Neoprene pads two layers
Air-handling unit	Hard-mounted	500 series	Cupmount series
TI Silent 700 No. 1	Neoprene pads	500 series	Cupmount series
TI Silent 700 No. 2	Hard-mounted	Hard-mounted	Hard-mounted
Oscilloscope rack No. 1	500 series	Cupmount series	Neoprene pads
Oscilloscope rack No. 2	Hard-mounted	Hard-mounted	Hard-mounted
Tektronix 4081 No. 1	Neoprene pads	Hard-mounted	Cupmount series
Tektronix 4081 No. 2	Neoprene pads	Cupmount series	Hard-mounted
Tektronix 4081 No. 3	Neoprene pads	Cupmount series	Hard-mounted
Tektronix 4081 No. 4	Neoprene pads	Cupmount series	Hard-mounted

Table 2. Summary of peak acceleration data (in g's)

Item	Hard-mounted	Cupmount series	500 series	Neoprene pads
1000 kW Generator	X=32.3 Y=40.4	X=16.1 Y=30.2	----- -----	X=4.19 Y=14.1
Air-handling unit	X=9.81 Y=13.2	X=2.01 Y=3.16	X=2.35 Y=2.82	----- -----
TI Silent 700	X=26.7* Y=36.8*	X=17.0 Y=24.3	X=21.1 Y=24.3	X=22.2 Y=79.6
Oscilloscope rack	X=5.49* Y=31.8*	X=8.32 Y=21.1	X=17.2 Y=65.6	X=2.44** Y=14.9**
Tektronix 4081 No. 1	X=9.53 Y=25.9	X=2.98 Y=14.1	----- -----	X=12.8 Y=30.6
Tektronix 4081 No. 2	X=7.60 Y=24.1	X=4.98 Y=15.8	----- -----	X=43.0 Y=46.9
Tektronix 4081 No. 3	X=9.87 Y=24.5	X=3.05 Y=17.7	----- -----	X=7.86 Y=32.6
Tektronix 4081 No. 4	X=5.52 Y=22.6	X=7.48 Y=21.8	----- -----	X=7.77 Y=7.49

* Denotes average of several readings.
** Neoprene pads were attached to both the floor and the equipment rack as shown in Figure 3.
----- This type of mount not used for the item.

DYNAMIC RESPONSE OF DEEP FOUNDATIONS

R. Scott Steedman,
Engineering Department, Cambridge University, Cambridge CB2 1PZ, UK
Conrad W. Felice
Capt., USAF, 485th Civ. Eng. Sq. (USAFE), APO, NY09138-5000, USA
and
Edward S. Gaffney
Ktech Corporation, 901 Pennsylvania Ave., NE, Albuquerque, NM 87110, USA

A series of model experiments have been conducted to investigate the dynamic response of pile foundations in a blast and shock environment. The model experiments were conducted at the Cambridge Geotechnical Centrifuge facility, Cambridge UK. Two experiments were carried out on a pair of single piles and one on a group of six piles at 60g, and a fourth experiment on a pair of single piles was conducted at 1g for comparison. The model piles were hollow aluminium alloy tubes, instrumented with strain gauges in the horizontal and vertical planes to measure bending and axial strain. The test bed was a fine grained sand, saturated with water. The blast load on the foundation was provided by a 2 gm charge of pentaerythritol tetranitrate (PETN) placed below the surface at a depth of one-half of the pile length and detonated at a distance of approximately one crater radius. The paper describes the experimental techniques employed and presents results from the model tests. The results highlight the differences in pile response, particularly with depth, between the 1g and the 60g experiments and confirm the importance of correctly scaling geostatic stresses.

1.0 INTRODUCTION

Evaluation of the response of foundations to blast loads is complicated by the fact that soil properties are sensitive functions of overburden pressure. In order to properly reproduce this effect in a model one must either use a full scale model or increase the rate at which the overburden stress increases with depth. Field testing on a full scale prototype pile foundation is difficult, generally expensive and in some cases not feasible. Therefore, a database from which to develop a rational design method cannot readily be developed using field testing alone. The series of centrifuge experiments reported in this paper were undertaken to determine the feasibility of using subscale models on a centrifuge to collect valid and reliable data on the blast response of pile foundations. Discussion of the use of the geotechnical centrifuge for dynamic modelling and on the necessary scaling relations for 1g and for centrifuge modelling may be found in the literature, Schofield (1981), Schofield and Steedman (1988).

The objective of these experiments was to show that the centrifuge is an appropriate means to gain an understanding of pile foundation response under blast loading. The design parameters were selected to be representative of a typical hollow reinforced concrete pile in a sand foundation but not a precise model of a specific prototype. This approach was selected because the authors believed that there was more to be learned at this stage from a study of a generic problem which identified phenomena, rather than from models which attempted to reproduce details of a site specific problem. Hence the results are more readily extended to other systems.

The paper describes the design and instrumentation of the model piles, and aspects of model construction. Results are presented in terms of deformations and bending moments as a function of length for two isolated single piles fixed at ground level. The cratering and ground motion data collected are presented in a companion paper, Gaffney et al. (1989). Results from the initial experiments were reported by Felice et al. (1988).

2.0 EXPERIMENTAL PROGRAMME

2.1 Model charge

Four experiments were conducted on single piles and a line of piles forming a pile group as described above. The charge was selected to simulate the detonation of a 1000 lb conventional munition. At 1/60th scale, 2 gm of explosive was required (scaling relations are shown in Table 1). This was accomplished by packing 1.6 gm PETN inside a plastic sphere. The remaining 0.2 gm was made up by the detonator. The average density of the PETN powder was 0.9 gm/cm^3. The detonator, a Reynolds RP-80 exploding bridge wire was placed in the sphere to initiate the explosion from the centre. The charge was coated with a thin film of epoxy to protect it against moisture.

2.2 Model piles

The model piles were constructed from 6.35 mm outer diameter aluminium alloy (dural) tube with an inner diameter of 5.0 mm. Prior to instrumenting, the piles were turned down to an outer diameter of 5.8 mm. Each pile extended 147 mm below its top fixity. The elastic Young's modulus and density of dural are 69 x 10^3 MPa and 2.83 gm/cm^3, respectively. The manufacturer's specification set the elastic limit as 255 MPa and the minimum tensile strength as 310 MPa. These data give a model bending stiffness of EI = 1.72 Nm^2 and a fully plastic moment capacity of Mp = 3.625 Nm. From the scaling relations, the equivalent prototype pile is seen to be 8.82 m in length, with a bending stiffness of 1.72×60^4 = 22.3 MNm^2, and a plastic moment capacity of 3.625×60^3 = 0.783 MNm. The head of each pile was fixed into a steel gantry at a range of either 125 mm (7.5 m prototype) or 158 mm (9.5 m prototype), as shown in Fig. 1.

Selected piles and the ground beam were instrumented with full bridge strain gauge circuits to record bending or axial strain. To protect the gauges and wiring from moisture, they were coated with a polyurethane varnish and covered with a heat shrink plastic tubing.

2.3 Model construction and layout

Fig. 1 shows the containment system used for the latter two of the four experiments. Two circular tubs were used, one sitting on a rubber mat inside the other, with an air gap of approximately 24 mm separating them around the perimeter. This was a development from the containment used for the earlier experiments (RSS.130 and 131, which used only a single tub) following concerns raised over the level of safety that a single tub provided.

Breeze block (a porous concrete patio block) was placed at the base of the model to simulate an underlying bedrock. The model was then constructed by pouring a uniform dry sand layer to a depth of 150 mm (9 m at prototype scale). The sand used in the model was a Leighton Buzzard 100/200 sand with a nominal grain size of 0.12 mm and specific gravity of 2.65. 100/200 denote the British Standard sieve sizes through which the sand should pass/be retained.

Prior to the sand-pouring the piles, which had been clamped at the top into a heavy steel gantry, were fixed in position by locating the gantry onto the model chamber. In each case the gantry spanned across the tub, and was securely bolted to the stiff rim of the outer tub. For the pair of piles experiments, one pile was positioned to be just inside the crater with the second near the crater lip, about 90° further round the crater perimeter. A small clearance existed between the piles and the breeze block beneath to avoid unpredictable axial bearing forces in the piles.

Sand was rained from a hopper suspended above the tub using a constant height of drop. Pouring was interrupted to allow the placing of transducers in the free field (see companion paper for a description and discussion of the free field instrumentation). The sand was levelled and the model saturated by sealing the chamber with a heavy lid and drawing in a calculated volume of water under vacuum. In the second series of experiments, RSS.140 and 141, CO_2 was flushed through the chamber prior to the introduction of water.

For all four experiments, the charge was placed at a depth of 74 mm (half the pile length) immediately prior to mounting the package on the centrifuge swinging platform. A short thin walled brass tube which had been placed in the sand bed during sand pouring to mark the location of the charge was excavated to the correct depth where the charge was placed at the bottom of the hole. The brass tube was then backfilled with the excavated sand and then extracted by gently vibrating the tube and pulling it upwards. The water level inside the tube was maintained at a constant level during the process.

The completed model was then mounted on the centrifuge and accelerated to 60 g. The FS-10 firing control unit, which had also been mounted on the centrifuge, was triggered remotely from the control room.

The procedure for the 1 g experiment was identical in all respects except that it was detonated on the laboratory floor instead of on the centrifuge. Care was taken to ensure that the model was level and that the ground water level was exactly at the ground surface.

Table 2 summarises the model parameters for each of the model tests.

3.0 RESULTS AND DISCUSSION

3.1 Bending moments

All results are plotted in terms of prototype dimensions. Fig. 2 shows time histories of the development of bending moment from a typical isolated single pile in a 60g experiment. A rapid build-up of bending moment is followed by a slower decay, with the duration of plastic straining being about 0.6 seconds (10 msec 'real time' in the model). The records, which are from strain gauge bridges at different depths on the same pile, show strongly consistent data, and this enables detailed consideration to be given to the profile of bending moment with time along the pile.

In contrast, Fig. 3 shows the equivalent data from a 1g experiment. There is a longer period at or near the peak bending strain at each depth, and a less rapid build-up to the peak strain. The magnitudes of peak strain are comparable between the 1g and the 60g model as would be expected since in both cases peak strains are limited by the plastic moment capacity of the pile.

It is clear from the plots of displacement profile shown below that all piles developed plastic hinges and failed, with large lateral permanent displacements. The peak bending strains recorded by the strain gauges are large and in excess of the manufacturer's stated elastic range. On a few occasions the local bending strains were so large (2-3%) that the gauges broke down and the signal from that circuit was lost. Clearly as strains in the outer fibres of the dural piles exceed a yield point the relationship between moment and measured bending strain is no longer linear. Thus although peak moments are of great interest, the development of moment as a function of time and depth may provide more significant clues to the reponse of the pile from an analytical view-point. Furthermore, in the design of the model piles correct scaling of the bending stiffness was chosen at the expense of the correct yield characteristics.

Fig. 4 compares the development of bending moment with time from an isolated single pile in a 60g experiment to the development of moment in a 1g experiment.

Time intervals have been chosen to be shortly after the first significant build-up of strain and then at equal time intervals of 46.9 msec until the peak strain was reached, or shortly thereafter. A 'best fit' fourth order polynomial has been drawn through the peak data of both 1g and 60g experiments.

One clear feature of the data is the marked similarity between the strain distributions at the early (t1) stage, in contrast to the later build-up towards a peak. At the t2 or t3 stage the peak moment is clearly at a shallower depth in the 60g experiment than in the 1g experiment (which consistently shows a peak near shot depth). The 60g model, however, has a distribution biased upwards, towards the ground surface.

This is likely to be due to the increased stiffness of the sand bed in the 60g experiment in comparison to the 1g model (a factor of 8 under static load conditions). However, this factor may have been considerably reduced around the time of the maximum moments (t2 or t3 in Fig. 4) because of the large negative pore pressures in the 1g experiment which followed the peak pore pressure 'wave'. In the 60g experiments, the pore pressure wave lasted longer and decayed considerably more slowly.

The early time data of bending strains is enlarged in Fig. 5 together with a polynomial which follows the general trend of the data. At this time in both the 1g and the 60g experiments, the pore pressure around the pile was approaching a peak, with a corresponding reduction in stiffness.

The polynomial in Fig. 5 was used to deduce the general trend of the pressure distribution, by differentiation. A check was made, by integrating the polynomial, that the slope at the pile top and the displacement at the pile bottom were minimised or zero. It is clear that the trend of the pressure distribution at this time is as shown in Fig. 6, in which a high load at the pile top decays to near zero around the central portion of the pile together with some restraint near the pile bottom.

Preliminary conclusions are that the central portion of the pile moves with the liquefied soil, without load or resistance. Near the top of the pile, the soil is being driven past the stationary pile head, imposing very substantial loading and this is the most likely location of the first plastic hinge.

3.2 Displacements

Fig. 7 shows the profile of displacement with depth for piles (1) and (2) (range 7.5m and 9.5m) in both a 1g (141) and 60g (140) experiment. Measurements were made using an image analyser at AFWL.

The initial slopes of the piles are very consistent, but the increased restraint caused by the higher overburden stresses at the base of the 60g model limits the outward movement of these piles. Clearly these displacements are much more closely linked to the distribution of soil strain in the sand beds, which is discussed in more detail by Gaffney et al. (1989).

The depth of the central plastic hinge is less in the 60g than in the 1g experiments, which is in agreement with the observations of bending strain in Fig. 4.

A critical element in the prediction of the range of damage to piles in the field is the nature and magnitude of the pore pressure wave. The fast decay of the pore pressure wave in the 1g model is likely to be due to the strong dilation front which followed immediately behind. Although at high g a dilation front will recover the full field (or prototype) strength in the soil, at 1g the strength of the sand is small and large strains can take place.

The high g model can correctly scale the pattern of ground strain and the character of a pore pressure wave, whereas the response of a pile in a 1g experiment, close in to the charge, will be determined by the strength of the pile and the proximity of the charge.

4.0 Conclusions

4.1 The time histories of bending strain in model tests have provided valuable data towards the development of analytical techniques. In particular, it is clear that a data-base of soil-structure interaction under blast loading can be developed using centrifuge modelling.

4.2 In particular, the build-up towards a peak strain is initiated as the wave of pore pressure arrives at the pile, softening the soil around the pile. High loading is observed near the pile top with a minimum of load around the central section. The peak strain is reached as the pore pressure wave decays, both radially and with depth. Larger bending strains are then invoked as the deeper soil consolidates more rapidly and provides restraint against lateral movement.

5.0 Acknowledgements

The work described in this paper was supported by the US Air Force Weapons Laboratory, (AFWL/NTESG), Kirtland AFB, NM 87117-6008.

5.0 References

Felice, C.W., Steedman, R.S. and Gaffney, E.S. (1988). Centrifuge models of ple response in a blast and shock environment, Int Conf Centrifuge Modelling, 'Centrifuge 88', Paris.

Gaffney, E.S., Felice, C.W. and Steedman, R.S. (1989). Cratering by buried charges in wet media : comparison of centrifuge and field events, Symp on Interaction Non-nuclear Munitions with Structures, Panama City, Florida.

Schofield, A.N. (1981). Dynamic and earthquake geotechnical centrifuge modelling, Proc Int Conf Recent Advances in Geotech Earthquake Eng Soil Dynamics, Vol.3 1081-1100, Univ Missouri Rolla.

Schofield, A.N. and Steedman, R.S. (1988). Recent development of dynamic model testing in geotechnical engineering. Proc IX World Conf Earthquake Engineering, Tokyo.

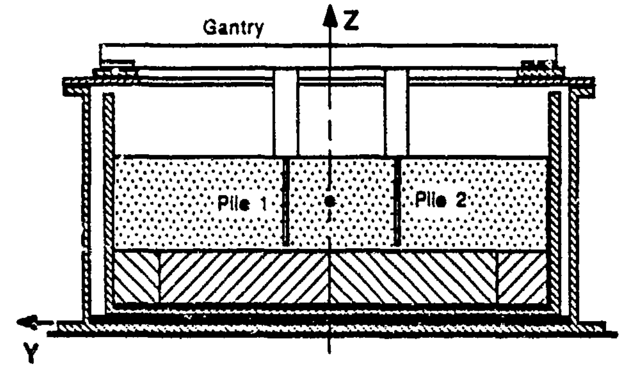

ELEVATION THROUGH TUB, Y-Z PLANE

Table 1

Quantity	Ratio of model to prototype
Length	1/n
Velocity	1
Acceleration	n
Force	$1/n^2$
Stress	1
Energy	$1/n^3$
Frequency	n
Time	1/n for inertial events $1/n^2$ for diffusion

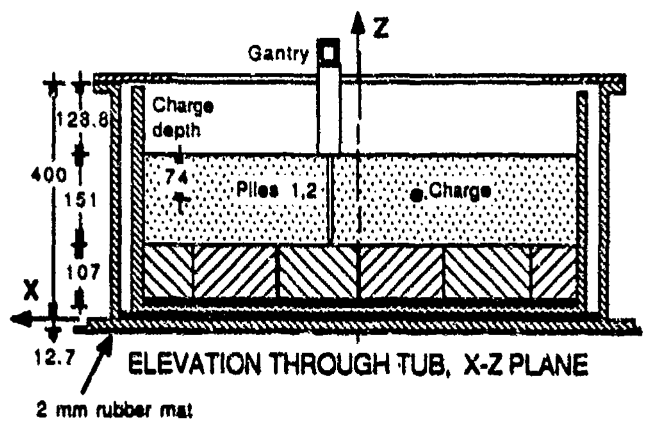

Table 2

Exp't	piles	sand mass kg	sand volume litres	void ratio	relative density	φ
RSS.130	2	124.5	84.6	0.8	60%	60
RSS.131	6(line)	126.5	86.4	0.82	55%	60
RSS.140	2	109.5	71.47	0.74	75%	60
RSS.141	2	111.0	71.97	0.72	82%	1

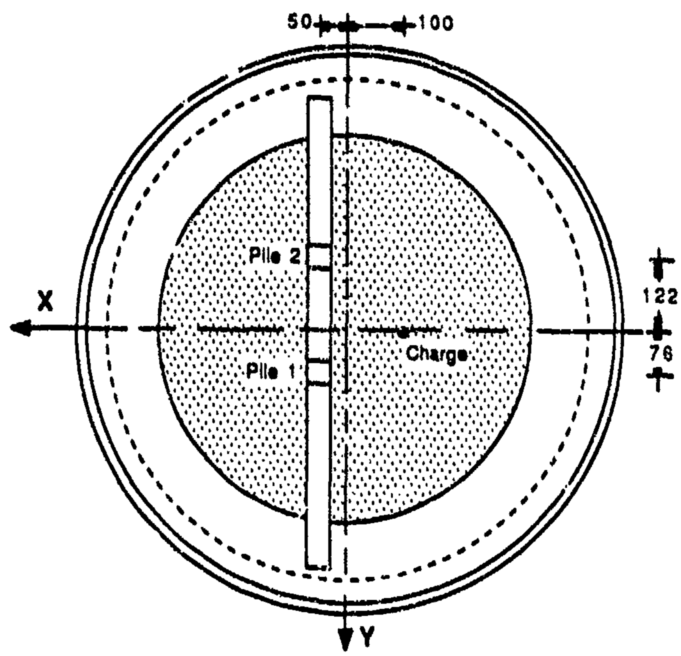

PLAN VIEW OF MODEL RSS.140, LOOKING ALONG Z AXIS

Fig.1 Plan and cross-sections through the 60g centrifuge model test RSS.140

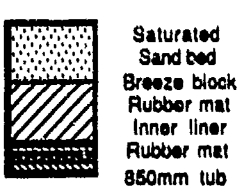

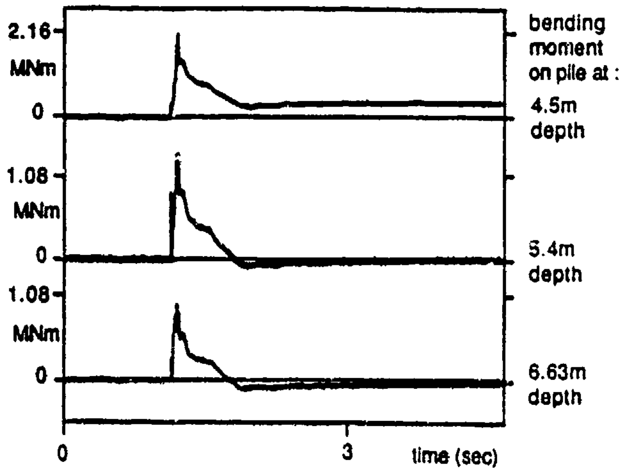

Fig.2 Bending moment recorded on Pile 1, model RSS.140 (60g)

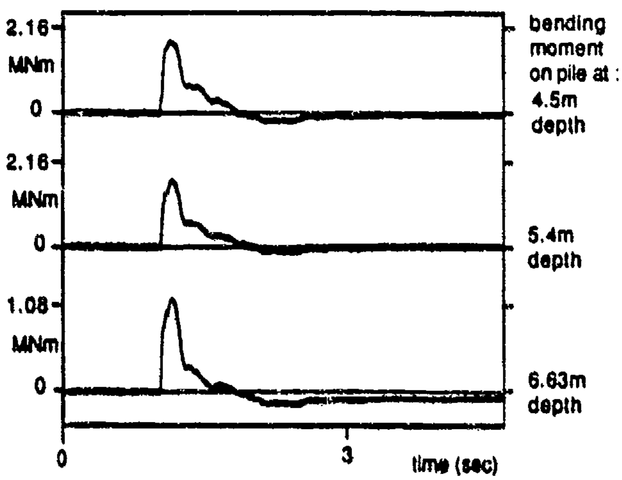

Fig.3 Bending moment recorded on Pile 1, model RSS.141 (1g)

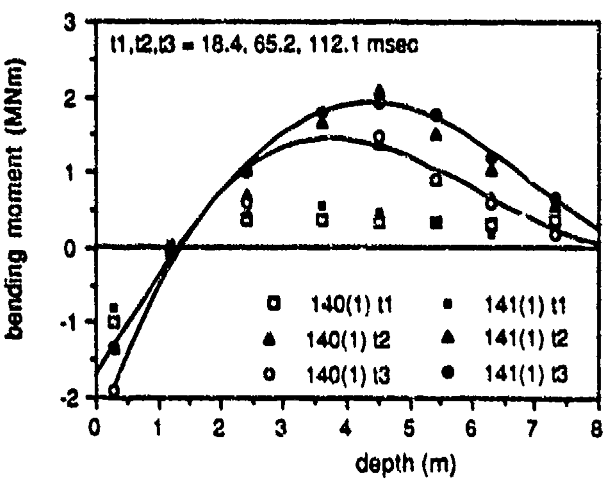

Fig.4 Comparison of 1g and 60g single pile data : piles inside crater

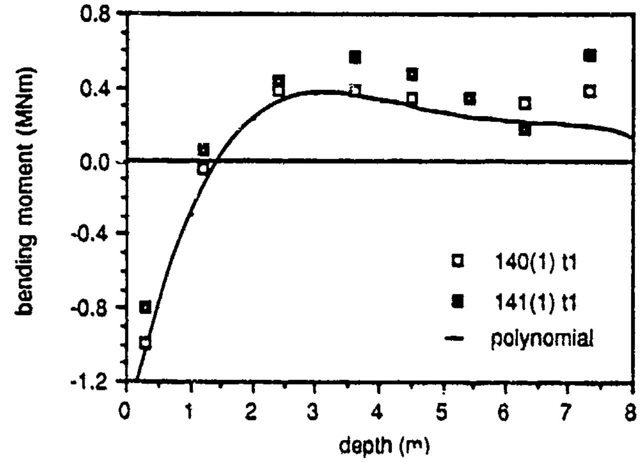

Fig.5 Fourth order polynomial through early time data

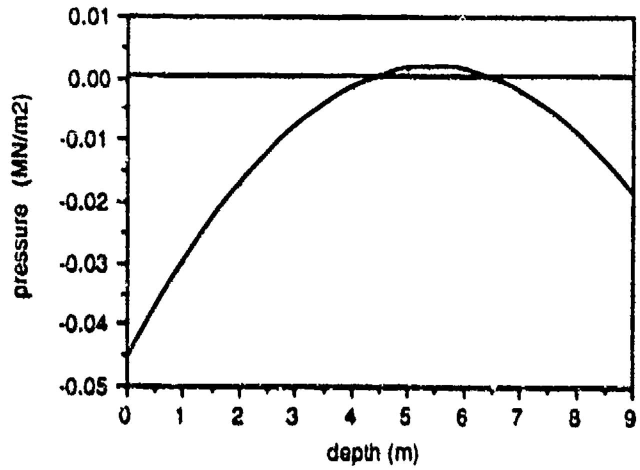

Fig.6 Interpreted pressure distribution

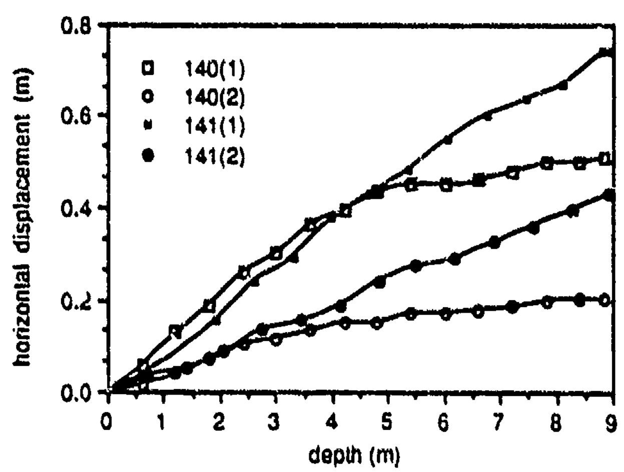

Fig.7 A comparison of pile deflections from 60g and 1g experiments

LIST OF ATTENDEES

Satish Abrol
HQ USAF/LEEE, #516, Bolling AFB
Washington, D. C. 20332-5040

Mark A. Amend
AD/ENYW
Eglin AFB, Florida 32542-5000

Ali Amini
UTD Inc.
8560 Cinderbed Road, Suite 1300
P.O. Box 8560
Newington, Virginia 22122

Kolodkin Arkady
7 Hasadna Street
Industrial Center Holon 58814
P.O.B. 32 AZOR 58190

Gerald Ast
SIGMA - Beratende Ingenieure
Auerstr. 1, 7500 Karlsruhe
WEST GERMANY

Charles Baker
Lawrence Livermore Laboratory
P. O. Box 808 L-606
Livermore, California 94550

Quentin A. Baker
Wilfred Baker Engineering
P.O. Box 6477
San Antonio, Texas 78209

Wilfred Baker
Wilfred Baker Engineering
P.O. Box 6477
San Antonio, Texas 78209

Khosrow Bakhtar
The Earth Technology Corp. (Western)
100 West Broadway, Suite 5000
Long Beach, California 90807

George Y. Baladi
AFWL/NTE
Kirtland AFB, New Mexico 87117-6008

Peter Balazs
FORTF, Research Department
63189 Eskilstuna
SWEDEN

Donald B. Baldwin
Sverdrup Corporation
Embassy Task Group
1500 Wilson Blvd., Suite 900
Arlington, Virginia 22209-2454

Athanassios Ballis
MOD Breece/Hellenic Air Force
AF HQS - NATO Infractructure Dept.
Mesogion Street
Athens - GREECE

Jimmy Balsara
USAE Waterways Experiment Station
P.O. Box 631
Vicksburg, Mississippi 39180

Darrell Barker
Mason & Hanger - Silas Mason Co., Inc.
P.O. Box 30020
Amarillo, Texas 79177

James J. Bartis, Jr.
Ground & Weapons Safety
103D TFG
Bradley ANG Base
East Granby, Connecticut 06026-5000

Martin Becker
Weidleplan Consulting
Maybachstrasse 33
D 7000 Stuttgart 30
WEST GERMANY

Greg Bessette
MSD/ENYW
Eglin AFB, Florida 32542

Brian Bidwell
Mason & Hanger - Silas Mason Co., Inc.
P.O. Box 30020, Pantex Plant
Amarillo, Texas 79177

Scott E. Blouin
Applied Research Associates, Inc.
3202 Wisconsin Avenue
Vicksburg, Mississippi 39180

Wayne R. Boeck
ATTN: CEMIO-EDST
Corp of Engineers
215 N 17th Street
Omaha, Nebraska 68102

Patricia Moseley Bowles
6220 Culebra Road
San Antonio, Texas 78284

Steven Boyce
AFOSR/NA Building 410
Bolling AFB, D.C. 20332-6448

Jimmie L. Bratton
Applied Research Associates Inc.
4300 San Mateo Blvd. NE
Suite B380
Albuquerque, New Mexico 87110

Aubrey C. Brock
Shriver & Holland Associates
355 West Freemason Street
Norfolk, Virginia 23510

Larry L. Brown
University of Denver
Denver Research Institute
University Park 2050 E. Iliff
Denver, Colorado 80208

Walter C. Buchholtz
Air Force Engineer and Services Center
Tyndall AFB, Florida 32403

Edward H. Bultmann, Jr
UNM/NMERI
Campus Box 25
Albuquerque, New Mexico 87131

D. N. Burgess
The BDM Corporation
PO Box 1206
Redland, California 92373

Lou Caccia
Naval Surface Warfare Center
Code G13
Dahlgren, Virginia 22448

Delmar Calhoun
New Mexico Engineering Research Inst.
Campus Post Office Box 25
Albuquerque, New Mexico 87131

Chester E. Canada
DoD Explosives Safety Board
Eisenhauer Avenue
Alexandria, Virginia 22331-0600

James D. Cargile
CEWES-SD-O
USAE Waterways Experiment Station
P.O. Box 631
Vicksburg, Mississippi 39181-0631

Martin Carlsson
TYRENS
Esplandaden 3A
P.O. Box 512
S-17229 Sundbyberg
SWEDEN

Thomas P. Carroll
T. Carroll Associates, Inc.
6917 Arlington Road #303
Bethesda, Maryland 20814

W. O. Carter
Department of Civil Engineering
FAMU/FSU College of Engineering
PO Box 2175
Tallahassee, Florida 32316-2175

Mel Castillo
General Dynamics-Convair
P.O. Box 85357
Mail Zone 16-6150
San Diego, California 92138

Ching S. Chang
Department of Civil Engineering
University of Massachusetts
Amherst, Massachusetts 01003

Wayne A. Charlie
Geotechnical Engineering Program
Department of Civil Engineering
Colorado State University
Fort Collins, Colorado 80523

Hung-Liang Chen
Department of Civil Engineering
Northwestern University
Evanston, Illinois 60208

Anthony J. Cichocki, Jr.
103D TFG
Bradley ANG Base
East Granby, Connecticut 06026-5000

K. J. Claber
62 CRE Works, Chilwell Station
Beeston, Nottingham NG95HB
UNITED KINGDOM

Greg Clemens
USAE Waterways Experiment Station
P.O. Box 631
Vicksburg, Mississippi 39180

Lily C. Clouston
University of Florida
Eglin Graduate Center
P.O. Box 1918
Eglin AFB, Florida 32542

Carlos Coe
BDM Corporation
7910 Jones Branch Drive
McLean, Virginia 22102

John Collins
AFATL/SAA
Eglin AFB, Florida 32542

Ken Conley
Naval Surfaces Warfare Center
Code G13
Dahlgren, Virginia 22448

Bob Courtier
WS Atkins & Partners
Woodcote Grove Ashley Road
Epsom, Surrey KT18 5BW
UNITED KINGDOM

George Crews
AFATL/SAA
Eglin AFB, Florida 32542

Franc Croch
(no address available)

Gerald P. D'Arcy
Applied Research Associates, Inc.
P.O. Box 40128
Tyndall AFB, Florida 32403

William C. Dass
Applied Research Associates, Inc.
P.O. Box 40128
Tyndall AFB, Florida 32403

Lindell A. Davidson
Naval Facility Engineering Command
Code 403 Building 212
Washington Navy Yard
Washington, D.C. 20374-2121

Michael C. R. Davies
University of Wales
College of Cardiff
School of Engineering
Newport Road
Cardiff CF2 1TA
UNITED KINGDOM

Roger DeBrabander
Chief, Belgian Military Const. Agency
Quartier Rein Elisabeth-Bloc 5-Rue d'Evere
BELGUIM 1140 Evere - Brussels

Chandra Dibankar
University of Minnesota
Dept. of Civil & Mineral Engineering
Minneapolis, Minnesota 55455-0220

Charles D. Dilts
McDonnell Douglas Astronautics Co.
701 Columbia Blvd.
Titusville, Florida 32780

Kathy Douglas
Fixed TGT Technical Oversight Center
MSD/XRF
Eglin AFB, Florida 32542

Clifford H. Doyle
US Army Tech Center for Explosive Safety
Attn: SMCAC-ESP
Savanna, Illinois 61074-9639

James L. Drake
Applied Research Associates, Inc.
3202 Wisconsin Avenue
Vicksburg, Mississippi 39180

Richard Drake
Fluor Daniel, Inc.
3333 Michelson Drive
Irvine, California 92730

Ron Earyes
US Army Corps of Engineers
CEEC-EM
20 Massachusetts Avenue NW
Washington, D.C. 20314-1000

David Eldar
KKL St. No. 34, GEDERA
ISRAEL

Russell H. England
California Research & Technology
20943 Devonshire Street
Chatsworth, California 91311

Edward D. Esparza
Southwest Research Institute
P.O. Drawer 28510
San Antonio, Texas 78284

Jan Eversen
Joe D. Glenn & Associates, Inc.
PO Box 12154
Norfolk, Virginia 23502

Reuben Eytan
Eytan Building Design Ltd.
44 Ugarit Street
69016 Tel Aviv
ISRAEL

Richard H. Fashbaugh
Mechanical Engineering Department
University of Nevada at Reno
Reno, Nevada 89557

O. Favarger
Gruppe fur Rustungsdienste
Fachabtlg. Ballistik und
Waffen/Kampffahrzg-Prufung
General Herzog Haus
3602 Thun
SWITZERLAND

Clarence J. Fennell
Structural Response Section
Box 1266, PSC West
Kirtland AFB, New Mexico 87117

Marty Fertal
The BDM Corporation
7915 Jones Branch Drive
McLean, Virginia 22102

Richard Forsen
Swedish Defence Research Establishment
(FOA)
P.O. Box 557
S-74725 Tumba
SWEDEN

Eugene R. Fosness
WL/NTESR
Kirtland AFB, New Mexico 87117-6008

Eugene L. Foster
8560 Cinderbed Road, Suite 1300
Newington, Virginia 22122

Mavis Foster
8560 Cinderbed Road, Suite 1300
Newington, Virginia 22122

Richard J. Fragaszy
Geotechnical & Transportation Engr. Section
Department of Civil & Environment Engr.
Washington State University
Pullman, Washington 99164-2910

Robert Frank
Applied Research Associates, Inc.
Suite 200
6404 Falls of Neuse Road
Raleigh, North Carolina 27615

H. A. Franklin
Bechtel National Inc.
P.O. Box 3965 (50/17/B54)
San Francisco, California 94119

K.-L. Fricke
KONSTRUKTIV - Ingenieurburo
Kopenhagener Str 25
3000 Hannover
WEST GERMANY

Kazuo Fujimoto
Protective Structures Research Section
1st Div., 4th Research Center of Technical Research and Dev. Inst.
Japan Defense Agecy
Fuchinobe, Sagamihara, Kanagawa 229
JAPAN

Edward S. Gaffney
Ktech Corporation
901 Pennsylvania NE
Albuquerque, New Mexico 87110

James B. Gaines, Jr.
Middle East/Africa Projects Office
US Army Corps of Engineers
P.O. Box 2250
Winchester, Virginia 22601-1450

William H. Gaube
215 North 17th Street
Attn: CEMRO-ED-SH
Omaha, Nebraska 68102-4978

Eberhard Gerth
Luwa Ltd., U.S. Office
Defense Products Division
Suite 230
4400 East West Highway
Bethesda, Maryland 20814

John J. Gill
Geologic Response Section
AFWL/NTESG
Kirtland AFB, New Mexico 87117

Robert C. Gilliat
The Old Post Office
Lee, Ilfra Combe
Devon EX34 8LR
UNITED KINGDOM

Ferdinand Glaser
GE Federal Office for Military Technology and Procurement, Test Center 91
4470 Meppen
WEST GERMANY

Max Gloor
Heierli, AG Ingenieurbuero
Culmannstr 56, Postfach 248
CH-8033 Zurich
SWITZERLAND

Kent Goering
Defence Nuclear Agency
Headquarters
Washington, D.C. 20305

Paul W. Graham
USAE Waterways Experiment Station
P.O. Box 631
Vicksburg, Mississippi 39180

Dan Granados
AF Weapons Laboratory/NTSM
Kirtland AFB, New Mexico 87117-6008

Curt Granrud
Granruds
P.O. Box 571
651 13 Karlstad
54/156850
SWEDEN

Glen Green
Protective Door Industries
2250 Western Avenue
Park Forest, Illinois 60466-1293

Gerhard H. Guerke
Fraunhofer Institut fur Kurzzeitdynamik
Ernst Mach Institut
Eckerstr 4 7800 Freiburg
WEST GERMANY

H.-J. Hader
Basler und Partner AG
Ingenieurunternehmen
Zollikerstrasse 65
8702 Zollikon
SWITZERLAND

Paul F. Haggard
Mason and Hanger Engineering, Inc.
1500 Leestown Road
Lexington, Kentucky 40511-2058

Carl Halsey
Naval Weapons Center
Code 3269
China Lake, California 93555

Juerg Hasler
Luwa Ltd.
CH-8152 Blattbrugg Kanalstrasse 5
SWITZERLAND

John R. Hayes, Jr.
U.S. Army Construction Engineering
Research Laboratory
(CECER-EME)
P.O. Box 4005
Champaign, Illinois 61820-1305

Werner Heierli
Heierli, Ingenieurburo AG
Culmannstr 56, Postfach 248
CH-8033 Zurich
SWITZERLAND

Robert W. Henny
AFWL/NTE
Kirtland AFB, New Mexico 87117

Willi Herrmann
Wehrbereichskommando V
Abteilung Infrastruktur
Nurnberger Str 184
7000 Stuttgart
WEST GERMANY

Cornelius J. Higgins
Applied Research Associates, Inc.
4300 San Mateo Blvd. NE Suite 220
Albuquerque, New Mexico 87110

Eve E. Hinman
Weidlinger Associates
333 Seventh Avenue
New York, New York 10001

Lim Chee Hiong
Lands & Estates Organisation
5th Storey, Leo Building
Paya Lebar Airport
SINGAPORE 1953

K.-Q. Ho
Housing & Development Board
3451 Jalan Bukit Merah
HDB Centre
SINGAPORE 0315

Brian Hobbs
Department of Civil and Structural
Engineering
The University, Mappin Street
Sheffield, S1 3JD
UNITED KINGDOM

Erich Holthauser
BTE Bavaria T.O.R. Engr. GmpH
Niederlassung Koln
5000 Koln 41
Eupener Str. 161
WEST GERMANY

Douglas Honegger
EQE Engineering
3150 Bristol Street, Suite 350
Costa Mesa, California 92626

Goh Song How
Lands & Estates Organisation
5th Storey, Leo Building
Paya Lebar Airport
SINGAPORE 1953

John W. Howard
Lorron Corporation
44 Mall Road, Suite 203
Burlington, Massachussetts 01803

Klaus Huesing
WTD 91 - 443
Schiessplartz
4470 Meppen/Ems
WEST GERMANY

Wes Hughson
MSD/ENYW
Eglin AFB, Florida 32542

David A. Hulburt
Hercules Incorporated
P.O. Box 210
Rocket Center, West Virginia 26726

David W. Hyde
USAE Waterways Experiment Station
P.O. Box 631
Vicksburg, Mississippi 39180-0631

M.J. Iremonger
Royal Military College of Science
Shrivenham, Swindon SN6 8LA
UNITED KINGDOM

Makren Jaber
GEO Services
5950 Liveoak Pkwy, Suite 330
Norcross, Georgia 30093

Edward Jacobs
Integrated System Analysts, Inc.
7 Buckingham Way
Shalimar, Florida 32579

Bengt Jakstad
JP Sheltec AB
Box 1163
141 24 Huddinge
SWEDEN

David A. Jenkins
University of Florida
College of Engineering Sciences
Gainesville, Florida 32611

Arnfinn Jenssen
Norwegian Defence Construction Serv.
Oslo Mil/Akershus
N-0015 Oslo 1
NORWAY

Elisabeth Jerome
Sverdrup Technology Inc.
TEAS Group
P.O. Box 1935
Eglin AFB, Florida 32542

Kjell Jonassen
Norwegian Defence Construction Serv.
Oslo Mil/Akershus
N-0015 Oslo 1
NORWAY

Torbjorn Jonasson
Swedish Defence Research Establishment (FOA)
P.O. Box 557
S-74725 Tumba
SWEDEN

Alex Katzaf
Air Force Engineering & Services Center
Tyndall AFB, Florida 32403

Ronald Kaufmann
Amt fur Studien und Ubengen der Bundeswehr
Bereich Sonderaufgaben Infrastruktur
Friedrich-Ebert-Str. 72
5060 Bergisch Gladbach 1
WEST GERMANY

Leon M. Keer
Northwestern University
Department of Civil Engineering
Evanston, Illinois 60208

Melvin H. Keith
Code 39104
Naval Weapons Center
China Lake, California 93555-6001

Robert W. Kelley
US Army Corps of Engineers
Omaha District
215 N. 17th Street
Omaha, Nebraska 68102-4978

L. J. Kennedy
Rarde Barrak Road
Christchurch
Dorset BH 23 2BB
UNITED KINGDOM

Roy G. Kennington
Commander
Air Force Engineering & Services Center
Tyndall AFB, Florida 32403

Sam Kiger
USAE Waterways Experiment Station
Box 631
Vicksburg, Mississippi 39180

Martin Koller
Glauser Studer Stussi Engineers, Inc.
Witikonerstrasse 15
CH-8032 Zurich
SWITZERLAND

Diethard Konke
Universitat der Bundeswehr Munchen
Institut fur Mechanik und Statik
Werner-Heisenberg-WEG 39
8014 Neubiberg, BRD
WEST GERMANY

David Kossover
Amman & Whitney
Ninety-Six Marton Street
New York, New York 10014-3309

Fred Krach
Monsanto Research Corp.
P.O. Box 32
Miamisburg, Ohio 45342

Dusan Krajcinovic
CEMM Department mc 246
University of Illinois at Chicago
P.O. Box 4348
Chicago, Illinois 60680

Dieter Kraus
Lehrstuhl fur Massivbau,
Universitat Der Bundeswehr Munchen
8014 Neubiberg
Werner Heisenberg Weg 39
8014 Neubiberg
WEST GERMANY

T. Krauthammer
University of Minnesota
Department of Civil and Mineral Engineering
Minneapolis, Minnesota 55455-0220

Richard L. Kresge
ADWC/SEWE
Tyndall AFB, Florida 32403-5000

Martin Kropatscheck
Amt fur Studien und Ubungen
der Bundeswehr
Bereich Sonderaufgaben-Infrastruktur
Friedrich-Ebert-Str 72
5060 Bergisch Gladbach 1
WEST GERMANY

Malthias Kruse
E. Basler & Partners
Zollikerstr. 65
CH 8702 Zollikon
SWITZERLAND

Stephen Kuennen
USAF Engineering & Services Lab
RDCM
Tyndall AFB, Florida 32403-6001

Paul LaHoud
P.O. Box 1600 HNDED-CS
Huntsville, Alabama 35807

Patrick J. Lama
Mason IND/ASHRAE
350 Rabno Drive
Hauppauge, L.I., New York 11787

Samuel C. Lambert
Chief Scientist
Air Force Armament Laboratory (AFSC)
Eglin AFB, Florida 32542

Helge Langberg
Norwegian Defence Research Est.
Div. for Weapons & Equipment
P.O. Box 25
N-2007 Kjeller
NORWAY

Helga Langheim
Ernst-Mach-Institut
Eckerstr
7800 Freiburg
WEST GERMANY

Magnus Langseth
Div. of Structural Engineering
The Norwegian Institute of Technology
7034 Trondheim
NORWAY

Pam Langston
GEO Services
3950 Liveoak Pkwy, Suite 330
Norcross, Georgia 30093

Darell J. Lawver
Department of Civil Engineering
U S Air Force Academy Qtrs 4209A
USAF Academy, Colorado 80840

W. Douglas Lewis
Dept. of Navy, Atlantic Division
Naval Facilities Engineering Command
Code 402
Norfolk, Virginia 23511-6287

Pat Lindsey
US Army Corps of Engineers
215 North 17th Street
Omaha, Nebraska 68102-4978

Frank Maestas
Applied Research Associate, Inc.
4300 San Mateo Blvd., NE, Suite 220
Albuquerque, New Mexico 87110

Robert J. Majka
HQ AF Engineering & Services Center
Tyndall AFB, Florida 32403-6001

Mark Malone
NATO Infrastructure Tech. Div.
HQ USAFE/DENT
APO New York 09094

Lawrence E. Malvern
Department of Aerospace Engineering
Mechanics, and Engineering Science
University of Florida
Gainesville, Florida 32611

Kirk A. Marchand
Southwest Research Institute
P.O. Drawer 28510
San Antonio, Texas 78284

Larry Mars
Sverdrup Technology
Bldg. 9800, John C. Stennis Space Center
Stennis Space Center, Mississippi 39529

Audrey Martinez
USAF Weapons Laboratory
WL/NTESE
Kirtland AFB, New Mexico 87111

Ronald Massa
Lorron Corporation
44 Mall Road
Suite 203
Burlington, Massachussetts 01803

H.S. McDevitt, Jr.
USAE Waterways Experiment Station
P.O. Box 631
Vicksburg, Mississippi 39181-0631

Mark K. McVay
USAEDE
CEEUD-ED-TA
APO New York 09757

Yoav Me-Bar
8 Gedera Stairs
Haifa
ISRAEL 34722

David Medina
USAF Weapons Laboratory
WL/NTESG
Kirtland AFB, New Mexico 87117

Douglas H. Merkle
Applied Research Associates, Inc.
P.O. Box 40128
Tyndall AFB, Florida 32403

Hans-Georg Mett
Amt fur Studien und Ubungen
der Bundeswehr Bereich
Sonderaufgaben-Infrastruktur
Friedrich-Ebert-Str. 72
5060 Bergisch Gladbach 1
WEST GERMANY

Diane Miller
USAF Engineering & Services Laboratory
RDCS
Tyndall AFB, Florida 32403-6001

B. J. Mills
Sheltec Ltd.
Dewey House 55, High Street
Ringwood BH24 1AE Hampshire
UNITED KINGDOM

Craig A. Mills
WS Atkins & Partners
Woodcote Grove, Ashley Road
EPSOM SURREY KT18 5BW
UNITED KINGDOM

James E. Milton
Resident Director
University of Florida
Graduate Engineering Center
P.O. Box 1918
Eglin AFB, Florida 32542

Paul Mlakar
JAYCOR
2734 Washington Street
Vicksburg, Mississippi 39180

Brian Monroe
Sverdrup
Mail Stop 660
Arnold AFB, Tennessee 37389-5000

Jan Montross
Morton Thiokol, Inc.
P.O. Box 524
Brigham City, Utah 84302

Thomas Moriarty
University of Tennessee
School of Architecture
1715 Volunteer Blvd.
Knoxville, Tennessee 37996-2400

Michael L. Moring
Fraioli, Blum, Yesselman Assoc. Inc.
945 Norfolk Square
Norfolk, Virginia 23502

R. J. Mulkey
Mason-Hanger
P.O. Box 30020
Amarillo, Texas 79120

Raman Muralidaharan
University of Minnesota
Dept. of Civil & Mineral Engineering
Minneapolis, Minnesota 55455-0220

Robert N. Murtha
Naval Civil Engineering Lab
Code L51
Port Hueneme, California 93043

Guido C. Naeyaert
MOD Infrastructure Department
KGC/KDT/KTB - Kwartier Queen Elisabeth
Bloc 5
Everestraat - 1140 Brussels
BELGIUM

Phillip T. Nash
Texas Technical Research Institute
P.O. Box 4089
Mail Stop 1023
Lubbock, Texas 79409

Dale Nebuda
Hardened Structures Section
Corps of Engineers
ATTN: CEMRO-ED-SH
215 N 17th Street
Omaha, Negraska 68102-4978

D.H. Nelson
USAE Waterways Experiment Station
P.O. Box 631
Vicksburg, Mississippi 39181-0631

Howard Nickerson
Naval Facility Engineering Command
200 Stovall Street
Alexandria, VA 22332

Hans H. Oppliger
Luwa Ltd.
Filters & Shelter Equipment
Kanalstrasse 5, CH-8152 Glattbrugg
SWITZERLAND

Dave Ortiz
AF Weapons Laboratory/NTSM
Kirtland AFB, New Mexico 87117-6008

Chuck Oswald
Southwest Research Institute
P.O. Drawer 28510
San Antonio, Texas 78284

Manfred Ott
MOD GE Air Staff IV 4
WEST GERMANY

George E. Pace
AF Regional Civil Engineers
BMS/DEES
Norton AFB, CA 92409-6448

Hermann Pahl
NATO - Headquarters
International Staff
Infrastructure Directorate
1110 Brussels
BELGIUM

Jonas Palm
FORTF
63189 Eskilstuna
SWEDEN

Erhard Peters
Bundesamt fur Wehrtechnik und
Bescha ffung
Koblenz
WEST GERMANY

W. Pfrang
Industrieanlepen
Betriebsposellsdaft mbH (IABG)
TTF
Einsteinstr 20 / 8012 Ottobrann
WEST GERMANY

Dwayne D. Piepenburg
Lachel Piepenburg & Assoc., Inc.
P.O. Box 6177
Alexandria, Virginia 22306-0177

Steven J. Pierce
Department of Civil Engineering
Colorado State University
1231 West Swallow Road #25
Fort Collins, Colorado 80526

Joseph A. Poland
103D TFG
Bradley ANG Base
East Granby, Connecticut 06026-5000

Alvin L. Pope
Mason & Hanger Engineering, Inc.
1500 West Main Street
Lexington, Kentucky 40511

Robert J. Power, Jr.
Heery Engineering, Inc.
999 Peachtree St., NE
Atlanta, Georgia 30367-5401

Matti Purhonen
TEMET OY
Asentajankatu 3
SF - 00810
Helsinki 81
FINLAND

Capt. David Pyle
AFIT/CI
323 Eastbrook Drive
Charlottesville, Virginia 22901

N.J.M. Rees
Ministry of Defence
Safety Services Organisation
Block A-B Station Square House
St. Mary Cray Orpington Kent BR3 3RE
UNITED KINGDOM

Richard Reid
USAF Engineering & Services Laboratory
RDCS
Tyndall AFB, Florida 32403-6001

David E. Richardson
Hercules, Inc.
P.O. Box 98
Magna, Utah 84044

Michael A. Rochefort
Applied Research Associates, Inc.
P..O. Box 40128
Tyndall AFB, Florida 32403

Bob Rohani
USAE Waterways Experiment Station
P.O. Box 631
Vicksburg, Mississippi 39180-0631

Paul L. Rosengren, Jr.
Gulf Coast Community College
5230 W. Highway 98
Panama City, Florida 32401

Boyce Ross
P.O. Box 1600 HNDED-CS
Huntsville, Alabama 35807

C. Allen Ross
AFESC/RDCS
Tyndall AFB, Florida 32403-6001

Timothy J. Ross
Intelligent Systems Integration, Inc.
3801 Enbank NE
Albuquerque, New Mexico 87111

Arnon Rozen
BNE-Beitkha
KFAR JONA B 40300
ISRAEL

Dietger Russwurm
Amt fur Studien und ubungen
der Bundeswehr
Bereich Sonderaufgaben-Infrastruktur
Friedrich Ebert-Str. 72
5060 Bergisch Gladbach 1
WEST GERMANY

James Saylors
Bernard Johnson, Inc.
5050 Westheimer
Houston, Texas 77056

G. Scheklinski-Gluck
Fraunhofer Institut fur
Kurzzeitdynamik
Ernst Mach Institut
Eckerstr 4
7800 Freiburg
WEST GERMANY

Robert Schilling
Bundesministerium der
Verteidigung-RUE III7
D5300 Bonn1, Postfach 1328
WEST GERMANY

Walter Schmidt
University of Minnesota
Dept. of Civil & Mineral Engineering
Minneapolis, Minnesota 55455-0220

Bruce Schneider
University of New Mexico
New Mexico Engineering Research Institute
Campus P.O. Box 25
Albuquerque, New Mexico 87131

Hans-Josef Schneider
Staatsbeuamt Kaiserslautern West
Bauschenweg 32
6750 Kaiserslautern
WEST GERMANY

James Schumacher
TRW, Bldg. DH4 Room 2936
One Space Park
Redondo Beach, California 90278

F.H. Schluster
Universitat Karlsruhe
Abteilung Massivbau
Postfach 6980 7500 Karlsruhe 1
WEST GERMANY

William F. Seipel II
215 N 17th
Omaha, Nebraska 68102

Surendra P. Shah
Civil Engineering
Technological Institute
Northwestern University
Evanston, Illinois 60201

Hussain Shanna
University of Minnesota
Dept. of Civil & Mineral Engineering
Minneapolis, Minnesota 55455-0220

Raymond Shiroma
HQ PACAF/DEEE
Hickam AFB, Hawaii 98653-5001

A. K. Singh
CISS
P.O. Box 5456, Station B
Greenville, South Carolina 29606

Louis E. Smith
Target Vulnerability/Survivability Lab
University Park, Denver Research Inst.
Denver, Colorado 80208

Richard M. Smith
Applied Research Associates, Inc.
2750 Eisenhower Avenue Suite 100
Alexandria, Virginia 22314

F.Y. (Yates) Sorrell
Box 7910
North Carolina State University
Raleigh, North Carolina 27695-7910

Harold Speer
Integrated System Analysts, Inc.
7 Buckingham Way
Shalimar, Florida 32579

E. Spiller
Explosives Effects & Safety
PSA. DCES. Rm 706 Apollo Ho.
36 Wellesley Road
Croydon, London Cr9 3RR
UNITED KINGDOM

Terry R. Stanton
USAE Waterways Experiment Station
P.O. Box 631
Vicksburg, Mississippi 39181-0631

R. S. Steedman
Cambridge University Engr. Dept.
Trumpington Street
Cambridge CB21PZ
UNITED KINGDOM

Heinz Stemmler
Staatsbauamt Kaiserslautern West
Rauschenweg 32
6750 Kaiserslautern
WEST GERMANY

Klaus Stocker
Lehrstuhl fur Massivbau
Universitat der Bundeswehr Munchen
8014 Neubiberg
Werner-Heisenberg-Weg 39
WEST GERMANY

Jerry R. Stockton
Director, Weapons Effects Technology
BDM Corporation
7915 Jones Branch Drive
McLean, Virginia 22102-3396

William S. Strickland
USAF Engineering & Services Laboratory
RDCS
Tyndall AFB, Florida 32403-6001

Robert H. Sues
Applied Research Associates
6404 Falls of Neuse Road
Suite 200
Raleigh, North Carolina 27615

David I. Syse
Fixed TGT Technical Oversight Center
MSD/XRF
Eglin AFB, Florida 32542

Peter C. Tatnall
Bekaert Corporation
1395 Marietta Parkway
Bldg. 500, Suite 100
Marietta, Georgia 30067

Paul Newton Taylor
Sir Alexander Gibb & Partners
Early House, 427 London Road
Earley Reading RG6 1BL
UNITED KINGDOM

Teresa Taylor
University of Missouri-Columbia/Kansas City
UMC/UMKC Engineering
Truman Campus
600 West Mechanic
Independence, Missouri 64050-1799

Joseph W. Tedesco
Department of Civil Engineering
Auburn University, Alabama 36849

J. M. Terrier
SNPE Centre de Recherche du Bouchet
B.P.02 91710 Vert-le-Petit
FRANCE

Frank Theos
Box 863
AFCE-UK Region
APO New York 09241-5000

Paul Y. Thompson
Dept. of Civil Engineering
346 Weil Hall
University of Florida
Gainesville, Florida 32611

Jeff N. Thornton
Morton Thiokol, Inc.
P.O. Box 524, M/S 205
Brigham City, Utah 84302

David L. Tilson
USAE Waterways Experiment Station
P.O. Box 631
Vicksburg, Mississippi 39181-0631

Tan See Ting
Public Works Department
PWD Robinson Road Offices
77 Robinson Road
#03-00, SIA Building
Singapore 0106
REPUBLIC OF SINGAPORE

George A. Tompkins, Jr.
Temet USA, Inc.
P.O. Box 439
Great Falls, Virginia 22066

Wes Tucker
WL/NTESE
Kirtland AFB, New Mexico 87117-6008

Turhan Turker
UNITEK Ltd.
60-G Guilford Lane
Williamsville, New York 14221

Ken P. Turpin
HQ AFESC/YE
Tyndall AFB, Florida 32403-6001

L.A. Twisdale
Applied Research Associates, Inc.
6404 Falls of Neuse Road
Suite 200
Raleigh, North Carolina 27615

Lawrence G. Ullyatt
Target Vulnerability/Survivability Lab
University Park, Denver Researach Inst.
Denver, Colorado 80208

James Underwood
USAF Engineering & Services Laboratory
RDCS
Tyndall AFB, Florida 32403-6001

A. Vasiloff
Air Base Survivability
AD/YQ
Eglin AFB, FL 32542

Wilhelm von Essen
Televerket
Natavdelningen, Rum L 12:47
Marbackagatan 11
123 86 FARSTA, Sverige
SWEDEN

Bengt E. Vretblad
Fort F/F
S-63189 Eskilstuna
SWEDEN

Alfred Wagner
Wehrtechnische Dienststelle
Fuer Sprengmittel und Sondertechnik
Oberjettenberg, 8230 Schneizlreuth
WEST GERMANY

Francis Walley
OVE Arup Partnership
Central Technical Service
13 Fitzroy Street
London W1P 6B
UNITED KINGDOM

Edward K. Walsh
Dept. of Engineering Sciences
University of Florida
Gainesville, Florida 32611

Bruce Walton
HQ AFESC/RDCS
Tyndall AFB, FL 32403-6001

James Wassenberg
Integrated System Analysts, Inc.
7 Buckingham Way
Shalimar, Florida 32579

J.H. Weathersby
USAE Waterways Experiment Station
P.O. Box 631
Vicksburg, Mississippi 39181-0631

J. Weeheijm
Prins Maurits Laboratory INO
P.O. Box 45
2280 AA Rijswijk ZH
THE NETHERLANDS

Ronald D. Williams
Bernard Johnson, Inc.
5050 Westheimer
Houston, Texas 77056

Jon Windham
USAE Waterways Experiment Station
P.O. Box 631
Vicksburg, Mississippi 39180-0631

Tommy Wiren
Building & Construction Division
National Rescue Services Board
Jungfru Stavas Vag 3
65346 Carlstad
SWEDEN

Bruce E. Wittmeier
Integrated System Analysts, Inc.
7 Buckingham Way
Shalimar, Florida 32579

Dallon Thomas Woosley
MS-305
Arnold AFB, Tennessee 37389

Michael Worswick
Military Engineering Section for
Chief/DRES
Defence Research Establishment Suffield
Ralston, Alberta TOJ 2NO
CANADA

Hiroshi Yamaguchi
Protective Structures Research Section
1st Division Fourth Research Center of
Technical Research and Development Inst.
Japan Defense Agency, 2-9-54
Fuchinobe, Sagamihara, Kanagawa 229
JAPAN

Yaakov Yerushalmi
The ASP Group
1355 Piccard Drive, Suite 350
Rockville, Maryland 20850

C. Wayne Young
Sandia National Laboratory
P.O. Box 5800
Albuquerque, New Mexico 87115

Joel Young
Naval Civil Engineering Laboratory
Code L56
Port Hueneme, California 93043

Steve Young
Mason & Hanger - Silas Mason Co., Inc.
P.O. Box 30020
Amarillo, Texas 79177

Tony Zahrah
Applied Research Associates, Inc.
4300 San Mateo Blvd., NE
Suite A220
Albuquerque, New Mexico 87110